論文 / 著書情報
Article / Book Information

題目(和文)	酸化鉄系新規リチウム二次電池正極材料の開発
Title(English)	Development of new cathode materials for lithium batteries based on iron oxides
著者(和文)	神崎昌
Author(English)	
出典(和文)	学位:博士（理学）, 学位授与機関:東京工業大学, 報告番号:甲第6755号, 授与年月日:2007年3月26日, 学位の種別:課程博士, 審査員:菅野了次
Citation(English)	Degree:Doctor of Science, Conferring organization: Tokyo Institute of Technology, Report number:甲第6755号, Conferred date:2007/3/26, Degree Type:Course doctor, Examiner:
学位種別(和文)	博士論文
Type(English)	Doctoral Thesis

Development of new cathode materials for lithium batteries based on iron oxides

（酸化鉄系新規リチウム二次電池正極材料の開発）

Sho Kanzaki

Department of Electronic Chemistry

Interdisciplinary Graduated School of Science and Engineering

Tokyo Institute of Technology

January 2007

Contents

Chapter 1

Introduction

1-1 Materials for solid state ionics applied for lithium secondary batteries

Solid state ionics is a kind of the solid state chemistry and its field is learning of the dynamics of the ions in solid. Many subjects of solid state ionics have been performed for progress of new technologies. One of these subjects, the phenomenon of high ionic in crystalline solid has been an intensive research for a long period. For example, sodium-β-alumina[1], which is the sodium ion conductor, and AgI[2], which is the silver ion conductor, are well known. Recently, high lithium ionic conductors has been watched with keen interest for the lithium(ion) secondly battery compounds, which is one of the main candidate of power sources for electro devices, and various kinds of alternative compounds for lithium battery cathode have been extensively explored.

Schematic drawing of the conventional lithium ion secondary battery composed by carbon / organic solvent electrolyte with Li salt / $LiCoO_2$ is shown in Fig. 1.1. At the discharge process, the anode gives up electrons to the external circuit with the oxidizing the carbon and the Li ions are de-intercalated from interlayer of carbon to electrolyte. Li ions are conducting through the electrolyte to the cathode. Cathode accepts the electrons from the external circuit with reduced the valence state, and lithium ions are intercalated from electrode to interlayer and diffuse the interlayer pathway of CoO_6 framework. At the charge process, reverse reaction is undergone.

The solid-state lithium conductors for the lithium(ion) secondary battery cathode material are required the mix conduction of ion and electron. But commonly, ionic conductivity of crystalline compounds, such as covalent crystals and ionic crystals like oxide and halide, is very low, because atoms are usually settles in crystalline sits and only can diffuse through few defects in its crystal structure. The general acceptance of the criteria for ionic diffusion are follows:

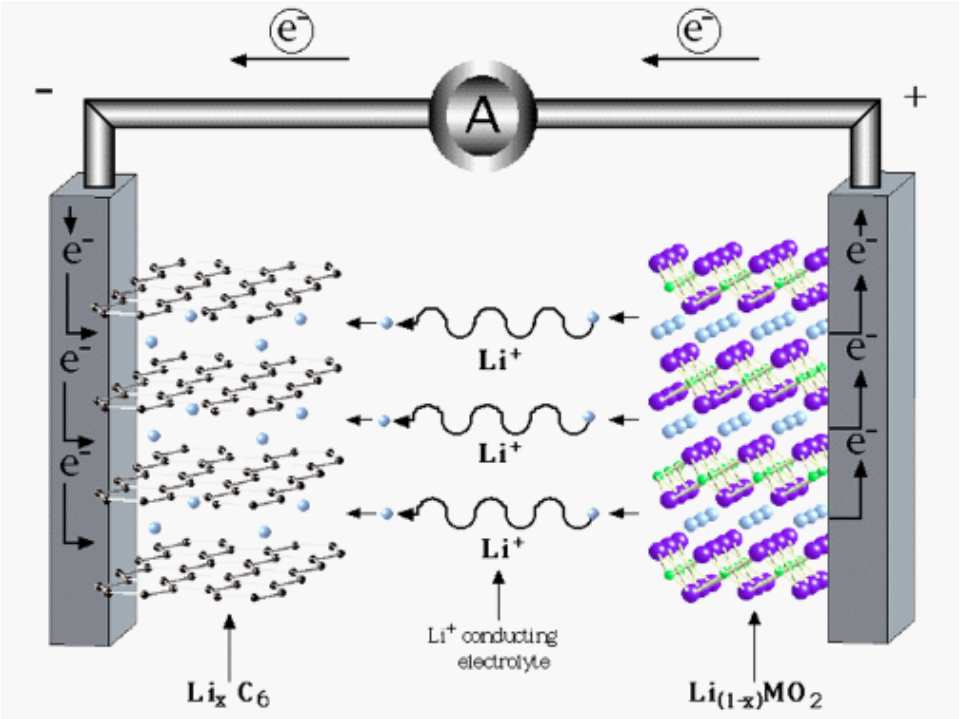

Fig. 1.1 Schematic drawing of LiMO_2 cathode / Li^+ electrolyte / carbon anode conventional lithium secondary battery

(1) The structure has to have the sites available for model ions compared with the quantity of mobile ions.

(2) The bottleneck in the framework should be an appropriate size for the mobile ion.

(3) The polarizable framework should be composed of anions sorrunding the pathway for the mobile ions.

From the structural viewpoint, 2D layered compounds meet a demand of these conditions. 2D layered compounds are constructed with the two kinds of bonding. One is the strong bonding, such as covalent bonding, for the internal layer and another bonding is the week bonding, such as van der Waals force or coulomb force, for the interlayer where various kinds of atoms, ions, and molecules can insert. Carbon graphite is kinds of materials which satisfy the above-mentioned properties. The structure of carbon graphite is formed by a stacking of the honeycomb carbon sheet, and various kinds of ions can accommodated in the inter layer space without rearrangement of the framework structure. This mechanism is used for lithium secondary battery anodes.

1-2 Lithium battery cathode materials

Various kinds of alternatives for cathode materials have been explored. In 1978, TiS_2 was reported for the first time as an cathode material of lithium secondary batteries by Wittingham *et al*[3]. The structure of TiS_2 is formed by sulfur atoms with a hexagonal closed packing framework, and titanium ions are located at the octahedral site of every other layer. The TiS_6 layers are constructed by bonding with the week Van der Waals force, and Li ions can intercalate into the inter layer space. Using of this character, Adams proposed a symmetrical cell constructed by the Li_xTiS_2 with different lithium compositions for the each electrode[4]. This cell indicates the Li intercalation and de-intercalation reactions in each electrode repeatedly. This type of cell is a prototype of lithium secondary batteries and called as a rocking chair type cell or a shuttlecock type cell.

Lithium ion is suitable for diffusion in crystal structure because of its small ionic radius

and a variety of compounds in which Li ions can diffuse. In these compounds, Li containing transition metal oxides were proposed to be applied for practical battery cathodes with high voltage and high power density. These compounds contained two or more types of cations with different ionic radius. These cations are located either in tetrahedral or octahedral sits derived from the closed packing of oxygen, and the ordering of these cations with many different manners provides the variety of structures. These are mainly classified as 2D framework compounds with the 2D diffusion pathway and 3D framework compounds with the 1D or 3D diffusion pathway. Following contents described about representative compounds from structural viewpoint.

1-2-1 ABO_2 (A = Li, B = transition metal) with 2D framework structure and 2D Li diffusion pathway

The transition metal-lithium oxides, LiMO$_2$, have various structure types depending on the radii ratio of Li and M ions. These structures are based on the rock-salt type structures derived from the oxygen cubic close packing. Table 1.1 and Fig. 1.2 summarizes the LiMO$_2$ compounds with various transition metals. Figure 1.3 shows the structural field map of LiMO$_2$ and NaMO$_2$.

Table 1.1 Structures of LiMO$_2$ compounds.

Structures	Ordered tetragonal	Disordered Rock-salt	Corrugated layer	Layered rocksalt
Compounds	γ-LiFeO$_2$ LiScO$_2$	α-LiFeO$_2$ LiTiO$_2$	LiMnO$_2$	LiVO$_2$ LiCrO$_2$ LiCoO$_2$ LiNiO$_2$

With in the ordered tetragonal structure, Li and M ions are ordered in the c-plane, Li and M ions are situated at the possible octahedral sites randomly in the disordered tetragonal structure. In the corrugated layered structure, edge sharing MO$_6$ octahedra form zigzag layers and Li ions occupy the

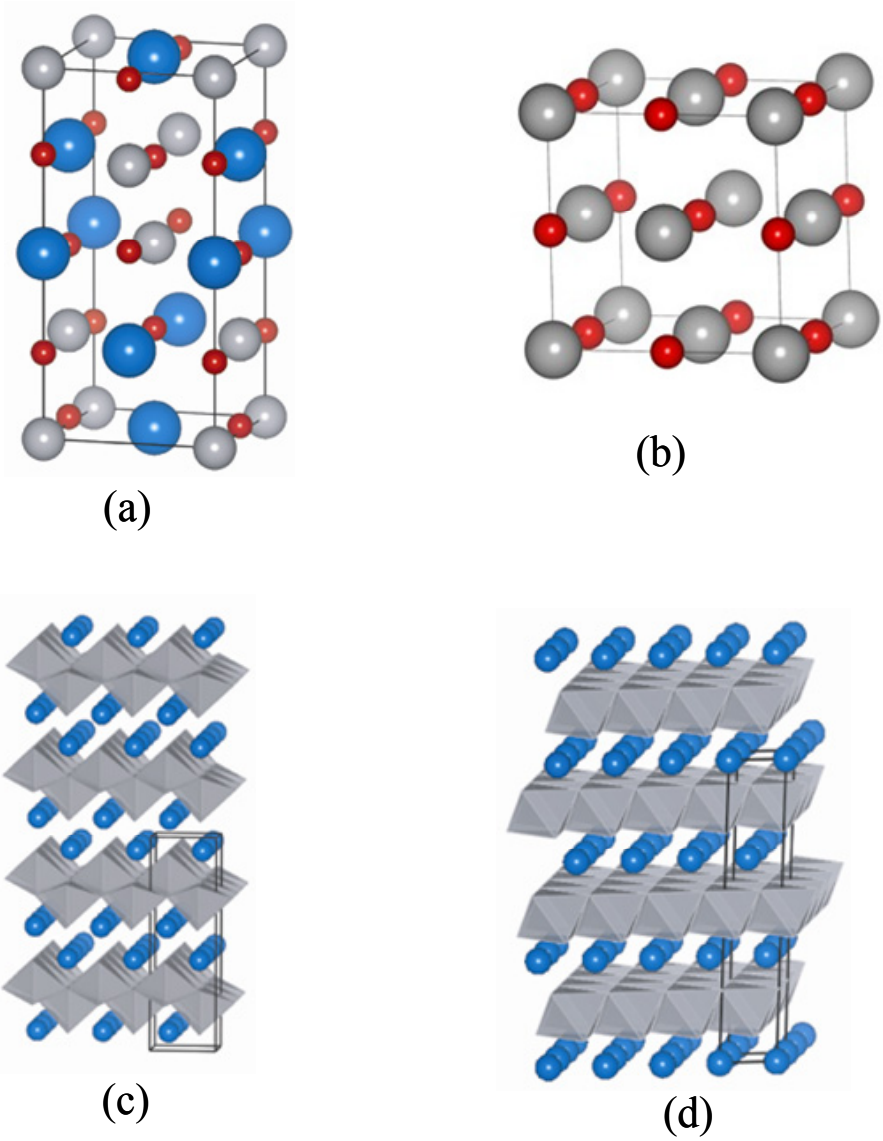

Fig. 1.2 Structures of LiMO$_2$ compounds, (a) ordered tetragonal, (b) disordered rocksalt, (c) corrugated layer, and (d) layered rocksalt.

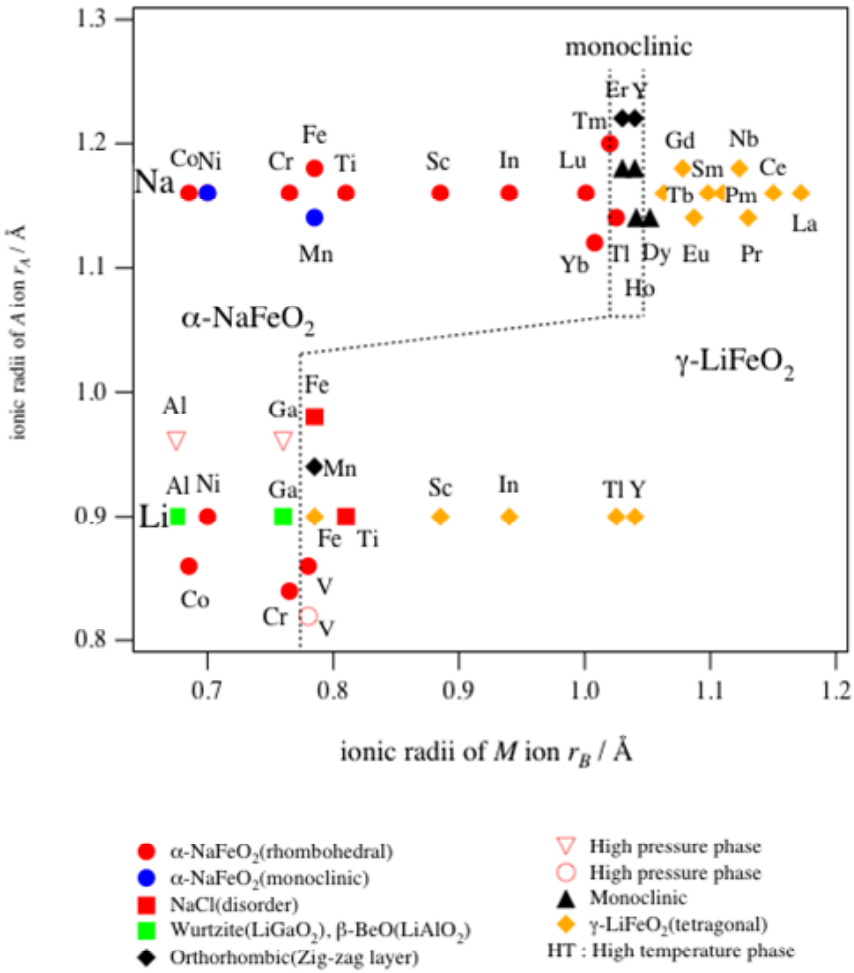

Fig. 1.3 Structure field map for AMO_2 (A = Li, Na, M = transition metal) compounds

interlayer sites. In the layered rocksalt structure, Li and *M* ions are situated in the separate planes in cubic close packing oxygen arrays. Normally, this structure has rhombohedral symmetry. When the effect of distortion such as cooperative Jahn-Teller effect exists the structure has monoclinic symmetry. In the corrugated layer and layered rocksalt structures, Li sites form the 2D diffusion pathway in the inter layer space. They have the possibility of reversible electrochemical reactions with (de-)intercalation process. Electrochemical properties of 2D layered compounds are very sensitive of its structure. When the disorders of *M* ions in the Li layer exist, may either act as a pillar to stabilize the structure or disturb the diffusion pathway of Li ions.

These structures are significantly influenced by synthetic conditions. Lithium cobalt oxide, $LiCoO_2$, is the most popular cathode compounds of conventional lithium ion secondary battery. Its electrochemical properties were reported by Goodenough *et al*[5]. It is rather easy to synthesize the stoichiometric sample because Co(III) is stable and lithium occupies only in the interlayer sites. However, high toxicity, high costs and poor resources of cobalt cause extensive research for cathode candidate with low toxicity and low cost. For example, such as $LiNiO_2$[6-10], $LiFeO_2$[11-13] and solid solutions, $LiMO_2$ (M = Ni_xMn_{1-x}, $Ni_xCo_yMn_{1-x-y}$, …)[14-20] are examined for the cathodes.

1-2-2 MOOH (M = transition metal) with tunnel type Li diffusion pathway

The transition metal oxyhydroxides have metal ions surrounded by oxygen and hydroxide. Depending on the chemical character of the transition metals, hydroxides work as an alkali, amphoteric, and acid. Table 1.2 summarizes the structures of *M*OOH compounds.

The crystal structures of *M*OOH with *M* = Fe and Mn have various types of poly-morphism. As these structures are sensitive to the synthetic conditions, it is possible to obtain the desired structure by selecting synthetic methods. Some of these structures have a tunnel-type Li diffusion pathway formed by edge-sharing of MO_6 octahedral. Figure 1.4 shows the α-*M*OOH type with 1×2 tunnel-type structure and α-MnO_2 type with 2×2 tunnel-type structure. Manganese oxides, MnO_2 (ramsdelite) and β-MnO_2 (pyrolusite) are well known tunnel structures and these

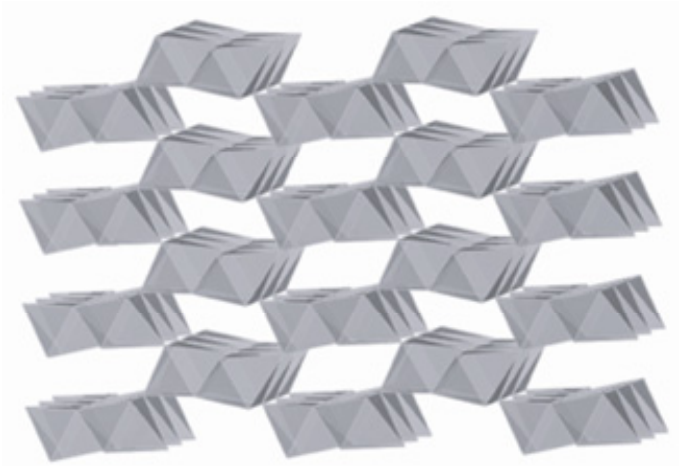

(a)

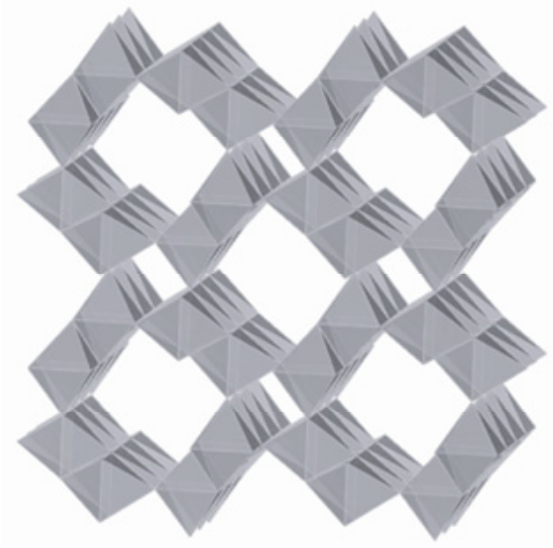

(b)

Fig. 1.4 Tunnel type structures of *M*OOH compounds. (a) 1×2 tunnel type and (b) 2×2 tunnel type.

compounds are expected to have high capacities (about 300 $mAh \cdot g^{-1}$ as theoretical capacity) and low cost lithium secondary battery cathodes. On the other hand, α-FeOOH and γ-FeOOH are known to be compounds with showing Li (de-)intercalation reaction.

Table 1.2 Structures of *M*OOH compounds.

Structures	α-*M*OOH type	Disordered rutile-like	Delafossite Structure	α-MnO_2 type	γ-*M*OOH type
Compounds	α-AlOOH α-ScOOH α-VOOH α-MnOOH α-FeOOH	InOOH β-CrOOH η–FeOOH	CoOOH	β-FeOOH	γ-AlOOH γ-ScOOH γ-MnOOH γ-FeOOH

1-2-3 AB_2O_4 (A = Li, B = transition metal) with 3D framework compounds with 3D or 1D Li diffusion pathway.

The most popular structures of 3D framework which enables for lithium battery cathode are spinel and olivine types. In the LiM_2O_4 spinel compounds, based on the face centered cubic unit cell with the cubic closed packing oxygen arrangement, Li ions situated at 8*a* tetrahedral site and *M* ions at 16*d* octahedral site. The interstitial 6*c* sites, situated between two 8a sites with face-sharing, and these two sites form 3D tunnel type diffusion pathway in the MO_6 framework. Figure 1.5 shows the cubic spinel type structure and diffusion pathway. The framework of the spinel compounds is very stable because *M* cations distribute three dimensionally in the oxygen cubic close packing, which forms stable host structures for the intercalation. Lithium manganese oxide, $LiMn_2O_4$ is one of the candidates of cathode materials for lithium secondary batteries of the next generation because of its low cost, low toxicity and stability[21-26].

The AB_2O_4 olivine structures are another examples of the 3D structure which is composed of hexagonal close packing oxygen array. Phosphorous ions occupy 1/2 of the tetrahedral site, *M* ions and Li ions occupy 1/4 of the octahedral sites, respectively, and 1D diffusion pathway of Li ions

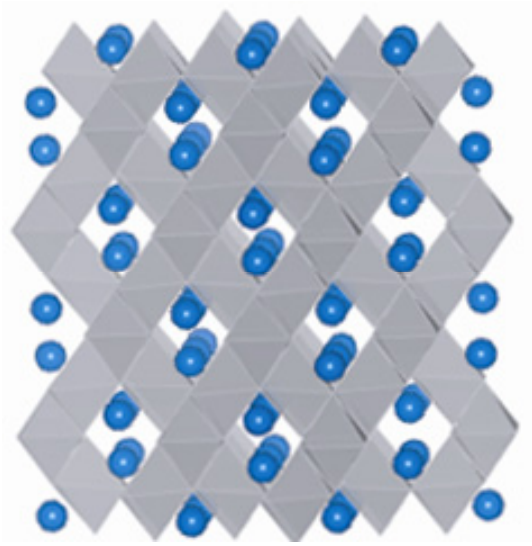

(a)

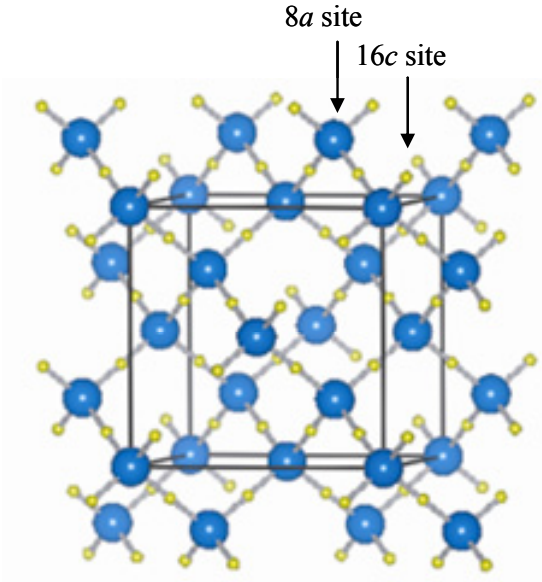

(b)

Fig. 1.5 (a) LiM_2O_4 cubic spinel type structure and (b) Li diffusion pathway of 8*a* to 8*a* through 16*c* site.

is constructed along the *b* axis. Figure 1.6 shows the olivine type structure. In this structure, electrons are localized and electronic conductivity is very low (~ 10^9 S/cm). Because of its stability caused by the poly-anion framework and high Li ionic conductivity, olivine type $LiFePO_4$, is excepted to be promising candidate for cathodes of the next generation[27-30].

1-2-4 New type Li ionic conductors containing the poly-silicate framework

Recently, new candidate of cathode materials, Li_2MSiO_4 (M = Fe, Mn) was reported (Fig. 1.7). The host structure is very stable because of SiO_4 polyhedral network similar to the PO_4 polyhedral network of the olivine structure. Furthermore, these compounds contain 2Li per formula which might provide high capacity with two lithium reactions[31, 32].

1-3 Development of cathode compounds using iron oxides.

Although the cathode material, $LiCoO_2$, is widely used for practical battery system, cobalt has several issues; toxic, cost and shortage of resource. Nickel and manganese based oxide widely studied to replace the cobalt system. However, the most attractive element for batteries is iron, which is low cost and environmental friendly. In the following section, simple iron binary/ternary systems with oxygen and hydrogen are discussed.

It is known that iron containing compounds with oxygen and hydrogen provides many crystal structures with a variety of compositions and valence state. Figure 1.8 displays the phase relationship of iron oxides and oxyhydroxides[33]. Among these compounds, the candidates of lithium secondary cathodes are γ-FeOOH with the layered structure, α-/β-FeOOH with the tunnel structure, α-Fe_2O_3 with the corundum structure, and γ-Fe_2O_3/Fe_3O_4 with the spinel structure. Thackeray and Goodenough reported the iron compounds for lithium battery cathode in 1982[34]. By both of chemical and electrochemical reactions, lithium can intercalate into α-Fe_2O_3 (hematite) and Fe_3O_4 (magnetite). Bonnet *et al.* and Pernat *et al.* reported that lithium also can intercalate into γ-Fe_2O_3 (maghemite) with chemically and electrochemically[35, 36]. But these compounds shows

Fig. 1.6 $LiFePO_4$ olivine type structure.

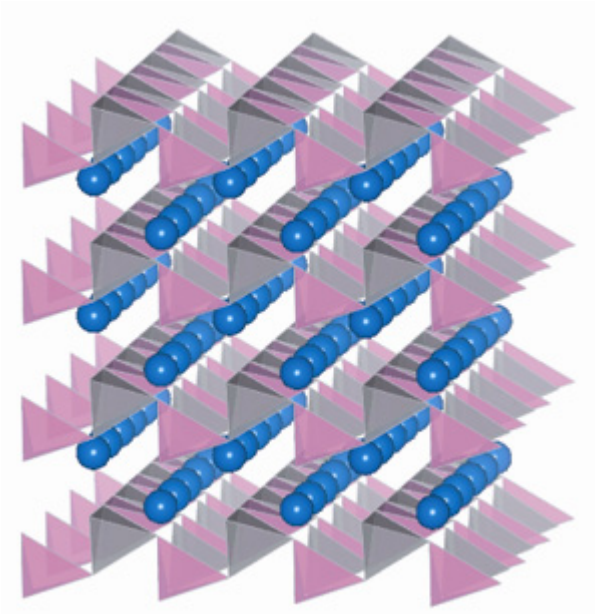

Fig. 1.7 Structure of Li_2FeSiO_4.

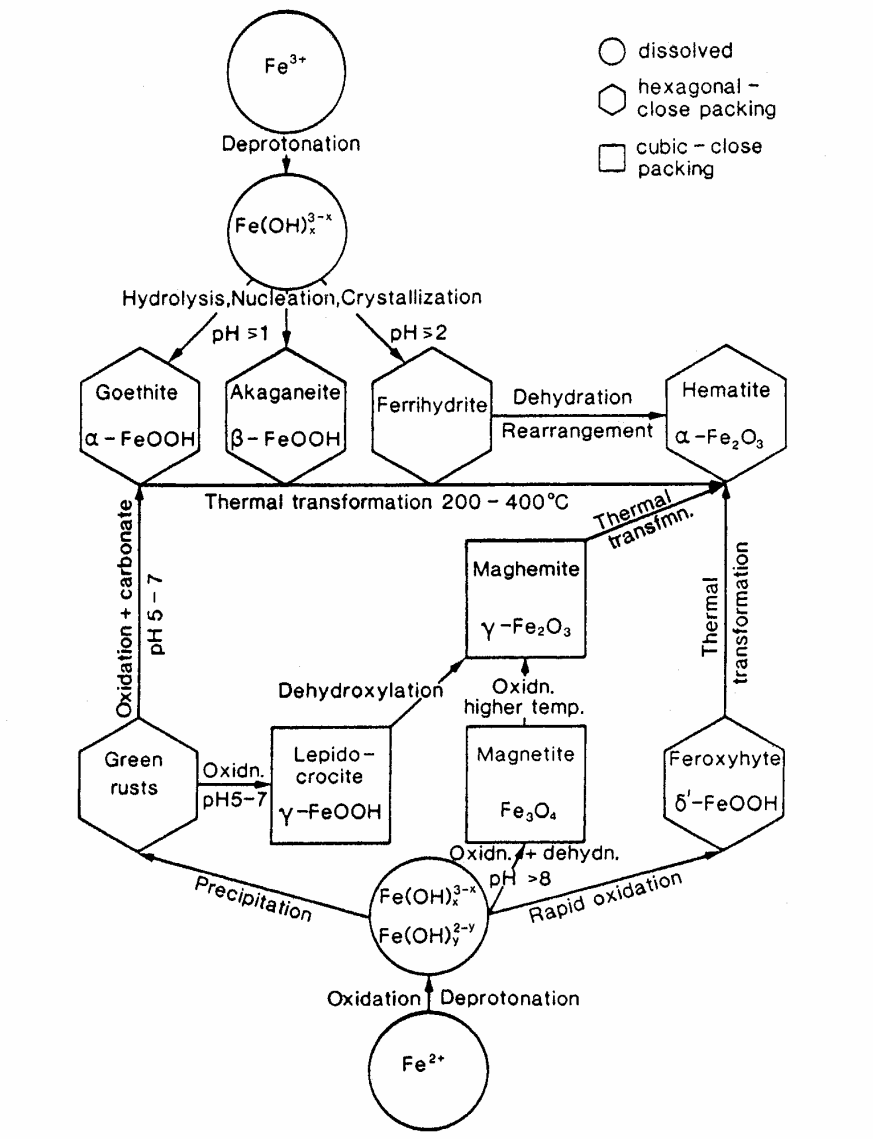

Fig. 1.8 Phase relationship between iron oxide and its related compounds.

irreversible phase transformation from corundum/spinel structure to disordered rocksalt structure, and it is considered to be difficult to apply for the lithium secondary battery cathode.

The iron oxides and their related compounds show lithium intercalation phenomena. Iron hydroxide forms three kinds of structures, α- type (goethite), β- type (akaganeite) and γ-type (lepidocrotite), which have Li diffusion pathway of 1×2 tunnel, 2×2 tunnel and 2D zigzag layer structures, respectively. In 1996, Kanno et al. reported that $LiFeO_2$ with the corrugated layer structure was synthesized by Li ion exchange reaction of γ-FeOOH with LiOH. Electrochemical reaction of this materials with lithium indicate reversible capacities of 80 mAh/g – 100 mAh/g[11]. Sakurai et al. also reported $LiFeO_2$ with the tunnel and zigzag layer types synthesized from α- type and γ- type FeOOH, which showed charge/discharge capacities of 60 mAh/g ~ 70 mAh/g and 100 mAh/g ~ 110 mAh/g, respectively[37]. These materials showed reversible lithium intercalation. Main problem of these compounds is its low capacities. It is considered that influence of hydrogen in the tunnel decrease the capacities. In 1999, Amine *et al.* investigated the β-FeOOH synthesized by the hydrolysis and found a capacity of 275 mAh/g[38]. This compound forms the tunnel with 2×2 large size which might make the reaction without any influence of hydrogen.

In iron oxides, particles with nanometric structure have been reported to show a reversible lithium intercalation reaction. Ito et al. reported K^+-β-ferrite can react reversibly with lithium[39, 40]. The structure of K^+-β-ferrite is composed of a 6 Å thickness of alkaline layer of K_2O are arranged between two inter layer of γ-Fe_2O_3 spinel blocks, which is the same structure as β-Al_2O_3. Lithium (de-)intercalates from/into the γ-Fe_2O_3 layer through the alkaline inter layer. Komaba et al. reported 20 nm particle size of α-Fe_2O_3 as lithium secondary battery cathode with the rechargeable capacities of 100 mAh/g ~ 110 mAh/g[41]. Tarascon group investigated the relationship between the particle size and electrochemical reactivity with lithium[42, 43]. When one lithium is reacted with a reaction, Li + α-Fe_2O_3 → $LiFe_2O_3$, α-Fe_2O_3 with a particle size of 1 μm showed irreversible corundum/disorder rocksalt transformation, while those with 20 nm, showed no phase transformation with a slight lattice expansion.

These results indicate that the particle size effect, such as increase of reactive area and flexible lattice expansion for intercalation, affects the reversibility of electrochemical (de-)intercalation reaction.

1-4 Development of new cathode compounds based on nanotechnology

In the pervious section, crystalline cathode materials are reviewed. The advantage of these materials is its high voltage and stable charge-discharge reversibility by its concrete framework of host materials. Nevertheless, its theoretical capacity or effective capacity is very small compare to anode, such as carbon graphite or Li metal, because the amount of Li which can react during charge-discharge reaction is restraint by the crystallographic sites in which lithium ions occupy. Figure 1.9 shows the capacity vs. potential (vs. Li/Li^+) map of various cathode materials. The theoretical capacities of principal crystalline materials are ~280, 170 and 148 mAh/g for layered $LiMO_2$, $LiFePO_4$ and $LiMn_2O_4$, respectively. By contrast, carbons shows over 500 mAh/g and Li metals are about 3800 mAh/g. To make a good use of battery, large amount of cathode active compounds than anode compounds must insert the stack of batteries and this process is one of the reasons for increase the weight of the batteries. (Generally, cathode active materials are heavier than anode one). New cathode active compounds which can react over one amount of lithium per one equivalent formula are strongly demanded.

1-4-1 Strategies for development of new cathode compound

New cathode active materials which can react over one amount of lithium per one equivalent formula are really necessary for future batteries. For example, it is necessary to investigate new reaction mechanism, which is not restricted by the number of the crystallographic site of the structure. Two types of new reactions are proposed. Schematic drawings of these reactions are shown in Fig 1.10. One is the adsorption reaction on the surface of small particles. The other is making nano-pore in the active materials which make lithium cluster in the pore.

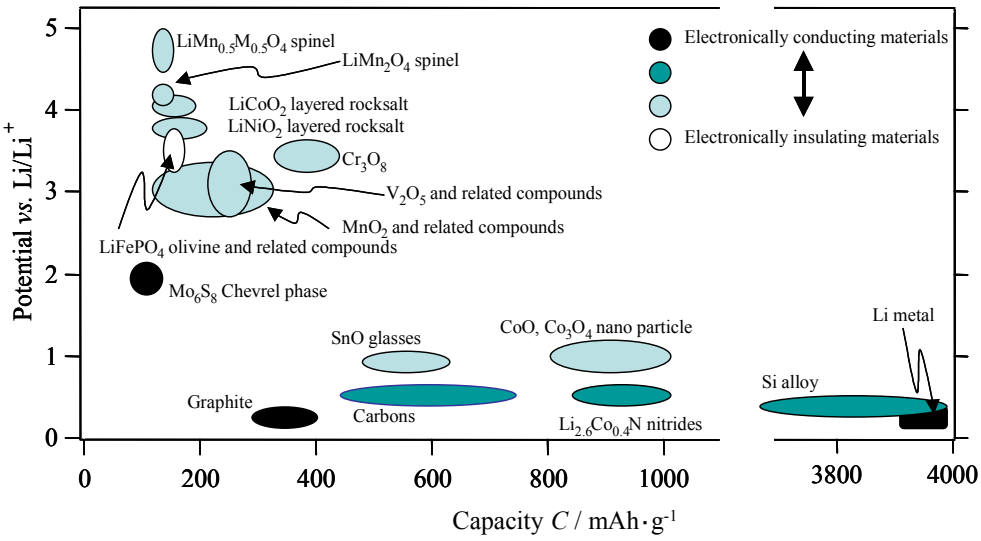

Fig. 1.9 Relationship between the potential and the capacity for electrode materials.

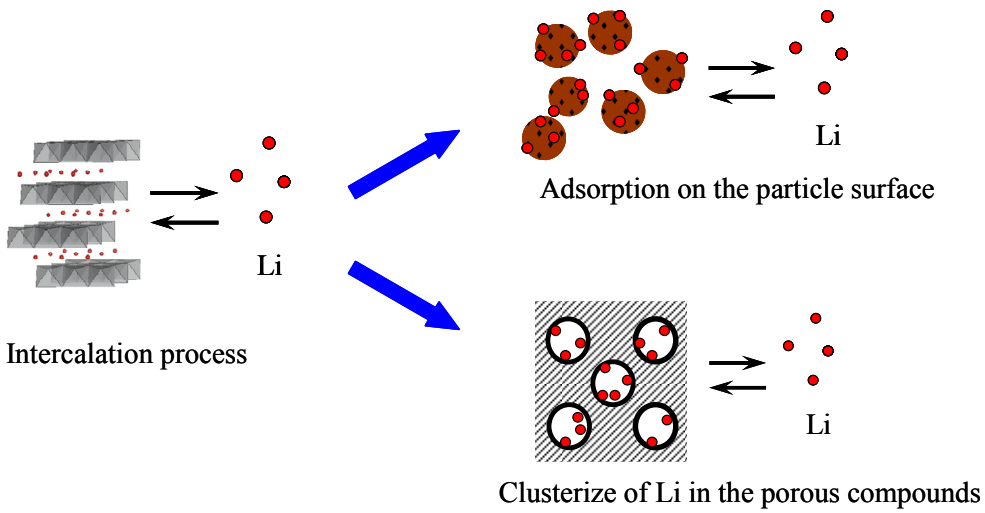

Fig. 1.10 Strategies for the realization of high capacity.

1-4-2 Ultra fine nanoparticles

Ultra fine nanoparticles have usually particle size of less than 100 nm. These particles indicate special features different from those of the 'bulk' compounds, which are derived from huge surface area and thin homogeneous interface. These nano particles are available for various kinds of applications, such as industrial technologies and medical technologies, for example, catalytic reactions like hydrogenation catalyst or desulfurization catalyst, and ceramics stuffs like high purity alumina or silicon nitride. In case of iron oxides, ultra fine nanoparticles are used for data storage devises such as magnetic tapes. In the magnetic tape, needle-like magnetic fine particles are dispersed homogeneously in organic binder. Memory density of devices is determined by the particle size and size distribution, so particle size control is very important.

As for lithium secondary battery cathodes, smaller particle size provided reversible reactions as mentioned above. Another example of cathode materials of ultra fine nanoparticles is iron-tin binary system, reported by Matsumura *et al.* The α-Fe_2O_3/SnO_2 binary compounds are synthesized by hydrothermal synthesis method in acidic condition[44]. When the particle size is 7 nm and the ratio of α-Fe_2O_3 to SnO_2 is 3:7, large capacities of over 300 mAh/g were obtained. From XRD and mössbauer spectroscopy measurements, lithium ions were found to insert into the SnO_2 rutile structure, and react with α-Fe_2O_3 with the Fe(III)/Fe(II) oxidation-reduction reaction on the interface of α-Fe_2O_3 phase. Stabilization and the reactivity enhanced by particle effect brought reversible and large storage capacity.

1-4-3 Mesoporous materials as lithium secondary battery application

Mesoporous materials are defined as kinds of porous compounds, whose pore diameter is 2 nm ~ 10 nm. Recently, these compounds get into the strong limelight because of its conspicuous structure and chemical behavior and expected to apply various kinds of industrial fields, catalyst technology, petrochemistry, medical technology, and electrochemistry. In the field of the lithium secondary battery, some kinds of mesoporous compounds are studied for both cathode and anode.

The advantage of mesoporous compounds are their large surface area and short diffusion length of Li ions, which brings high specific current density for rapid charge-discharge process. In case of anode compounds, mesoporous carbons are one of the candidates of anode compounds together with carbon nanotubes and pyrolytic carbons. The first results of mesoporous carbon applied for anode is reported by Zhou *et al.*[45]. They investigated the electrochemical properties of CMK-3 with lithium, and found that the CMK-3 showed a large reversible capacity of 1000 mAh/g with the current density of 100 mA/g. Except for the carbon compounds, mesoporous SiO_2, SnO_2, TiO_2 and composite compounds are investigated[46-52]. As for the cathodes, metal oxides of manganese, nickel, cobalt and iron phosphate are currently investigated[53-58].

1-5 Purpose of this paper

The purpose of this paper is to develop new cathode materials with ultra fine nano particles. The γ-Fe_2O_3 is one of the target materials. The structure of γ-Fe_2O_3 is categorized into the defect spinel in which a part of the octahedral sites of Fe_3O_4 is vacant. As for the conventional γ-Fe_2O_3, iron situated at the tetrahedral site blocks the lithium ion diffusion in γ-Fe_2O_3, thus leading to poor cathode characteristics. However, it is excepted that the ultra fine nanoparticles of γ-Fe_2O_3 may provide high reactivity and high charge-discharge capacities. With respect to this advantage, nano-sized γ-Fe_2O_3 was focused in the present study. Particular interests are found on the following subjects:

(i) suppression of spinel-rocksalt transformation which have hindered the reversible redox reaction,

(ii) maximizing lithium reactivity by huge surface area,

(iii) kinetic improvement by minimizing distance for lithium to pass across the particle, and

(iv) high lithium adsorption behavior.

In the present study, electrochemical activity of nano-sized γ-Fe_2O_3 with lithium, particle size effect, and influence of chemical oxidation are investigated by X-ray diffraction measurement, Mössbauer spectroscopy, FT-IR and TG measurements. Nano-sized crystalline γ-Fe_2O_3 was

synthesized by mild oxidation of iron micelle obtained from $Fe(CO)_5$. Heat treatment at 150ºC in oxygen was effective to remove a large amount of organic impurities, and weight of which was over 40 wt.% in the as-prepared solid phase. Significant suppression of the spinel-rocksalt transformation was confirmed as a major nano-sized effect and this led to a reversible topochemical lithium interaction with the corresponding lattice volume expansion.

Removal of residual phases on the surface by chemical oxidation with NO_2BF_4 provided improvement of charge-discharge characteristics; higher capacity and better reversibility. The reversible charge-discharge reaction of the nano-size γ-Fe_2O_3 was proceeded by a phase transition between the spinel and the disordered rock-salt type, which was previously claimed to be an irreversible process for the bulk materials. The nano-size effect of the phase transitions and the charge-discharge mechanism will be discussed. To clarify the reaction process of nano-sized γ-Fe_2O_3 with lithium, neutron diffraction and neutron scattering was studied in addition to X-ray diffraction studies. Reaction of nano-sized γ-Fe_2O_3 with lithium was preceded with biphasic reaction, spinel based phase and Li-rich disorder rocksalt phase.

New cathode material of iron oxide/porous carbon binary system was also investigated. Iron oxide/mesoporous carbon composite system was synthesized by electrolysis method. The nano-particles of the iron oxides tightly bounded on the highly electric conducting carbon matrix showed high electrochemical reactivity. The composite electrode showed extremely high charge-discharge capacity with high current rate capability.

The results of these subjects are described in the following chapters.

Reference

1. R. H. Radzilowski, Y. F. Yao and J. T. Kummer, *J. Appl. Phys.*, **40**, 4716 (1969).
2. B. B. Owens and G. R. Argue, *Science (Washington, DC, United States)*, **157**, 308 (1967).
3. M. S. Whittingham, *Prog. Solid State Chem.*, **12**, 41 (1978).
4. M. B. Armand, *NATO Conference Series VI: Materials Science*, **2**, 145 (1980).
5. K. Mizushima, P. C. Jones, P. J. Wiseman and J. B. Goodenough, *Mater. Res. Bull.*, **15**, 783 (1980).
6. M. G. S. R. Thomas, W. I. F. David, J. B. Goodenough and P. Groves, *Mater. Res. Bull.*, **20**, 1137 (1985).
7. T. Ohzuku, H. Komori, M. Nagayama, K. Sawai and T. Hirai, *Nippon Seramikkusu Kyokai Gakujutsu Ronbunshi*, **100**, 346 (1992).
8. T. Ohzuku, A. Ueda, M. Nagayama, Y. Iwakoshi and H. Komori, *Electrochim. Acta*, **38**, 1159 (1993).
9. R. Kanno, H. Kubo, Y. Kawamoto, T. Kamiyama, F. Izumi, Y. Takeda and M. Takano, *J. Solid State Chem.*, **110**, 216 (1994).
10. A. Hirano, K. Kanie, T. Ichikawa, N. Imanishi, Y. Takeda, R. Kanno, T. Kamiyama and F. Izumi, *Solid State Ionics*, **152-153**, 207 (2002).
11. R. Kanno, T. Shirane, Y. Kawamoto, Y. Takeda, M. Takano, M. Ohashi and Y. Yamaguchi, *J. Electrochem. Soc.*, **143**, 2435 (1996).
12. K. Ado, M. Tabuchi, H. Kobayashi, H. Kageyama, O. Nakamura, Y. Inaba, R. Kanno, M. Takagi and Y. Takeda, *J. Electrochem. Soc.*, **144**, L177 (1997).
13. Y. Sakurai, H. Arai and J.-i. Yamaki, *Solid State Ionics*, **113-115**, 29 (1998).
14. C. Delmas and I. Saadoune, *Solid State Ionics*, **53-56**, 370 (1992).
15. T. Ohzuku, A. Ueda and M. Kouguchi, *J. Electrochem. Soc.*, **142**, 4033 (1995).
16. M. Okada, K.-i. Takahashi and T. Mouri, *J. Power Sources*, **68**, 545 (1997).
17. T. Ohzuku and Y. Makimura, *Chem. Lett.*, 642 (2001).
18. D. D. MacNeil, Z. Lu and J. R. Dahn, *J. Electrochem. Soc.*, **149**, A1332 (2002).
19. N. Yabuuchi, Y. Koyama, N. Nakayama and T. Ohzuku, *J. Electrochem. Soc.*, **152**, A1434 (2005).
20. H. Xia, S. B. Tang, L. Lu, Y. S. Meng and G. Ceder, *Electrochim. Acta*, **52**, 1120 (2006).
21. M. M. Thackeray, W. I. F. David, P. G. Bruce and J. B. Goodenough, *Mater. Res. Bull.*, **18**, 461 (1983).
22. M. M. Thackeray, P. J. Johnson, L. A. De Picciotto, P. G. Bruce and J. B. Goodenough, *Mater. Res. Bull.*, **19**, 179 (1984).
23. R. J. Gummow, A. de Kock and M. M. Thackeray, *Solid State Ionics*, **69**, 59 (1994).
24. Y. Gao and J. R. Dahn, *J. Electrochem. Soc.*, **143**, 100 (1996).
25. M. Tabuchi, C. Masquelier, H. Kobayashi, R. Kanno, Y. Kobayashi, T. Akai, Y. Maki, H. Kageyama and O. Nakamura, *J. Power Sources*, **68**, 623 (1997).
26. T. Ohzuku, S. Kitano, M. Iwanaga, H. Matsuno and A. Ueda, *J. Power Sources*, **68**, 646 (1997).
27. A. K. Padhi, K. S. Nanjundaswamy and J. B. Goodenough, *J. Electrochem. Soc.*, **144**, 1188 (1997).

28. S. Okada, S. Sawa, M. Egashira, J. i. Yamaki, M. Tabuchi, H. Kageyama, T. Konishi and A. Yoshino, *J. Power Sources*, **97-98**, 430 (2001).
29. A. Yamada, M. Hosoya, S. C. Chung, K. Hinokuma, Y. Kudo and K. Y. Liu, *Ceram. Trans.*, **127**, 189 (2002).
30. A. Yamada, H. Koizumi, S.-I. Nishimura, N. Sonoyama, R. Kanno, M. Yonemura, T. Nakamura and Y. Kobayashi, *Nature Materials*, **5**, 357 (2006).
31. A. Nyten, A. Abouimrane, M. Armand, T. Gustafsson and J. O. Thomas, *Electrochem. Commun.*, **7**, 156 (2005).
32. M. E. Arroyo-de Dompablo, M. Armand, J. M. Tarascon and U. Amador, *Electrochem. Commun.*, **8**, 1292 (2006).
33. J. L. Jambor and J. E. Dutrizac, *Chem. Rev. (Washington, D. C.)*, **98**, 2549 (1998).
34. M. M. Thackeray, W. I. F. David and J. B. Goodenough, *Mater. Res. Bull.*, **17**, 785 (1982).
35. B. Bonnet, P. Strobel, M. Pernet, M. Gondrand, Y. Gros, C. Mouget and Y. Chabre, *Mater. Sci. Forum*, **91-93**, 345 (1992).
36. M. Pernet, P. Strobel, B. Bonnet, P. Bordet and Y. Chabre, *Solid State Ionics*, **66**, 259 (1993).
37. Y. Sakurai, H. Arai, S. Okada and J.-i. Yamaki, *J. Power Sources*, **68**, 711 (1997).
38. K. Amine, H. Yasuda and M. Yamachi, *J. Power Sources*, **81-82**, 221 (1999).
39. S. Ito, T. Aoyama and K. Akashi, *Solid State Ionics*, **113-115**, 23 (1998).
40. S. Ito, K. Ui, N. Koura and K. Akashi, *Solid State Ionics*, **113-115**, 17 (1998).
41. S. Komaba, K. Suzuki and N. Kumagai, *Electrochemistry (Tokyo, Japan)*, **70**, 506 (2002).
42. D. Larcher, C. Masquelier, D. Bonnin, Y. Chabre, V. Masson, J. B. Leriche and J. M. Tarascon, *J. Electrochem. Soc.*, **150**, A133 (2003).
43. D. Larcher, D. Bonnin, R. Cortes, I. Rivals, L. Personnaz and J. M. Tarascon, *J. Electrochem. Soc.*, **150**, A1643 (2003).
44. T. Matsumura, N. Sonoyama, R. Kanno and M. Takano, *Solid State Ionics*, **158**, 253 (2003).
45. H. Zhou, S. Zhu, M. Hibino, I. Honma and M. Ichihara, *Adv. Mater. (Weinheim, Fed. Repub. Ger.)*, **15**, 2107 (2003).
46. A. H. Whitehead, J. M. Elliott, N. R. B. Coleman, P. N. Bartlett, G. S. Attard and J. R. Owen, *Proc. - Electrochem. Soc.*, **98-16**, 128 (1999).
47. F. Chen, Z. Shi and M. Liu, *Chem. Commun. (Camb.)*, 2095 (2000).
48. B. Li, K. Li, C. Lu, D. Wu, L. Ling, C. Xu and R. a. Wang, *Shiyou Daxue Xuebao, Ziran Kexueban*, **25**, 81 (2001).
49. P. Li, C.-y. Wang, H. Jiang and J.-m. Zheng, *Tansu Jishu*, 5 (2001).
50. A. Yu and R. Frech, *J. Power Sources*, **104**, 97 (2002).
51. E. Kim, D. Son, T.-G. Kim, J. Cho, B. Park, K.-S. Ryu and S.-H. Chang, *Angew. Chem., Int. Ed.*, **43**, 5987 (2004).
52. V. Subramanian, J. C. Jiang, P. H. Smith and B. Rambabu, *J. Nanosci. Nanotechnol.*, **4**, 125 (2004).
53. P. Liu, S.-H. Lee, C. E. Tracy, Y. Yan and J. A. Turner, *Adv. Mater. (Weinheim, Fed. Repub. Ger.)*, **14**, 27 (2002).

54. A. Yu and R. Frech, *J. Electrochem. Soc.*, **149**, A99 (2002).
55. P. Liu, S.-H. Lee, C. E. Tracy and J. A. Turner, *Proc. - Electrochem. Soc.*, **2001-21**, 183 (2003).
56. I. Moriguchi, R. Hidaka, H. Yamada and T. Kudo, *Solid State Ionics*, **176**, 2361 (2005).
57. Z. Shi, Y. Li, W. Ye and Y. Yang, *Electrochem. Solid-State Lett.*, **8**, A396 (2005).
58. J. Santos-Pena, P. Soudan, C. O. Arean, G. T. Palomino and S. Franger, *J. Solid State Chem.*, **10**, 1 (2006).

Chapter 2

Experimental

2-1 Synthesis

2-1-1 Synthesis of γ-Fe_2O_3 ultra fine nano particles

γ-Fe_2O_3 ultra fine nano particles was synthesized by mild oxidation of $Fe(CO)_5$ using a method reported by Hyeon *et al*[1]. Synthesis route is shown in Fig. 2.1. 1.0 ml of $Fe(CO)_5$ (Aldrich) was injected into a mixture of 50 ml of octylether (TCI) and 2.4 ml of oleic acid, used as surfactant, at 100ºC. The solution was refluxed for 1h. After cooling to room temperature, 1.7 g of dehydrated trimethylamine *N*-oxide (Alfa Acer) as oxidant was added. The solution was heated again to 130ºC and the temperature was kept for 2h. Then, the reaction temperature was slowly increased up to the reflux point, and was kept for 1h. All the processes were performed in Ar atmosphere. After cooling to room temperature, excess ethanol was added. The black precipitate was centrifuged for isolation, and washed with ethanol. After washing, black precipitate / ethanol solution were dispersed on the glass petri dish and removed ethanol by air-drying. From the TG-DTA measurement, about 40% of organic impurity phase was contained in the coarse products. To remove impurity phases, the coarse products were heat treated at 150ºC for 20h in oxygen atmosphere.

2-1-2 Chemical oxidation

The chemical oxidation was carried out at room temperature. The iron oxides were stirred with NO_2BF_4 in an acetonitrile for 24h in an inert atmosphere of Ar gas flow. After the reaction, the precipitate was centrifuged for isolation, washed with acetonitrile, and dried in vacuum at 60ºC for one night.

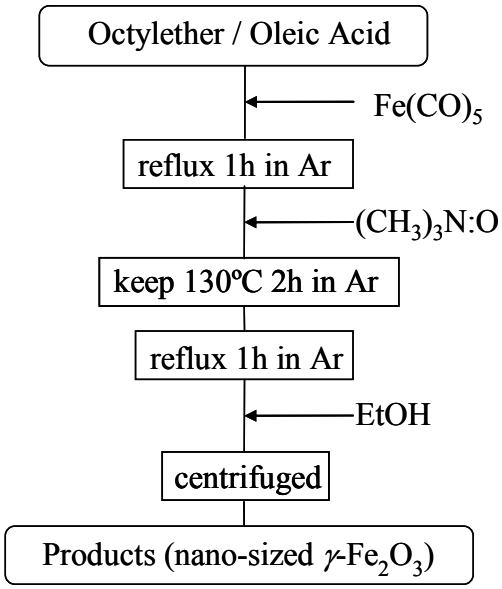

Fig. 2.1 Synthesis rote of nano-sized γ-Fe_2O_3

2-1-3 Chemical lithiation

Chemical lithiation was performed using *n*-butyl lithium in hexane solution. Nano-sized γ-Fe_2O_3 was dispersed into hexane, and then *n*-butyl lithium/hexane solution was injected under stirring. At the ratio of Li/Fe=1/4 ($Li_{0.5}Fe_2O_3$ as a formula of the product). After stirring for 24h in argon atmosphere at room temperature, hexane was removed by vacuum distillation and dried in vacuum at 60ºC for 3h.

2-1-4 Synthesis of mesoporous carbon

The synthesis of CMK-3 was performed using SBA-15 silica as the template and sucrose as the carbon source[2, 3]. Synthesis route is shown in Fig. 2.2. The SBA-15 sample was prepared using the triblock copolymer(P-123), $EO_{20}PO_{70}EO_{20}$ (Aldrich), as the surfactant and tetramethyl orthosilicate (TMOS, Kanto chem. 95%) as the silica sources, following synthesis procedure reported by Zhao et al. except for the modifications of the starting composition and stirring mode. The starting composition was 3.4×10^{-4} mol of P123: 1.8×10^{-2} mol TMOS: 0.11 mol HCl: 3.6 mol H_2O. Typically, 2 g of P123, 10 ml of HCl, 65 ml of H_2O, and 3 ml of TMOS. The mixture was stirred with magnetic stirring until TMOS was completely dissolved at 308 K. The mixture was placed in an oven for 20 h at 308 K, and subsequently for 24 h at 353 K. The product was filtered, dried without washing, and calcined at 823 K for 5h.

The calcined SBA-15 was impregnated with aqueous solution of sucrose containing sulfuric acid, similarly to the synthesis of CMK-3 except for the different amounts of sucrose and H_2SO_4. Briefly, 1.25 g of sucrose and 0.14 g of H_2SO_4 in 5 g of H_2O for 1 g of SBA-15. The mixture was placed in a drying oven for 6 h at 373 K, and subsequently the oven temperature was increased to 433 K and maintained there for 6h. The sample turned dark brown or black during the treatment in the oven. The silica sample, containing partially polymerized and carbonized sucrose at the present step, was treated again at 373 and 433 K using the same drying oven after the addition of 0.8 g of sucrose, 0.09 g of H_2SO_4 and 5 g of H_2O. The carbonization was completed by pyrolysis with heating to typically 1173 K under vacuum. The carbon-silica composite obtained after pyrolysis was washed with 10 mol/l NaOH solution three times at 353 K to remove the silica template. The template-free carbon product thus obtained was filtered, washed with ethanol, and dried at 393 K.

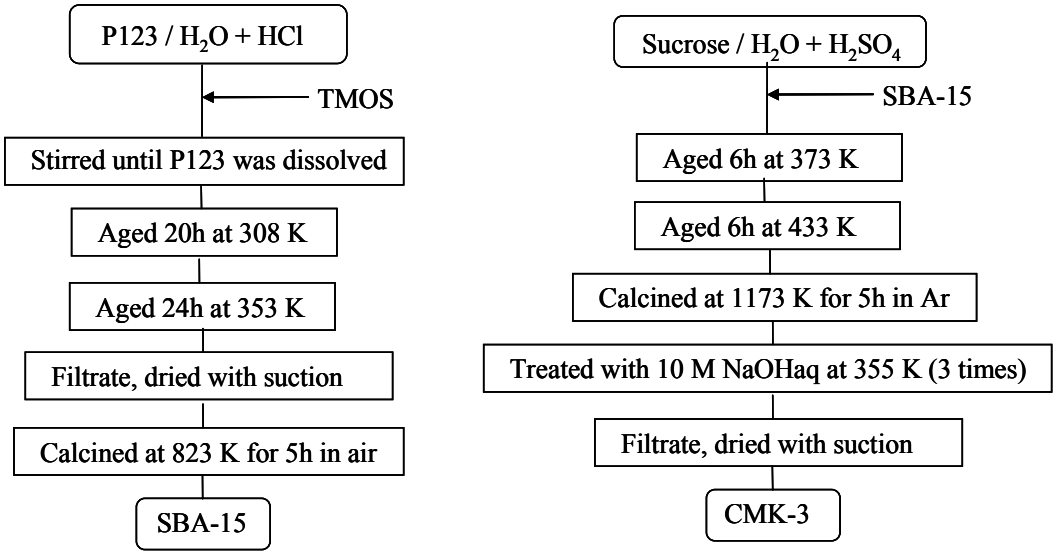

Fig. 2.2 Synthesis rote of mesoporous carbon, CMK-3

2-1-5 Preparation of Iron oxide mesoporous carbon binary system.

Iron metal was deposited on the mesoporous carbon by electrolysis using a method reported previously[4]. A mixture of CMK-3 and PTFE with a weight ratio of 95 : 5 was pressed into a pellet and placed on the carbon tape as an anode of the electrolysis. Cathode was an Al plate with a surface area of 5 cm^2. The electrolyte solution was prepared as follows: 36.6 g of ion sulfate hydrate ($FeSO_4$ $7H_2O$) and 12.5 g of iron chloride hydrate ($FeCl_2$ $4H_2O$) were dissolved in 28.9 ml of H_2O. The mixture was stirred at 313 K, and electrolysis was carried out with a current of 285 mA for 1710 s. After the electrolysis, the pellet was crashed, washed by distilled water, and dried. This process was repeated for several times.

2-2 Analytical measurement

2-2-1 X-ray diffraction measurement

X-ray diffraction data of powder samples were collected for characterization and determination of the structure. A high power X-ray diffractometer (RIGAKU RU-200B, 12 kW) with Cu$K\alpha$ radiation (λ = 1.5406 Å) and a X-ray diffractmeter (BRUKER AXS K. K., D8 FOCUS, 35 kV) with an CoKα (λ = 1.7889 Å) radiation was used. The diffraction data were collected for 1-3 seconds at each 0.03° step with the 2θ renge of 10° to 80°. In case of the lithiated samples, Ar shield stainless holder with KAPTON® window (Fig. 2.3) was used.

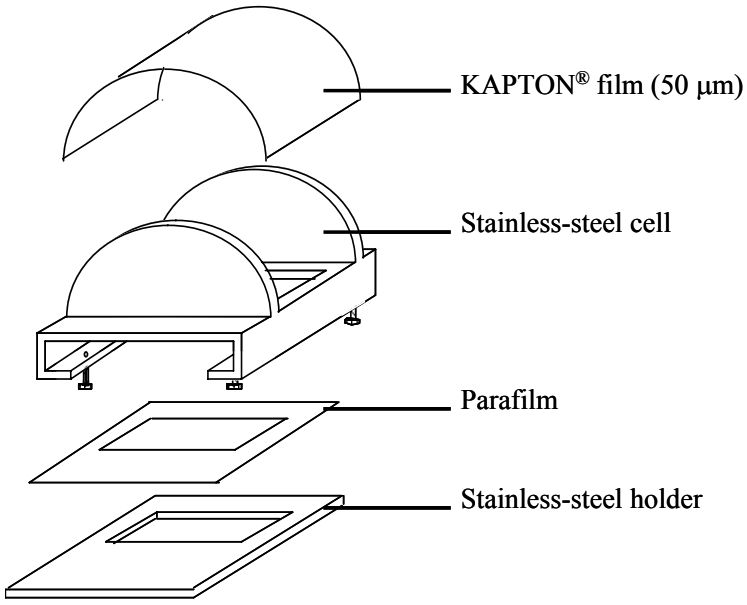

Fig. 2.3 Schematic image of the shield sample holder for XRD measurements.

2-2-2 Neutron diffraction measurement

Neutron diffraction measurement is a powerful tool to determine the structure of compounds containing light elements such as proton and lithium, because X-ray and neutron scatter by different mechanisms. X-ray scattering occurs primarily by interaction with the electrons that surround atoms, so that elements at the top of periodic table are weaker X-ray scatterers than those near the bottom and the scattering power falls off with increasing angle. On the other hand, neutrons are primarily scattered by atomic nuclei. There is only isotropic point scattering. Also nuclear scattering is a combination of scattering by short range nuclear forces and resonance scattering which gives neutron scattering lengths that vary very irregularly across the periodic table and from isotope to isotope.

Neutron different data were taken on a time-of-flight (TOF) type Special Environment Powder Diffractometer, SEPD, at the Intense Pulsed Neutron Source (IPNS) at the Argonne National Laboratory. High energy protons from the accelerator strike the tantalic target. The high energy neutron thus produced in the target by spallation are moderated to lower energies in solid CH_4 moderators (100 K) surrounding the target, and moderated neutron beams is incident to the samples in vacuum through beam shutter. Time-of-flight from target to counter through samples are monitored and time-of-flight (t) are translated to planer spacing (d) by the translated relation.

$$d \sin\theta = \frac{\lambda}{2} = \frac{ht}{2mL} = \frac{t}{505.55L},$$

where

h: Planks constant,

m: neutron mass (1.675×10^{-27} kg),

L: total path length of flight from target to counter through samples.

The specimen of (ca. 2 g) was put in a cylindrical vanadium cell. SEPD has the 4 banks of the detectors established on 2θ = 22°, 44°, 90°, 144°, respectively. Because of its higher count rate, The corrected data of 90° bank is used for the refinement of the structure.

2-2-3 Neutron total scattering measurement and atomic pair distribution function, PDF

Neutron total scattering measurement was performed by the TOF type High Intensity Total Scattering Spectrometer, HIT-II, at the KENS pulsed spallation neutron source at the High Energy Accelerator Research Organization (KEK). HIT-II has the 7 banks with the 2θ range of 10° - 160°. The specimen of (ca. 2 g) was put in a cylindrical TiZr cell. The structure factor, $S(Q)$ were collected with the Q range of 3-500 nm.

Conventional structural determination based on the Bragg refractions can determine the long range average structure of crystal. However, many materials are quite disordered or have short range arrangement and the study of this short atomic arrangement is even more important in understanding of their properties. One of the methods to reveal the local structure of a crystal is the analysis of the PDF, which is the function of the total scattering function of $S(Q)$, calculated from the diffuse scattering. Diffuse scattering contains the interaction of two atoms. In case of the neutron diffuse scattering of two atoms with there distance is r, phase shift of the neutrons scattered by each atoms are:

$$\phi = \frac{2\pi}{\lambda}\left(k - k_0\right) = \mathrm{Q}\cdot r,$$

where

k_0 and k: unit vectors of incident neutron and scattered neutron, respectively.

Q: scattering vector,

when the scattering angle is 2θ, the magnitude of the scattering vector Q is:

$$Q = |\mathrm{Q}| = \frac{4\pi \sin\theta}{\lambda},$$

After the correction for absorption and multiple scattering, the intensity of neutrons scattered from a collection of atoms, $I(Q)$ is given by:

$$I(Q) = \left\langle \sum_{\alpha\beta} b_\alpha b_\beta \exp\left\{iQ\cdot\left(x_\alpha - x_\beta\right)\right\} \right\rangle,$$

where

b: neutron scattering length,

x: the position of atoms.

The intensity, *I*(*Q*), depends on the total number of scatterers present, their scattering strength. It also contains a component of incoherent scattering. The structure function, *S*(*Q*) is only depend on the structure of the sample:

$$S(Q) = \frac{I(Q)}{N\bar{b}^2} - \frac{\overline{b^2} - \bar{b}^2}{\bar{b}^2},$$

where

N: number of scatters,

$\bar{n}$: averages over all the scatterers.

The second term gives the incoherent scattering contribution. The PDF, *G*(*r*) is obtained from the Fourier transformation of the *S*(*Q*):

$$G(r) = 4\pi r[\rho(r) - \rho_0] = \frac{2}{\pi}\int_0^\infty Q[S(Q) - 1]\sin(Qr)dQ,$$

where $\rho(r)$ is a pair density,

$$\rho(r) = \rho_0 + \frac{1}{2\pi r^2}\int_0^\infty Q[S(Q) - 1]\sin(Qr)dQ,$$

ρ_0:average number density.

2-2-4 Rietveld analysis.

Structural parameters were refined by Rietveld analysis with the computer program RITAN-2000[5] for the X-ray diffraction data and GSAS[6, 7] for the X- ray diffraction data and neutron diffraction data, respectively. The Rietveld method is a technique for refining lattice parameters and structural parameters directly from whole powder diffraction patterns without separating reflections. This method is useful when single crystal cannot be grown.

In the Rietveld analysis, the residual S_y is minimized by a least-square refinement:

$$S_y = \sum w_i (y_i - y_{ci})^2 ,$$

where

w_i: $w_i = \frac{1}{y_i}$,

y_i: observed intensity at the ith step,

y_{ci}: calculated intensity at the ith step,

and the sum is the overall number data points.

The calculated y_{ci} are determined from the $|F_k|^2$ values calculated from the structural model by summing of the calculated contributions from neighboring Bragg refractions plus background:

$$y_{ci} = s \sum L_K \left|F_K\right|^2 \phi(2\theta_i - 2\theta_K) P_K A + y_{bi} ,$$

where

s: scale factor,

K: Miller Indices, hkl, for a Bragg reflection,

L_K: Lorentz, polarization and multiplicity factors,

ϕ: refraction profile function,

P_K: preferred orientation function,

A: absorption factor,

F_k: structure factor,

Y_{bi}: background intensity at the ith step.

For the X-ray Rietveld analysis, refraction points and intensities were calculated for both Cu$K\alpha_1$ and Cu$K\alpha_2$ with a factor of 0.497 applied to the calculated integrated intensities of Cu$K\alpha_2$ peaks, so that only single scale factor is obtained. For angle-dispersive X-ray analysis, the profile shape function is represented as the product of symmetrical profile function and asymmetrical profile function; a pseudo-Voigt profile shape function was used as profile shape function. The mixing parameter, g, corresponding to the ratio of the component of the Gaussian and Lorentzian

functions, was including in the least-square refinements. For TOF neutron Rietveld analysis, the sum of two experimental profile shape function by Cole and Windsor was used.

The Rietveld refinement process will adjust the refineable parameters until the residual minimized. The parameters, R_{wp} (weighted pattern *R*-factor), R_p (pattern *R*-factor), R_R (Rietveld *R*-factor), R_e (expected *R*-factor), R_I (integrated intensity *R*-factor), R_F (structure *R*-factor) and *S* (goodness of fit) are indicators of the progress of refinements. Of those indicators, two indicators are important to judge whether the refinement is convolute satisfactory. R_{wp} is the most meaningful of the those *R* factors because the numerator is the residual being minimized. Another useful numerical criterion is the goodness of fit, S (= R_{wp}/R_e). In general, a *S* value of 1.3 or less is usually considered to be satisfactory.

2-2-5 Thermogravimetry measurement

Thermogravimetry and differential thermal analysis (TG-DTA) were measured using a 'TG/DTA6300' with 'EXSTAR6000' (SII.). Conditions are temperature range of room temperature to 1000 °C with the heating rate of 5 °C/min or 10 °C/min in O_2, Air, and Ar atmosphere.

2-2-6 FT-IR spectra measurement

FT-IR spectra were obtained using a 'NEXUS 670 FT-IR' (NICOLET), with the KBr disk method. For the pretreatment, KBr was dried at 120°C in vacuum overnight.

2-2-7 SEM observation

Scanning electron microscope (SEM) observation and energy dispersive X-ray (EDX) analysis were using 'S-4800' and 'S-4700' (Hitachi Co.) with the magnitude of ~×800,000. Compounds are fixed on the aluminum holder with carbon paste.

2-2-8 Specific surface area and pore size distribution analysis

Specific surface area was analyzed by nitrogen adsorption and desorption isotherms (BET) 'BEL JAPAN,INC., BELSORP-mini-II' with the sample was pretreated at 150℃, 1h in the vacuum line. The BET data were analyzed by the BJH (Barrett-Joyner-Halenda) method using the halsey equation for multiplayer thickness. The pore size distribution curves came from the analysis of the adsorption branch of isotherm. The pore volume was taken at the $P / P_0 = 0.952$ single point.

2-2-9 Elemental analyses

Elemental analysis were performed by inductivity coupled plasma (ICP) and organic elemental analysis. ICP analyses were using 'Prodigy' (LEEMAN LABS / JEOL DATUM) and 'ICPS-8100' (SHIMAZU). Organic element analysis was using 'MT-5' (YANACO).

2-3 Physical Property measurements

2-3-1 Mössbauer measurement

The Mössbauer spectra were obtained using a 'MÖSSBAUR SPECTROSCOPY' (TOPOLOGIC SYSTEM Inc.) with ^{57}Co γ-ray source at room temperature. The source velocity was calculated by using α-iron as a standard. There are three parameters for fitting the obtain spectra, isomer shift (*IS*) and quadropole splitting (*QS*). *IS* reflects the density of electrons, and the oxidation state of iron or degree of localization of electrons are estimated. *QS* shows the electron gradient around the nuclei, and the coordination state of anion or distribution of electrons are obtained.

2-3-2 Electrochemical measurements

Electrochemical characteristics were measured at 25°C with a 2032 coin type cell (Fig. 2.4) or a HS test cell (Hohsen Co., Fig. 2.5), with the charge-discharge device 'TOSCAT-3100' (TOYO system Inc.). The electrolyte was ethylene carbonate (EC) - diethyl carbonate (DEC) with

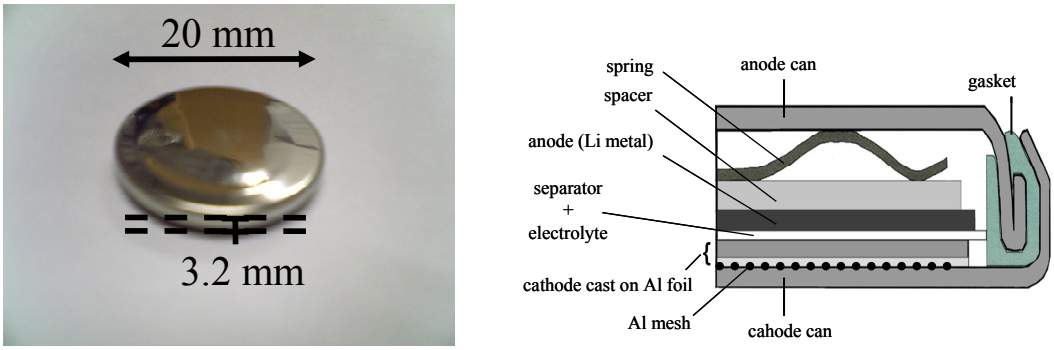

Fig. 2.4 Picture and configuration of the 2032 type coin cell.

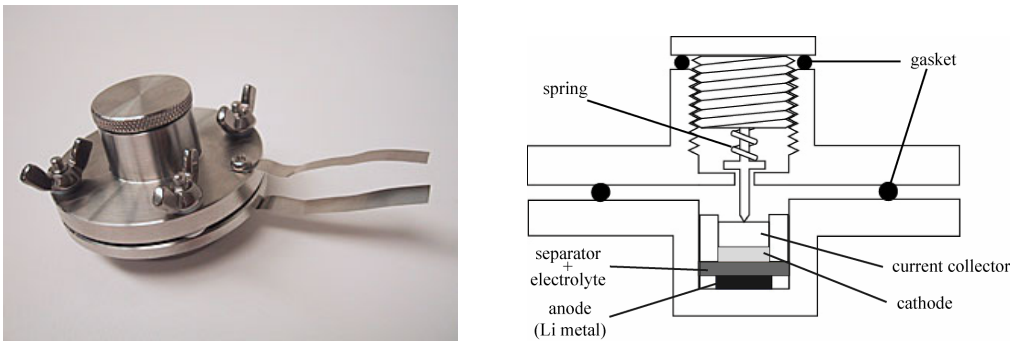

Fig. 2.5 Picture and configuration of the HS test cell.

a molar ratio of 3 : 7 as a solvent and a supporting electrolyte of 1 M $LiPF_6$. Polypropylene film and 0.6 mm thickness of Li foil were used as the separator and anode, respectively.

The cathode was a mixture of γ-Fe_2O_3 : acetylene black : Poly(vinilidene fluoride) (PVdF), with a weight ratio of 4 : 2 : 1. The mixture was dispersed into *N*-methyl-2-pyrrolidinone (NMP), and the slurry was cast on an Al foil to form an electrode. After remove the solution, the electrode was punched into a circular disk with the diameter of ϕ16 mm for coin cell or ϕ15 mm for HS test cell, respectively. Also, the electrode was dried at 80ºC in a vacuum before supplying for electrochemical tests. All the processes except for the vacuum drying were performed in an Ar field grove box.

For the palletized electrode, the cathode was a mixture of iron oxide/mesoporous carbon binary compound and polytetrafluoroethylene (PTFE) powder with the weight ration of 95 : 5. The cathode was pressed with a pressure of 20 MPa with the diameter of ϕ11 mm. The electrode was dried at 150ºC in a vacuum before supplying for electrochemical tests.

Reference

1. T. Hyeon, S. S. Lee, J. Park, Y. Chung and H. B. Na, *J. Am. Chem. Soc.*, **123**, 12798 (2001).
2. D. Zhao, J. Feng, Q. Huo, N. Melosh, G. H. Frederickson, B. F. Chmelka and G. D. Stucky, *Science (Washington, D. C.)*, **279**, 548 (1998).
3. S. Jun, S. H. Joo, R. Ryoo, M. Kruk, M. Jaroniec, Z. Liu, T. Ohsuna and O. Terasaki, *J. Am. Chem. Soc.*, **122**, 10712 (2000).
4. Y. Nobumoto, K. Kubota, S. Yoshihara, T. Shirakashi, W. Oikawa, N. Kudoh, *Proc.of the 109th Annual Conference of SFSJ*
5. F. Izumi and T. Ikeda, *Mater. Sci. Forum*, **321-324**, 198 (2000).
6. A.C. Larson and R.B. Von Dreele, *"General Structure Analysis System (GSAS)",* Los Alamos National Laboratory Report LAUR 86-748 (2000).
7. B. H. Toby, *J. Appl. Crystallogr.*, **34**, 210 (2001).

Chapter 3

Synthesis of the nano-sized γ-Fe_2O_3

3-1 Introduction

Conventional synthesis methods of ultra fine nanoparticle are roughly divided into two methods, breakdown and buildup. Features of breakdown method are easy processing and low cost, while control of particle size, homogenous grinding and preparation of particle size less than 50 nm are difficult. Typical method of breakdown is mechanical milling. On the other hand, features of buildup method are suitable for obtaining high purity compound, easily to control the parameters of particle size, distribution, crystalline or amorphous state, and so on. Buildup method is mainly classified as vapor-phase method and liquid-phase method and many techniques are developed. Table 3.1 summarizes the buildup methods[1].

In this study, protective colloid method was chosen. Advantage of this method are: (i) no need the exclusive apparatus, (ii) possible to obtain high crystalline and homogeneous distribution particles with the size of under 10 nm and (iii) easy to control the particle size as functions of surfactant concentration, temperature, pH, and so on. Details of the synthesis are described in this section.

Table 3.1 Prevailing techniques of buildup method

Vapor-phase method	Liquid-phase method
Gas evaporation method	Coprecipitation method
Spattering method	Alkoxide method
Ark plasma evaporation method	Hydrothermal method
Laser evaporation method	Sol-gel method
High-frequency plasma evaporation method	Suspension polymerization method
Thermal CVD method	Protective colloid method
Plasma CVD method	Dry spraying method
Laser CVD method	Emulsion method

3-2 Process and method

In this research, nano-sized γ-Fe_2O_3 was synthesized by the mild oxidation of iron-micelle, reported by Hyeon *et al*[2]. Scheme of the synthesis route was shown in Fig. 3.1. The details of the reaction process and mechanism of each reaction processes are as follows:

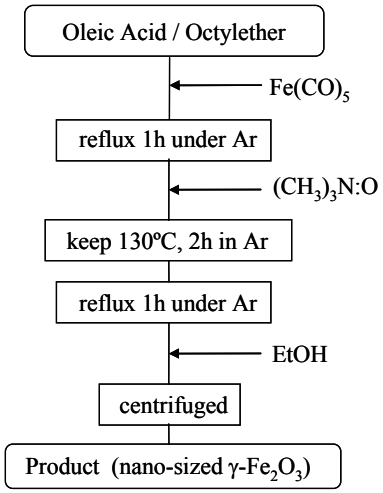

Fig. 3.1 Synthesis rote of nano-sized γ-Fe_2O_3

(i) Addition of the $Fe(CO)_5$ to the solution of octylether/oleic acid is one of the important process to get the homogeneous particle size products. Momentarily injection of $Fe(CO)_5$ and vigorous stirring of the solvent makes the solution homogeneous, and suppress the particle size distribution.

(ii) During the first reflux, thermal decomposition of $Fe(CO)_5$ was proceeded and iron reversed micelle with the oleic acid, as a surfactant, was formed. Partial oxidation of the iron was progressed and solution color was changed from clear yellow to dark brown.

(iii) Iron micelles are oxidized by the weak oxidant trimethylamine-*N*-oxide under mild condition (at 130°C). Solution color was changed from dark brown to right brown. It is considered that the spinel framework was constructed during this process.

(iv) During the second reflux, oxidation process was completely progressed. Solution color was changed from light brown to dark brown again.

(v) Ethanol was acted as a poor solvent. With the addition of ethanol, iron oxide micelles are agglutinated and precipitated.

Figure 3.2 shows the TEM images of the product. In addition to the particles, membrane-like material was observed. This material considered to be an organic impurity phase was generated during the synthesis process. Figure 3.3 shows XRD patterns of the products synthesized by the

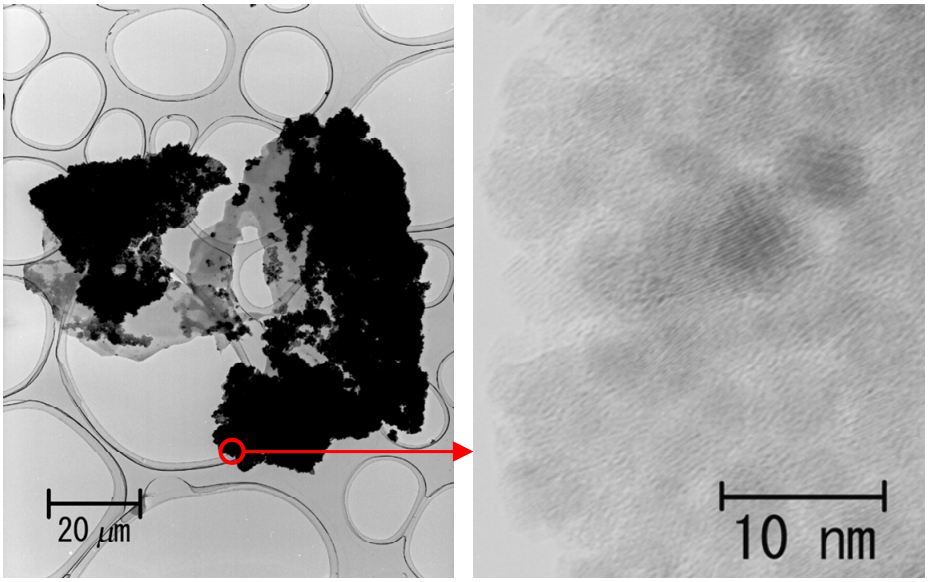

Fig. 3.2 TEM images of nano-sized γ-Fe_2O_3 crude product. Magnification: ×5,000 for the left, ×300,000 for the right. Membrane-like materials are organic impurity phase.

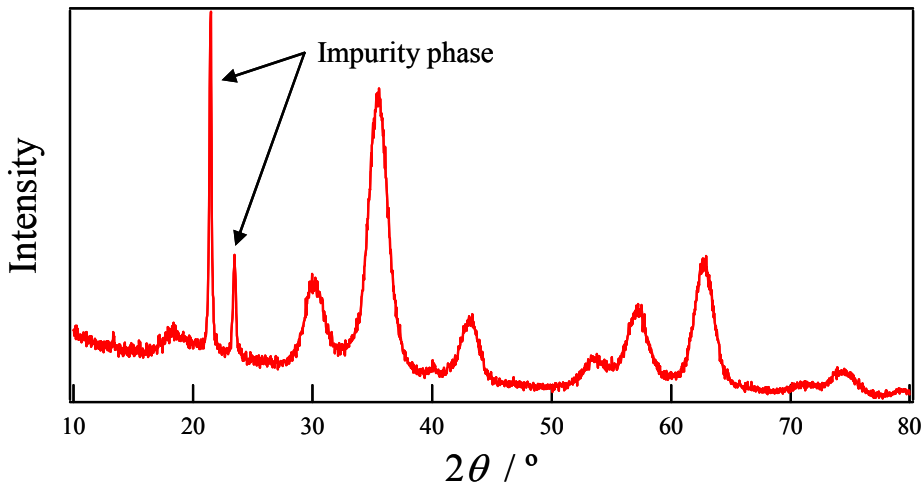

Fig. 3.3 XRD pattern of nano-sized γ-Fe_2O_3.

synthesis route shown in Fig. 3.1. In addition to the XRD peaks of γ-Fe_2O_3 (space group of $P4_332$)[3] two reflections were observed around the $2\theta = 20°$ and $2\theta = 24°$ which might be due to an impurity phase. Impurity phase in the products is not suitable for electrochemical measurement because of difficulty in estimating the actual sample weight and of possibility for the side reactions. The impurity phase was then tried to be identified and removed by the purification process.

3-3 Identification of the impurity phase

White color impurity phase was extracted from the crude product by bulb-to-bulb distillation apparatus, Kugelrohr (Aldrich)[4]. Identification was performed by XRD, FT-IR, ^{1}H NMR and ^{13}C NMR measurements. Figure 3.4 shows the XRD pattern of the impurity phase. Four large reflections, including two peaks shown in Fig. 3.3, were observed. However, the phase could not be identified by the JCPDS database. ^{1}H NMR and ^{13}C NMR spectra of the impurity phase with deuterated chloroform are shown in Fig. 3.5 and Fig. 3.6, respectivily. In ^{1}H NMR spectra, peaks arise from alkyl chain were observed around 0.7 ppm to 2.4 ppm, and peak due to methyl group was observed at 3.7 ppm. In the ^{13}C NMR spectra, peaks due to alkyl chain and alkene group were observed around 40 and 125 ppm, respectively, and peaks around 68 ppm and 210 ppm correspond to the tertiary amine and carboxyl group, respectively[5]. FT-IR spectrum of the impurity phase is shown in Fig. 3.7. Main absorption peaks (725 cm^{-1}, 964 cm^{-1}, 1380 ~ 1470 cm^{-1}, 1706 cm^{-1} and 2850 ~ 3000 cm^{-1}) may indicate the dimer of oleic acid[6-9]. TG-MS results indicated the existence of dimmer of oleic acid and other macromolecules which has lager molecular weight. These results indicate that the phase was composed of oleic acid related compounds, but the composition and the structure of these molecules are very complicated.

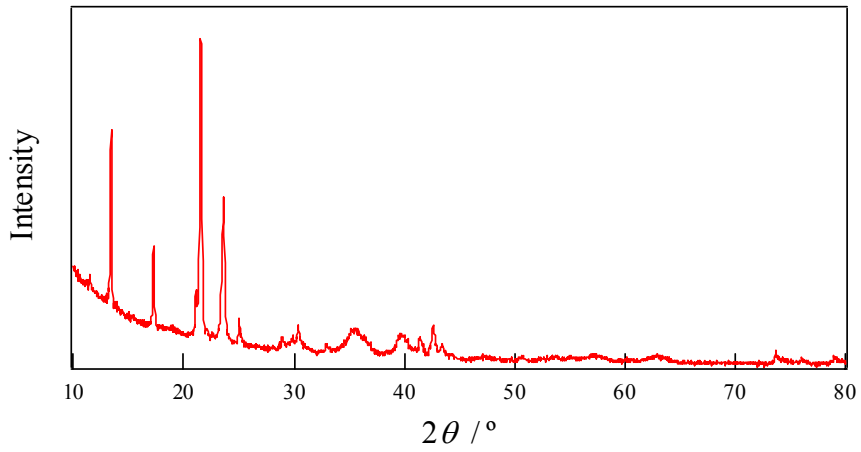

Fig. 3.4 XRD pattern of the impurity phase extracted from γ-Fe_2O_3.

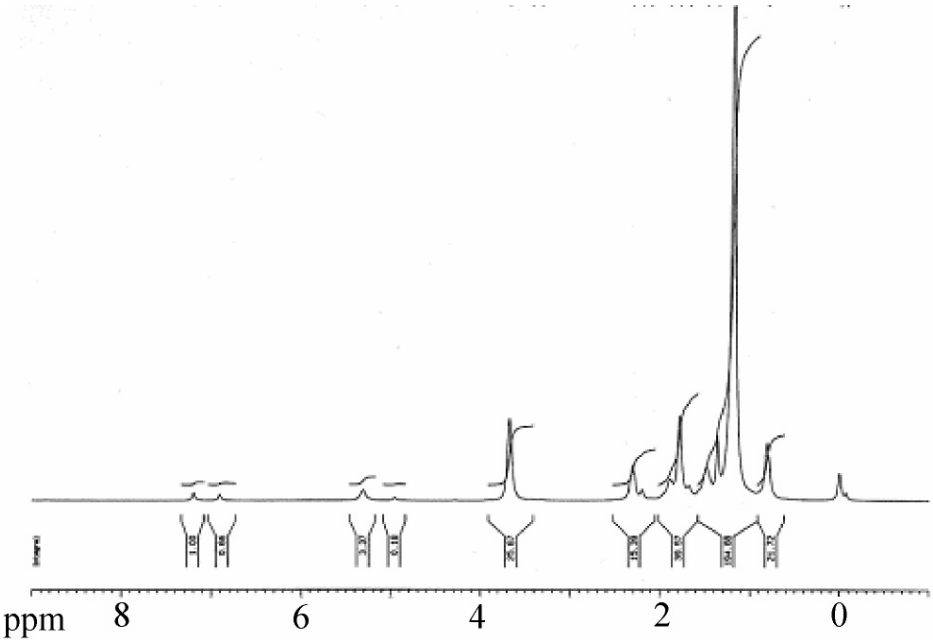

Fig. 3.5 ^{1}H NMR spectrum of the impurity phase extracted from γ-Fe_2O_3.

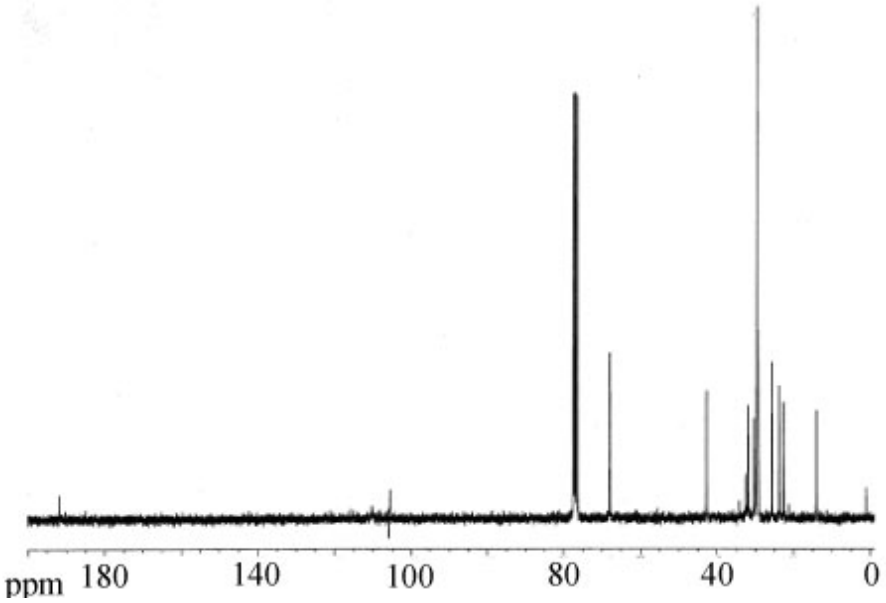

Fig. 3.6 ^{13}C NMR spectrum of the impurity phase extracted from γ-Fe_2O_3.

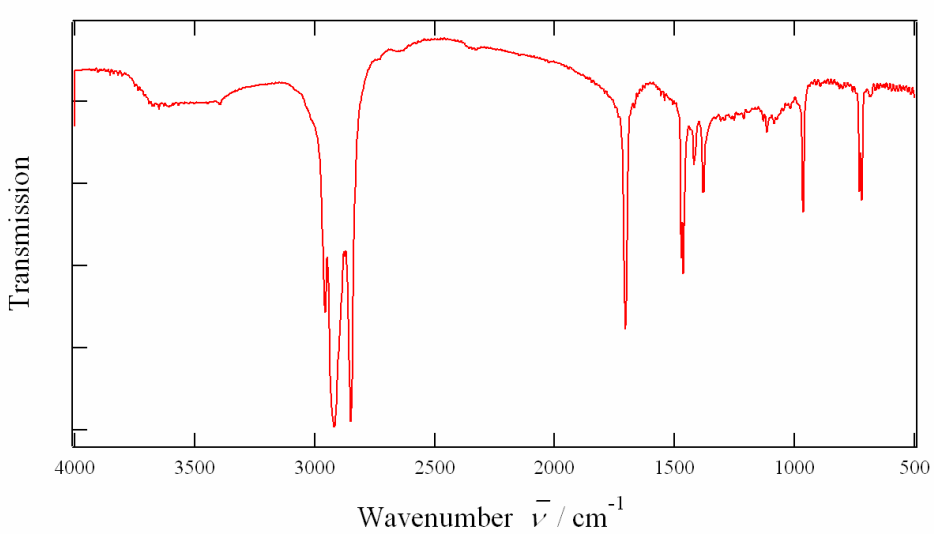

Fig. 3.7 IR spectrum of the impurity phase extracted from γ-Fe_2O_3.

3-4 Investigation of purification process

The organic impurity phases were removed using methods as follows: (i) washing by the solvent, (ii) vacuum drying with heat treatment and (iii) heat treatment under oxidation condition under an O_2 gas flow.

Method (i): washing by the solvent

This method is the most conventional and easiest way to remove the impurity phase, but it is difficult to adjust for the current system. This impurity phase was insoluble in almost organic/inorganic solvent, only partially soluble in chloroform, and solubility is not sufficient to remove all the impurity phase.

Method (ii); vacuum drying with heat treatment

Figure 3.8 shows the results of the TG-DTA measurement in an Ar gas flow. About 40% of weight loss was observed at 300°C ~ 400°C. Then a temperature of 400 °C is applied to remove impurity phase under reduction condition. Figure 3.9 shows XRD patterns of the products, before and after vacuum drying at 400 °C for 6h. Reflections of the impurity phase were disappeared, while shoulder-like reflection was observed at $2\theta = 38º$. Relative intensity of the peaks, $2\theta = 43º$ was higher than that of the sample before vacuum drying. Color of products after purification process changed form dark brown to black. These results indicate that the Fe_2O_3 phase was changed to Fe_3O_4 or FeO with partial oxygen defect. Figure 3.10 shows the TEM images of the products after vacuum drying. Membrane-like material was still observed. This material considered to be a residual organic impurity phase or carbonized impurity phase produced by the reduction condition. The method (ii) might not be efficient for purification of this product.

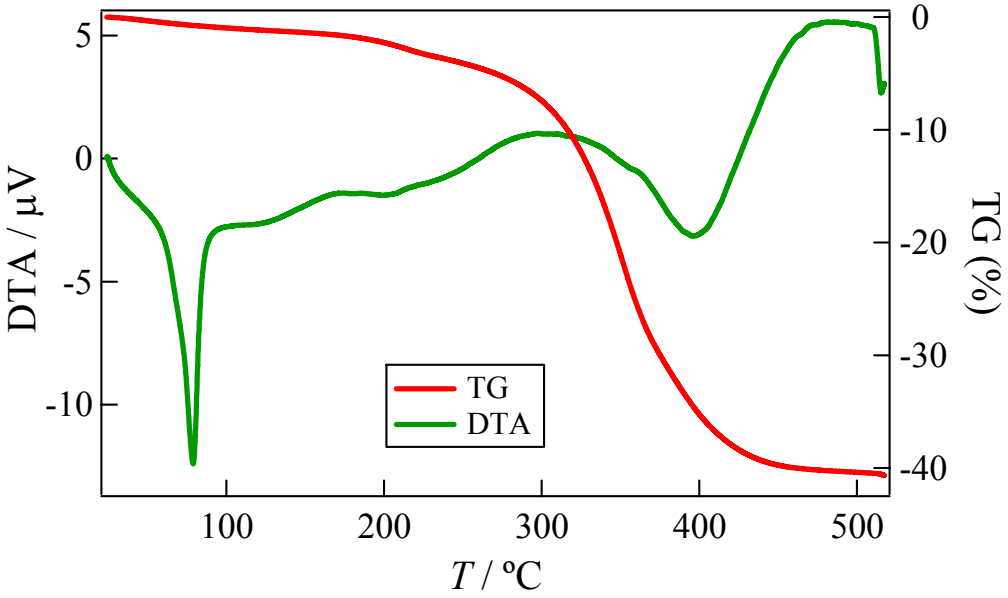

Fig. 3.8 TG-DTA profile of nano-sized γ-Fe_2O_3.

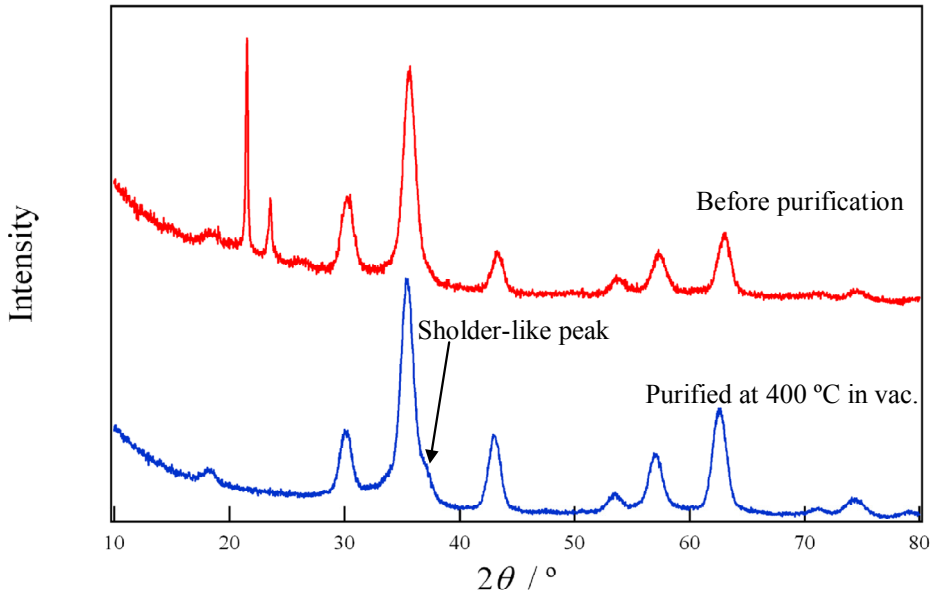

Fig. 3.9 XRD patterns of nano-sized γ-Fe_2O_3 before and after the purification at 150ºC for 20h in an oxygen atmosphere.

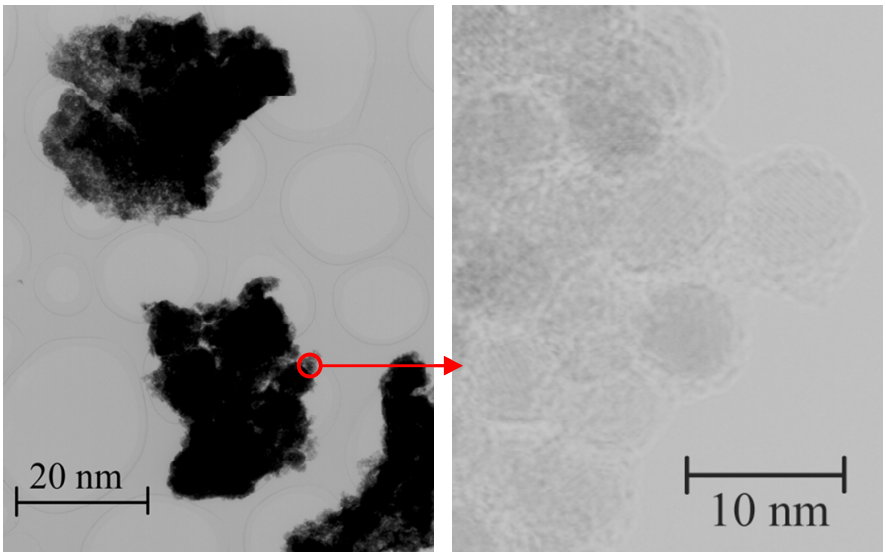

Fig. 3.10 TEM images of γ-Fe_2O_3 after heat treatment at 400ºC in vacuum.

Method (iii); heat treatment under oxidation condition

Figure 3.11 shows the results of the TG-DTA measurement in an oxygen gas flow. At 200ºC, the products were burned and the temperature increased to over 600ºC. Figure 3.12 shows TEM images of the product after heat treatment under oxidation atmosphere at 400ºC. Membrane-like material disappeared and crystal growth was observed. Purification by the oxidation condition was then effective to remove the impurity phase. Figure 3.13 shows the XRD patterns before and after the purification at 150ºC for 20h in an oxygen gas flow. Color of the products after purification process is light brown, indicative of γ-Fe_2O_3. No change in XRD measurement was observed for the patterns of γ-Fe_2O_3 except for the disappearance of impurity phase. Figure 3.14 shows the SEM image of the product after purification process. Particle size was very small (*c.a.* 8 nm) and homogeneous, and the crystal growth was suppressed.

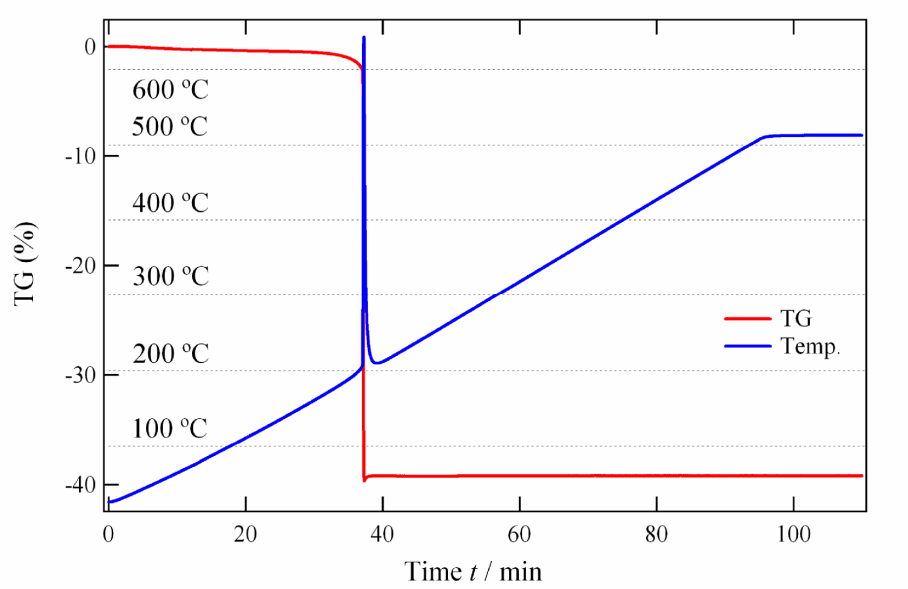

Fig. 3.11 TG-DTA profile of γ-Fe_2O_3 in oxygen atmosphere. Sample was burned at 200ºC.

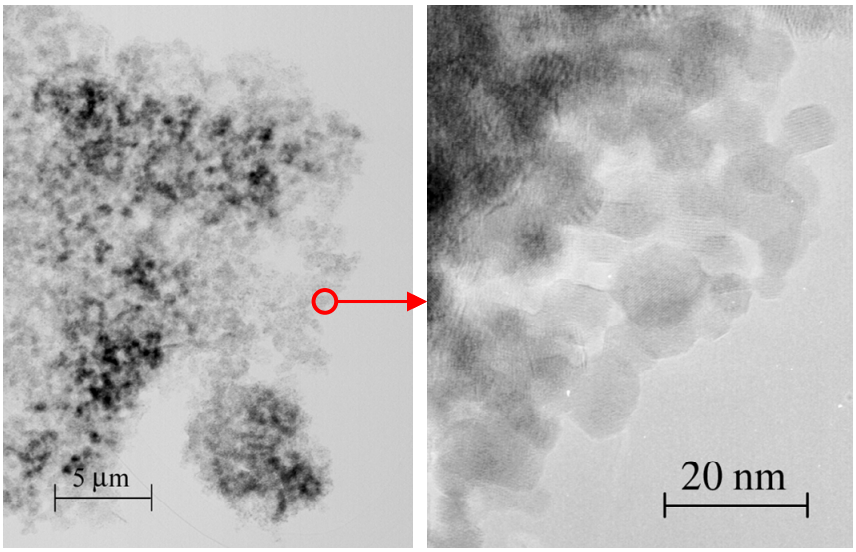

Fig. 3.12 TEM images of γ-Fe_2O_3 after heat treatment at 400ºC in air.

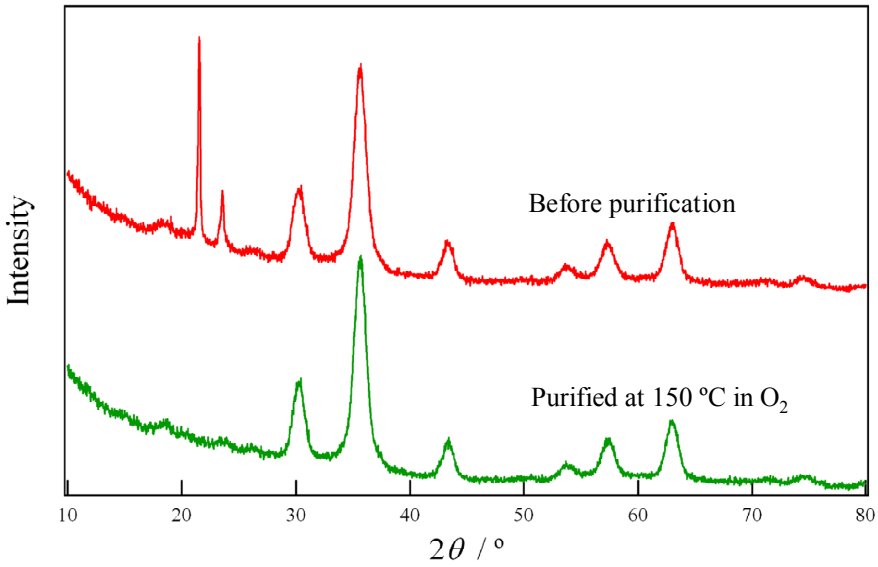

Fig. 3.13 XRD patterns of nano-sized γ-Fe_2O_3 before and after purification at 150ºC for 20h in an oxygen gas flow.

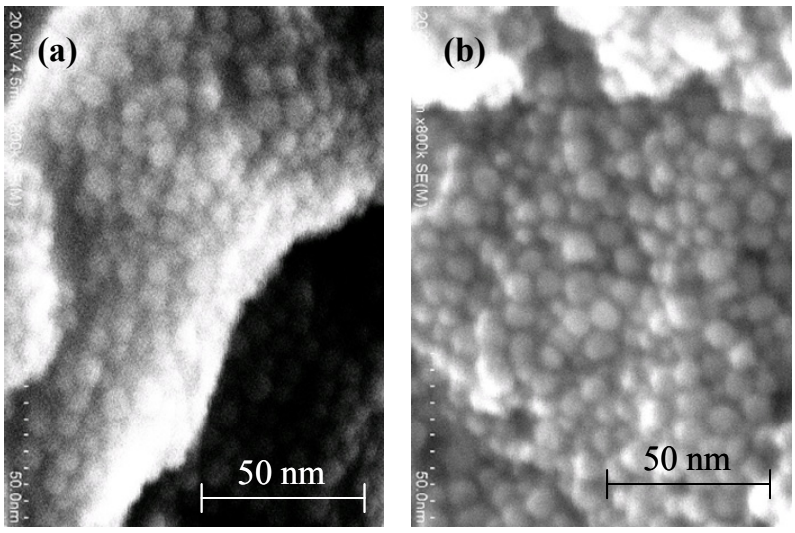

Fig. 3.14 SEM images of nano-sized γ-Fe_2O_3 (a) before, (b) after purification at 150ºC for 20h in an oxygen gas flow.

3-5 Conclusion

Nano-size γ-Fe_2O_3 synthesized by the mild oxidation of iron-micelle showed high crystalline and homogeneous products with small particle size. The synthesized compounds contain about 40 wt% of organic by-product as an impurity phase. Heat treatment was effective to remove impurity phases.

Reference

1. Material Science Society of Japan, *Ultrafine Particles as Materials (Shokabo Publishing Co. Ltd.)*, 12 (1993).
2. T. Hyeon, S. S. Lee, J. Park, Y. Chung and H. B. Na, *J. Am. Chem. Soc.*, **123**, 12798 (2001).
3. H.-S. Shin, *Yoop Hakhoechi*, **35**, 1113 (1998).
4. R. Graeve and G. H. Wahl, *J. Chem. Educ.*, **41**, 279 (1964).
5. L. A. Forato, V. E. Yushmanov and L. A. Colnago, *Biochemistry*, **43**, 7121 (2004).
6. T. Inoue, S.-I. Yanagihara, Y. Misono and M. Suzuki, *Chem. Phys. Lipids*, **109**, 117 (2001).
7. T. Inoue, Y. Hisatsugu, R. Ishikawa and M. Suzuki, *Chem. Phys. Lipids*, **127**, 161 (2004).
8. S. Chen and W. Liu, *Mater. Chem. Phys.*, **98**, 183 (2006).
9. N. Vlachos, Y. Skopelitis, M. Psaroudaki, V. Konstantinidou, A. Chatzilazarou and E. Tegou, *Anal. Chim. Acta*, **573+574**, 459 (2006).

Chapter 4

Electrochemical properties of nano-sized γ-Fe_2O_3

4-1 Introduction

Iron oxides have been considered to be difficult for the use of cathode material for lithium secondary battery due to their irreversible transformation from corundum/spinel phase to disordered rock-salt phase[1-3]. However, iron oxides with nano-sized particle are recently reported to react with lithium by a reversible process[4-8]. γ-Fe_2O_3 has the defect spinel structure in which a part of the octahedral sites in Fe_3O_4 is vacant. This may provides effective interstitial path for lithium transput property. Electrochemical properties of nano-sized γ-Fe_2O_3 are there for studied in the present study. The subjects focused in the present study are as follows: (i) to supperss the spinel/rock-salt transformation which presents reversible redox reaction, (ii) to maximize the lithium reactivity using huge surface area, and (iii) to improve reaction kinetics in the particles by minimizing diffusion distance.

In the pervious chapter, synthesis method and purification process of the nano-sized γ-Fe_2O_3 was investigated. In this chapter, electrochemical activities of synthesized nano-sized crystalline γ-Fe_2O_3 are studied; particle size effect, electrochemical behavior and cycle performance were clarified.

4-2 Particle size effect

Figure 4.1 shows the SEM images and the first discharge curves of γ-Fe_2O_3 with the particle size of 5, 20, and 30 ~ 50 nm. The 5 and 20 nm samples were synthesized by a protective colloid method, discussed in chapter 3, while the 30-50 nm sample was obtained by a conventional ceramic sintering process (TODA KOGYO CORP.).

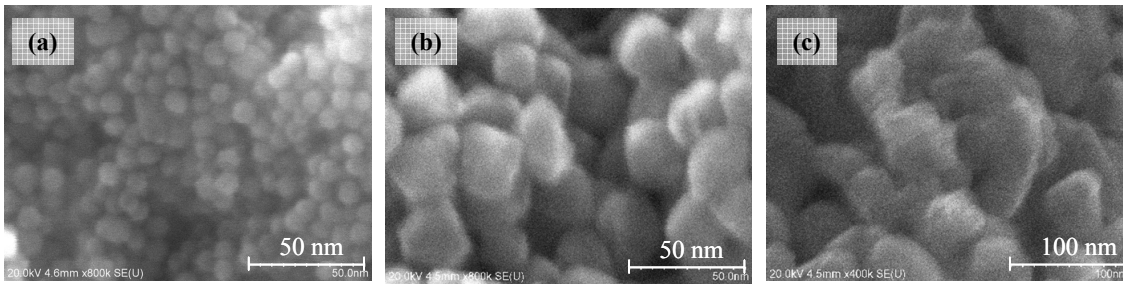

Fig. 4.1 SEM images of nano-sized γ-Fe_2O_3 with the particle size of (a) 7 nm, (b) 20 nm and (c) 30-50 nm, respectively. Magnetizations are ×800,000 for (a) and (b), ×400,000 for (c), respectively.

Figure 4.2 shows the first discharge curves of nano-sized γ-Fe_2O_3 with different particle size. Discharge capacities of the samples with the 5, 20 and 30-50 nm shows 205, 161 and 362 mAh/g, respectively. For the samples with the particle size of 5 and 20 nm, cell voltages decrease gradually to 1.0 V with a small slope change around 1.5 V. The sample with the particle size of 50 nm shows discharge capacities of 362 mAh/g with long plateau around 1.1 V region. For the large size and nano-sized α-Fe_2O_3, Larcher *et al.* reported similar plateau around 0.8 V [6]. They determined that the plateau corresponds to the decomposition of the electrolyte and a subsequent formation of an organic layer deposited on the surface of the particles. The plateau observed around 1.1 V may originated by similar reaction. The difference in the plateau voltage may be due to a difference in the reactivity between α-Fe_2O_3. and γ-Fe_2O_3 with the electrolyte (EC:DEC = 3:7 for this measurement and EC:DMC = 1:1 for Lancher's measurement). This plateau was only observed for the 50 nm particle, which might be due to a difference in the particle surface conditions which caused by the difference of the synthesis conditions.

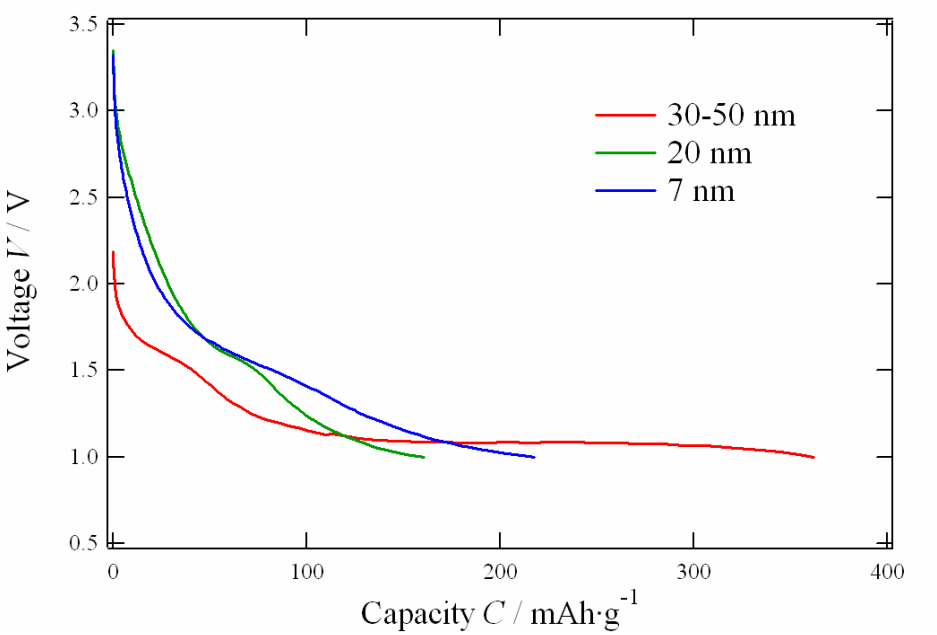

Fig. 4.2 First discharge curves of nano-sized γ-Fe_2O_3 with the particle size of 7 nm, 20 nm and 30-50 nm, respectively.

Figure 4.3 shows the ex-situ XRD patterns before and after the discharge process down to 1.0 V. For the particle size of 30-50 nm, spinel/disorder rock-salt phase transformation was observed, reflections of the disorder rock-salt phase was observed around 2θ = 37°, 43° and 62°. For the samples with smaller than 20 nm, spinel phase was observed during the discharge process with peak shifts to lower diffraction angles. These small particles might be suitable to apply for lithium secondary battery cathode.

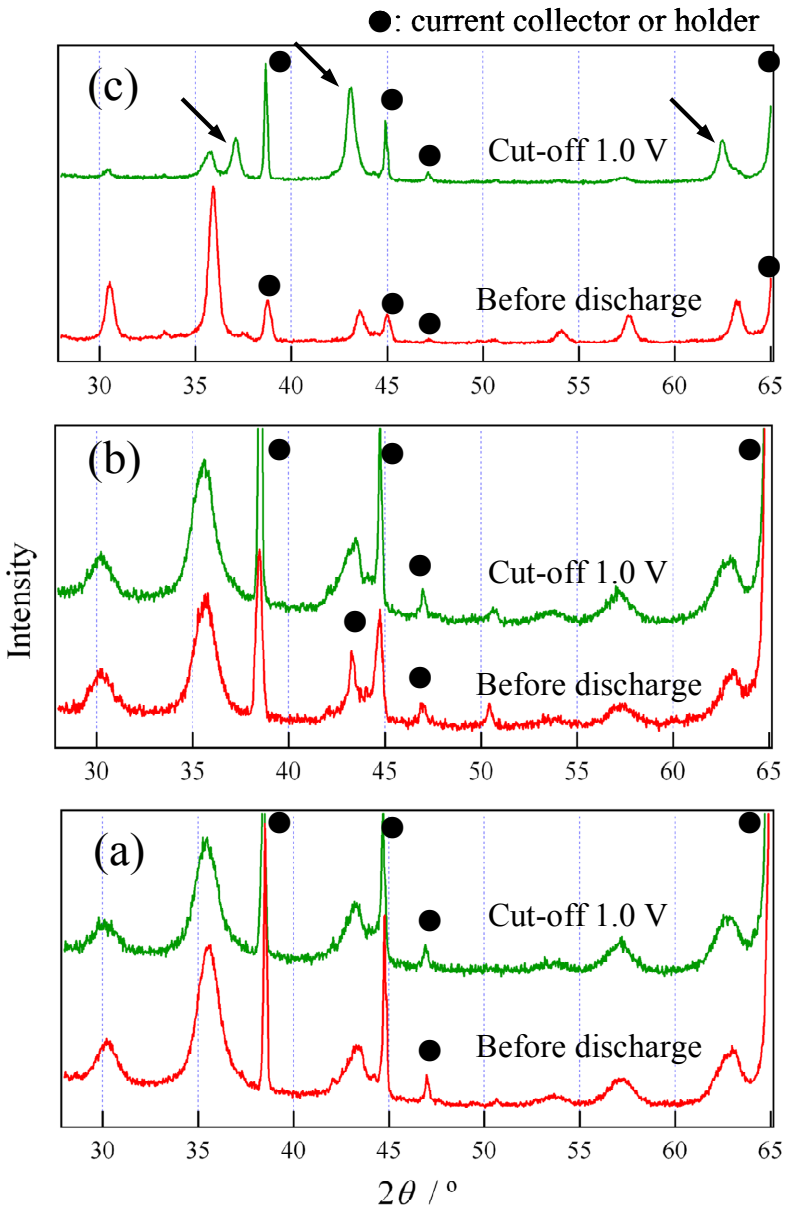

Fig. 4.3 XRD patterns of nano-sized γ-Fe_2O_3 with the particle size of (a) 5 nm, (b) 20 nm and (c) 30-50 nm. Red lines are before discharge, green lines are after discharge, and arrows indicate the disorder rock- salt phase.

4-3 Electrochemical behavior

Figure 4.4 shows the XRD patterns of ex-situ measurements for nano-sized γ-Fe_2O_3 with a particle diameter of *c.a.* 7 nm, during the first discharge process. The current density was 0.0565 mA/cm^2. The peaks shift to lower angles with the discharge and the increase of 004 reflection increased at 1.0 V. All the XRD peaks were indexed with the space group $P4_332$ maintaining the original framework of γ-Fe_2O_3 without nucleation or growth of another phase. The monotonic increase of the cubic lattice parameters as a function of the depth of discharge is summarized in Fig. 4.5, where approximately 0.25% expansion of lattice parameter (0.75% as a volume) was confirmed with an estimated ratio of $Li/Fe_2O_3 = 1.37$. Although a slight phase transformation seems to occur at the end of discharge as indicated by relative increase of 004 peak intensity in Fig. 4.4, the discharge process is essentially based on the topochemical reaction.

Mössbauer spectroscopy revealed that the valence state of Fe was Fe(III)/Fe(II) = 45/55 after discharge process(Fig. 4.6). The refined parameters are summarized in Table 4.1. This value corresponds to 193 mAh/g as a capacity, which is lower than the measured capacity of 230 mAh/g. This result indicates that some residual current is consumed to cause parasite reaction other than the lithium intercalation, such as adsorption of lithium on the particle surface or decomposition of electrolyte to form solid electrolyte interface (SEI) at the surface. Indeed, no incontinuous anomaly can be found in the bulk expansion during the discharge (Fig. 4.4 and Fig. 4.5).

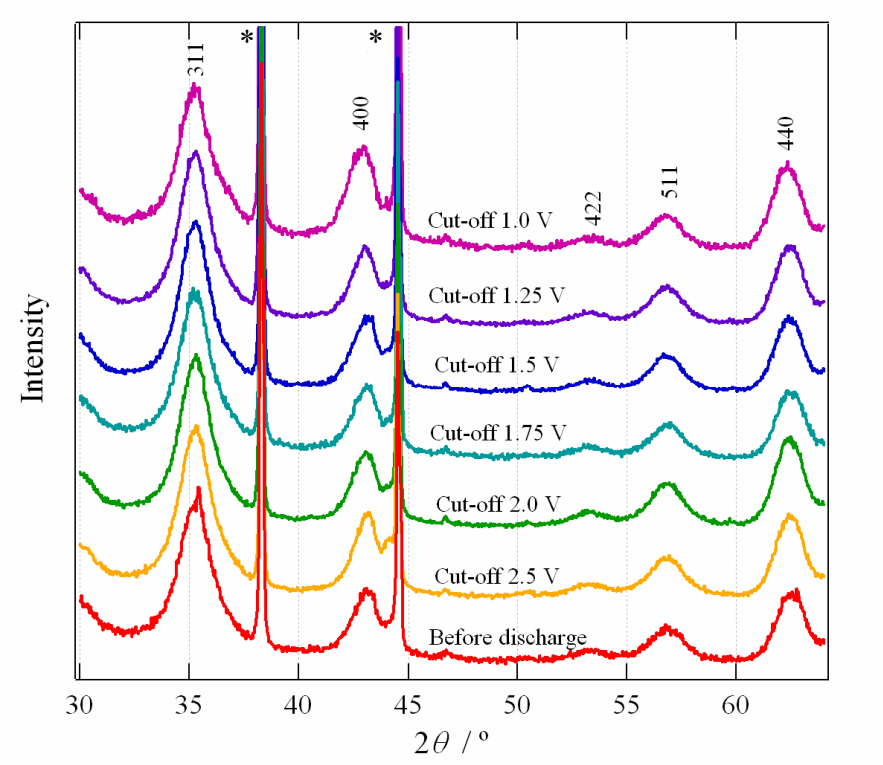

Fig. 4.4 *Ex-situ* X-ray diffraction patterns of nano-sized γ-Fe_2O_3 measured during the first discharge process. The discharge current density was 0.057 mA/cm^2. The peaks with asterisk label are diffractions from the Al current collector.

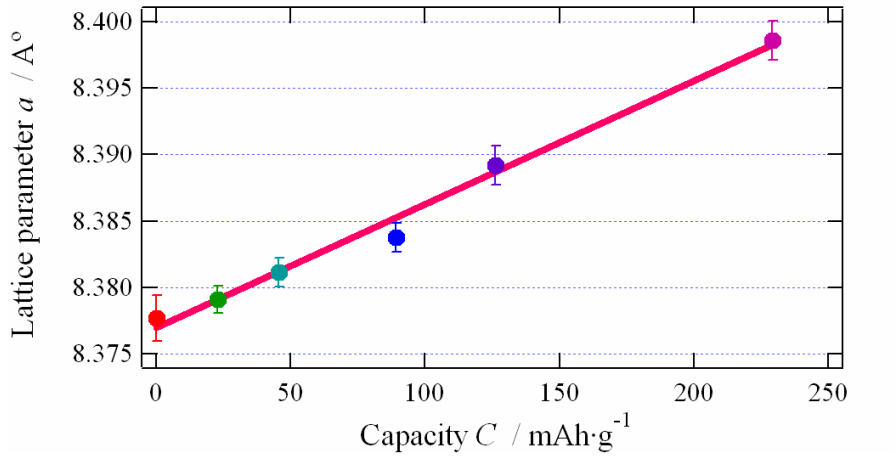

Fig. 4.5 Variation of the cubic lattice parameter during the first discharge process.

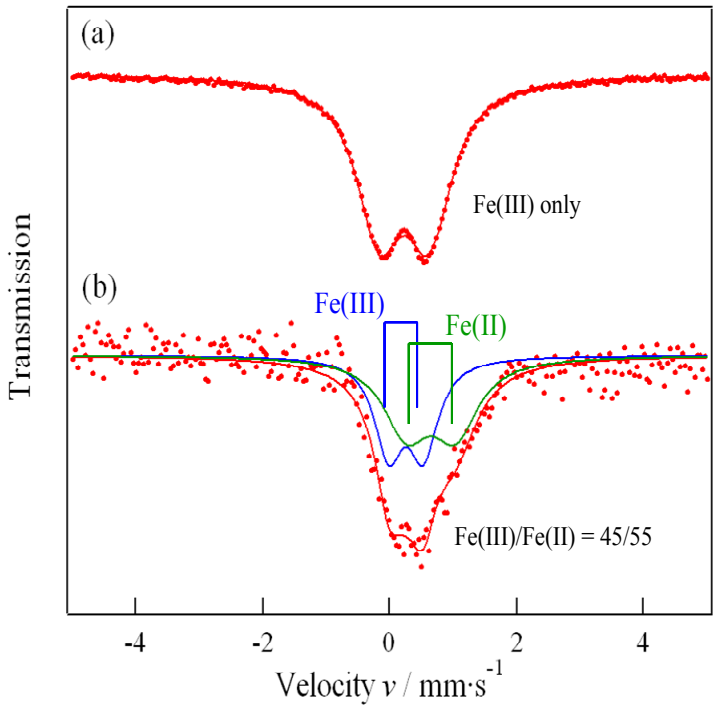

Fig. 4.6 Mössbauer spectrum for nano-sized γ-Fe_2O_3 (a) before discharge process, (b) after discharge process at 0.057 mA/cm^2 down to 1.0 V *vs.* Li/Li$^+$.

Table 4.1 Fitting parameters iron oxide of Mössbauer spectra before and after the electrochemical discharge experiments.

	Species	Quotient	*IS*	*QS*
Before discharge	Fe(III)	100	0.225	0.785
After discharge	Fe(II)	55.0	0.647	0.766
	Fe(II)	45.0	0.259	0.548

4-4 Cycle performance

The large irreversible capacity may also indicate the formation of SEI layer. Figure 4.7 shows the repeated charge-discharge curves of nano-sized γ-Fe_2O_3 under the current density of 0.1 mA/cm^2. The reaction is reversible, but huge irreversible capacity of over 140 mAh/g was observed at the first discharge process, and the subsequent capacity decreases upon repeated cycling is precipitous. Another possible reason of the large irreversible capacity and poor cycle performance may lie in the large difference in particle size between γ-Fe_2O_3 (~ 7 nm) and acetylene black (~ 35 nm). Efficient formation of the dense nano electron network with intimate contact would be an important future subject.

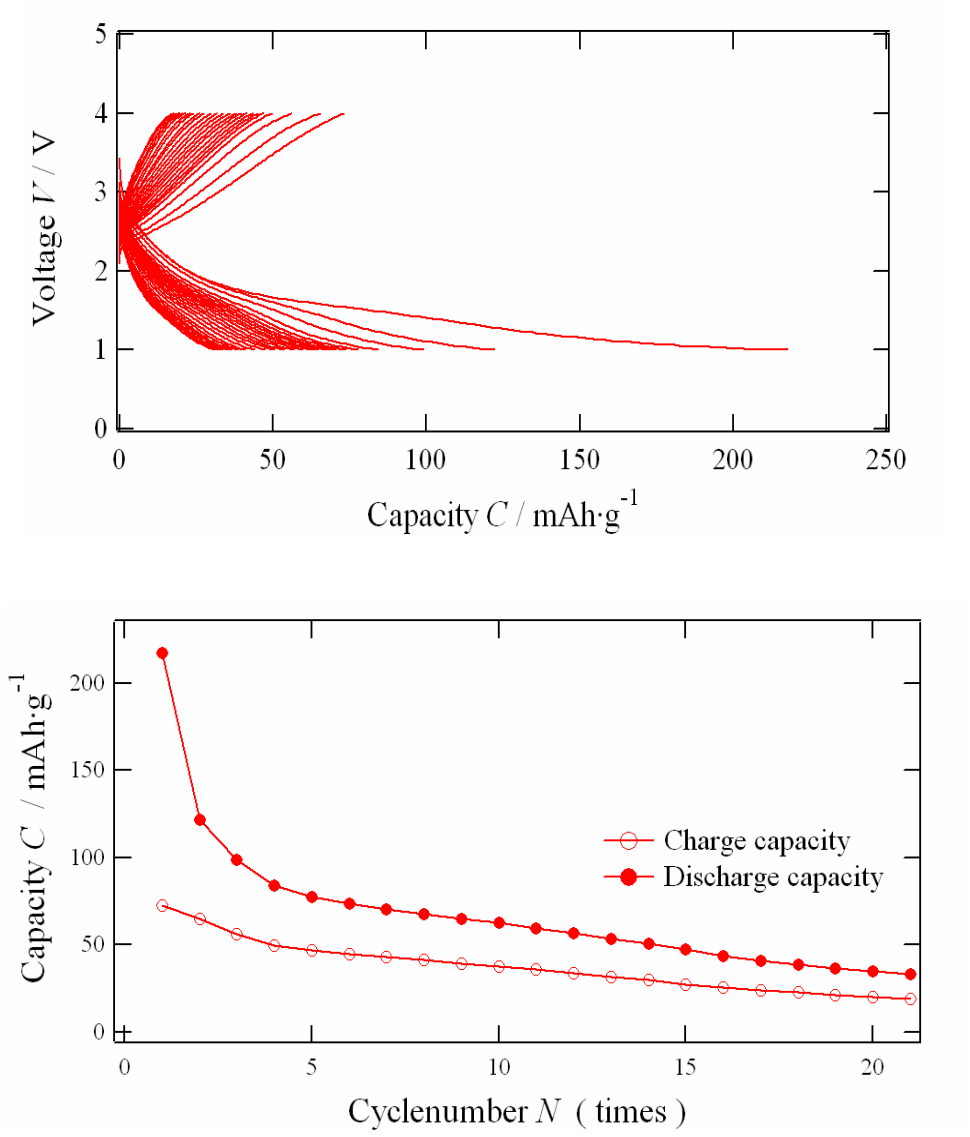

Fig. 4.7 (a) Repeated charge-discharge curves and (b) cycle characteristics of nano-sized γ-Fe_2O_3. Current density: 0.1 mA/cm^2.

4-5 Conclusion

Electrochemical reactivity of nano-sized γ-Fe_2O_3 with lithium was investigated. Particle diameter of under 20 nm are suitable for lithium secondary battery cathode. Nano-sized morphology led to the large capacity of about 230 mAh/g with improved reversibility based on the topochemical lithium intercalation without spinel/roc-ksalt transformation.

References

1. M. M. Thackeray, W. I. F. David and J. B. Goodenough, *Mater. Res. Bull.*, **17**, 785 (1982).
2. M. Pernet, P. Strobel, B. Bonnet, P. Bordet and Y. Chabre, *Solid State Ionics*, **66**, 259 (1993).
3. B. Bonnet, P. Strobel, M. Pernet, M. Gondrand, Y. Gros, C. Mouget and Y. Chabre, *Mater. Sci. Forum*, **91-93**, 345 (1992).
4. S. Komaba, K. Suzuki and N. Kumagai, *Electrochemistry (Tokyo, Japan)*, **70**, 506 (2002).
5. D. Larcher, D. Bonnin, R. Cortes, I. Rivals, L. Personnaz and J. M. Tarascon, *J. Electrochem. Soc.*, **150**, A1643 (2003).
6. D. Larcher, C. Masquelier, D. Bonnin, Y. Chabre, V. Masson, J. B. Leriche and J. M. Tarascon, *J. Electrochem. Soc.*, **150**, A133 (2003).
7. T. Matsumura, N. Sonoyama, R. Kanno and M. Takano, *Solid State Ionics*, **158**, 253 (2003).
8. S. Kanzaki, T. Inada, T. Matsumura, N. Sonoyama, A. Yamada, M. Takano and R. Kanno, *J. Power Sources*, **146**, 323 (2005).

Chapter 5

Effect of chemical oxidation for nano-size γ-Fe_2O_3 as lithium battery cathode

5-1 Introduction

The γ-Fe_2O_3 showed an irreversible transformation from the spinel to the rock-salt structure accompanied by the lithiation process, which caused low cycling characteristics for lithium battery electrodes. In order to overcome the irreversible characteristics, nano-size γ-Fe_2O_3 was synthesized and its electrochemical properties were clarified in chapter 4. The irreversible phase transformation was suppressed for the nano-size materials, and the reversible lithium intercalation and de-intercalation proceeded by a topochemical reaction[1]. However, only a low reversible capacity was observed, although relatively a large value of 230 mAh/g was obtained for the first discharge capacity.

There are several possibilities that caused low reversible characteristics. (i) Protons adsorbed on the surface of the particles react with lithium. (ii) Lithium insertion and extraction reactions caused aggregation of nano-size particles, which provided drastic degradation of reversibility. (iii) Impurity phases still exist on the nano-particle surface, which were deposited during the synthesis process, and the surface purification treatment was not efficient to remove these phases. We supposed that the surface protons or impurity phases might be the main reasons for its low reversible characteristics, because the particles had very small size (under 8 nm) and large surface area（140 m^2/g) without any morphology changes after the lithiation experiments.

In this chapter, the effect of chemical oxidation for nano-size γ-Fe_2O_3 was examined. The nano-particles synthesized by the Hyeon's[2] method were treated by chemical oxidation using NO_2BF_4. The electrochemical properties examined for γ-Fe_2O_3 after the oxidation process

provided better cycling characteristics with reversible phase transition between the spinel and the rock-salt structures, which was previously claimed to be irreversible process.

5-2 Effect for the structures and morphologies

Chemical oxidation is one of the effective techniques of di-protonation and to remove residual impurity phases. We chose NO_2BF_4 as an oxidant and acetonitrile as an aprotic solvent. NO_2BF_4 is a strong oxidant with an oxidation potential higher than 5 V, which is efficient to obtain high oxidized materials[3]. The nano-particles of γ-Fe_2O_3 were treated with the chemical oxidation. Figure 5.1 shows the XRD patterns of nano-size γ-Fe_2O_3 before and after the chemical oxidation. No significant change was found in the diffraction patterns with the chemical oxidation. The lattice parameters were calculated to be a = 8.3472(6) and 8.3472(7) Å for the samples before and after the oxidation, respectively, indicating no changes in the bulk structure with the chemical oxidation process. Figure 5.2 shows the SEM images of nano-size γ-Fe_2O_3 before and after the chemical oxidation process. No morphology change with the chemical treatment was confirmed. These results indicate that the chemical oxidation process caused no influence on the structures, particle size, and morphology of γ-Fe_2O_3. Figure 5.3 shows the TG curves of nano-size γ-Fe_2O_3 before and after the chemical oxidation together with the sample after immersed in acetonitrile. A weight loss of 9 wt% was observed for the sample before chemical oxidation and treated with acetonitrile. As the samples treated with NO_2BF_4 showed a weight loss of about 6 wt%, about 3 wt% of residual impurity phase was removed by the oxidation.

The TG measurements indicated that the phase synthesized by the Hyeon's method contained an impurity phase, which could be removed both by thermal treatment and the chemical oxidation process. Details of the impurity phase were discussed in chapter 3. Figure 5.4 shows the FT-IR spectra of nano-size γ-Fe_2O_3 before and after the chemical oxidation process, and a residual phase extracted by the distillation process[4]. The IR spectra showed peaks around 2900

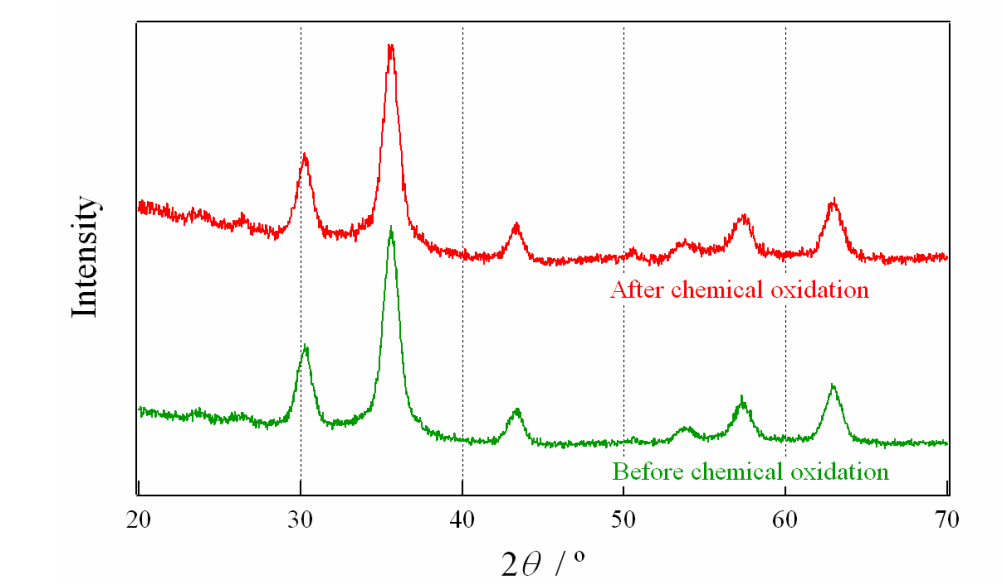

Fig. 5.1 XRD patterns of nano-size γ-Fe_2O_3, before (bottom) and after (top) chemical oxidation.

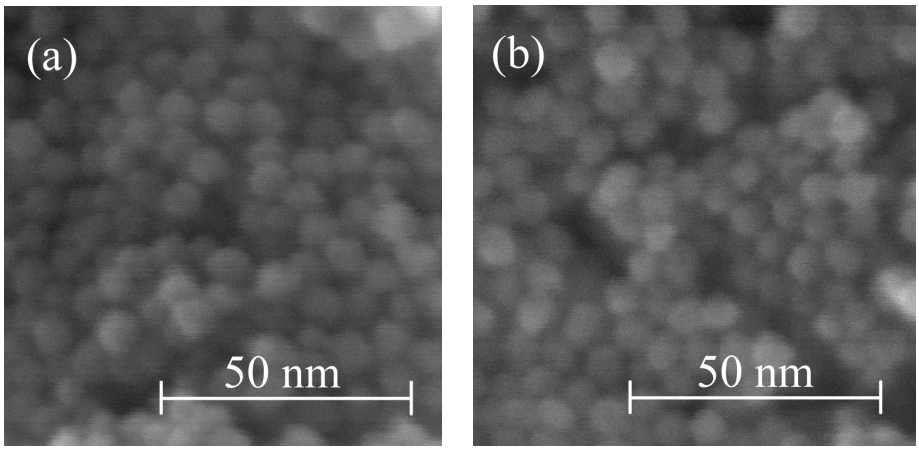

Fig. 5.2 SEM images of nano-sized γ-Fe_2O_3, (a) before and (b) after chemical oxidation. Magnification: ×800,000.

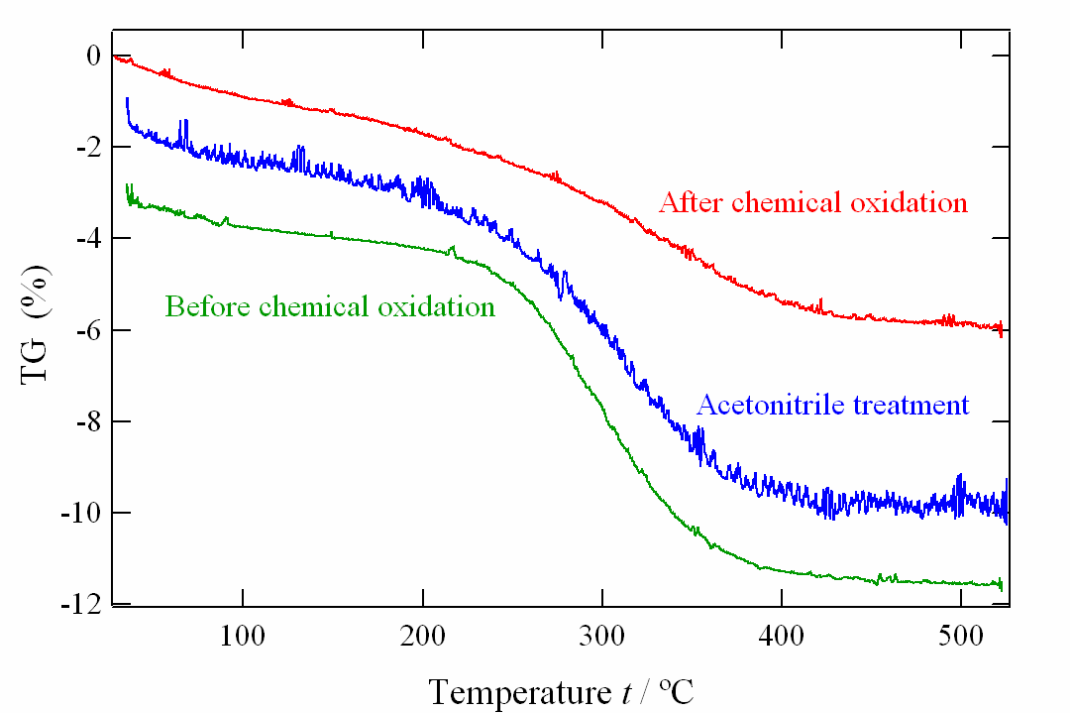

Fig. 5.3 TG curves of nano-size γ-Fe_2O_3, before chemical oxidation (bottom), after chemical oxidation (top) and after immersed in acetonitrile solution (middle). For clarity, the data for acetonitrile treatment and before chemical oxidation are offset 1% and 3%, respectively.

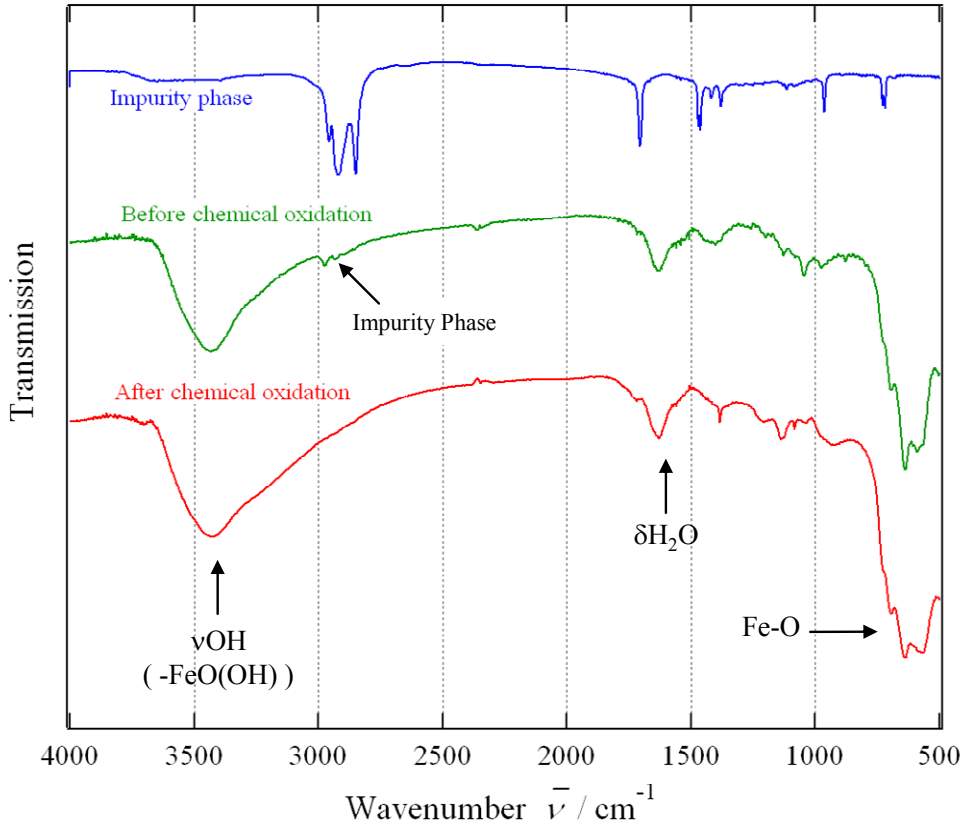

Fig. 5.4 FT-IR spectrum for nano-size γ-Fe_2O_3, before chemical oxidation (middle), after chemical oxidation (bottom), and the impurity phase extracted by evaporation method (top). Impurity phase was observed for the sample before chemical oxidation.

cm^{-1} characteristic of the residual impurity phase[5-7]. After the chemical oxidation, these peaks disappeared for the nano-size γ-Fe_2O_3, indicating that the surface impurity phase was removed by the chemical oxidation treatment. On the other hand, no significant changes were observed for the peaks around 1380 and 1640 cm^{-1}, and 3400 cm^{-1}, which correspond to H_2O, and –O(OH) on the surface, respectively[8, 9]. These results indicated that the chemical oxidation was efficient to remove the impurity phase on the surface of nano-size γ-Fe_2O_3 particles, but the process was not efficient to remove protons which were adsorbed or chemically bonded on the surface.

5-3 Effect for the electrochemical behaviors

Figure 5.5 shows the first discharge curves of the nano-size γ-Fe_2O_3 before and after the chemical oxidation process. The cut-off voltage was 1.0 V. The discharge capacities of 200 mAh/g for the sample before chemical oxidation increased to 236 mAh/g after the treatment; about 18 % of its discharge capacity was increased with the chemical oxidation process. Figure 5.6 shows the *ex-situ* XRD patterns of the chemically oxidized γ-Fe_2O_3 and the lithiated γ-Fe_2O_3. The XRD patterns of the lithiated γ-Fe_2O_3 were measured for the samples after discharged to 1.0 V (4.0 V in the figure), and the sample after charged from 1.0 to 4.0 V (4.0 V in the figure). For the sample discharged to 1.0 V, new peaks appeared around $2\theta = 37^\circ$ and 43º attributed to the disordered rock-salt phase, which indicates a phase transformation from the spinel to the disordered rock-salt phase. In the pervious section, it was reported that the irreversible spinel/rock-salt phase transformation was suppressed by making nano-particles, while the micro-size particles showed the irreversible spinel/rock-salt phase transition[10]. However, a larger amount of lithium inserted into the nano-particles by the surface treatment of chemical oxidation caused the phase transformation from the spinel to the rock-salt type. The amount of the rock-salt phase produced from the spinel structure was estimated by fitting XRD patterns with the Rietveld method; a ratio of the spinel/rock-salt phase was determined to be 0.2/0.8. The fitting pattern of the sample discharged to

1.0 V is shown in Fig. 5.7.

Figure 5.8 shows the Mössbauer spectra of nano-size γ-Fe_2O_3 before and after the discharge processes. The refined parameters are summarized in Table 5.1. Nano-size γ-Fe_2O_3 before discharge showed the existence of Fe(III), while a mixed valence state was observed with a ratio of Fe(III)/Fe(II) = 57/43 after the discharge. Bonnet *et al.* reported that the transformation from the spinel to the disordered rock-salt phase proceeded when the amount of 0.87 Li was reacted with γ-Fe_2O_3 in the bulk crystalline materials[10]. Assuming that the lithium content of the rock-salt phase was 0.87, the composition of the spinel phase was calculated to be $Li_{0.82}Fe_2O_3$ using the amount of spinel/rock-salt phase ratio and the Fe(III)/Fe(II) ratio determined by XRD and Mössbauer spectroscopy, respectively. The XRD pattern fitting analysis for the sample after charge to 4.0 V provided a spinel/rock-salt ratio of 0.5/0.5, clearly indicating that the disordered rock-salt phase transformed again to the spinel structure with the charge process; the reversible spinel/rock-salt transformation was found for our ultra fine nano-particles. Details of reaction process will discuss in chapter 6.

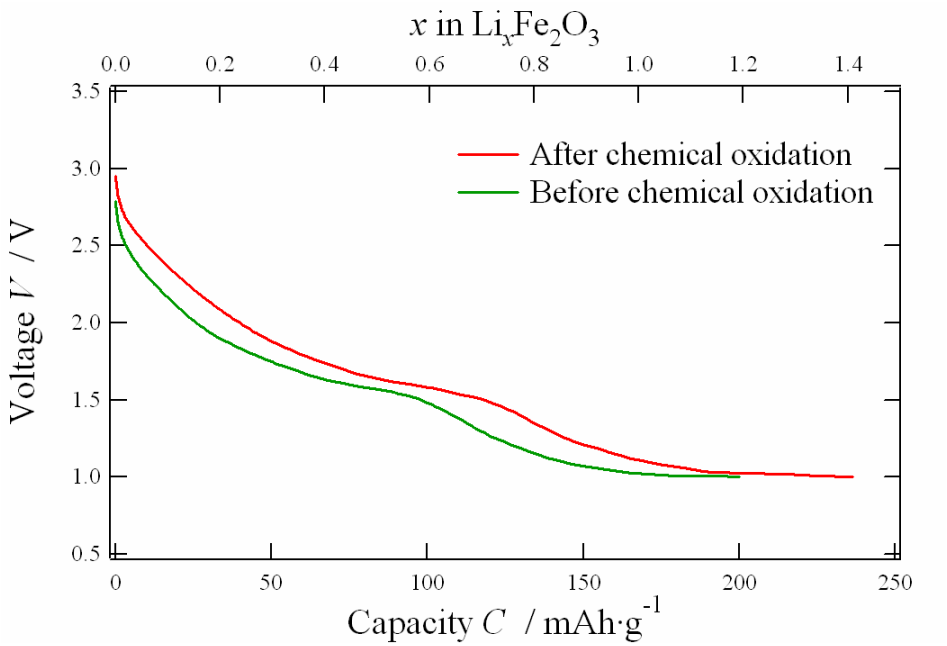

Fig. 5.5 First discharge curves for nano-size γ-Fe_2O_3 before chemical oxidation process (green line) and after chemical oxidation process (red line). Conditions; cut-off voltage: 1.0 V, current density: 0.05 mA/cm^2.

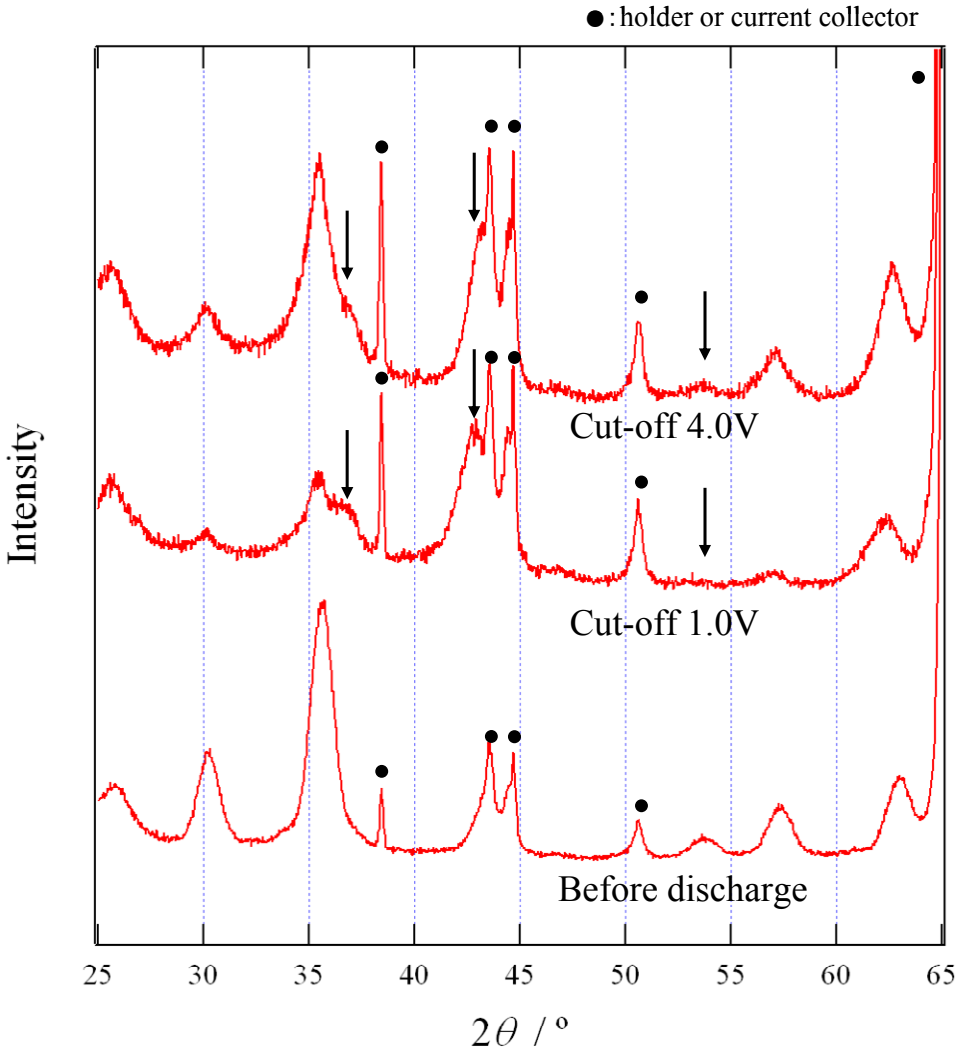

Fig. 5.6 XRD patterns of nano-size γ-Fe_2O_3, before and after the discharge process. The mark,●, indicate the current collector or XRD holder. Arrows indicate the reflections which changed.

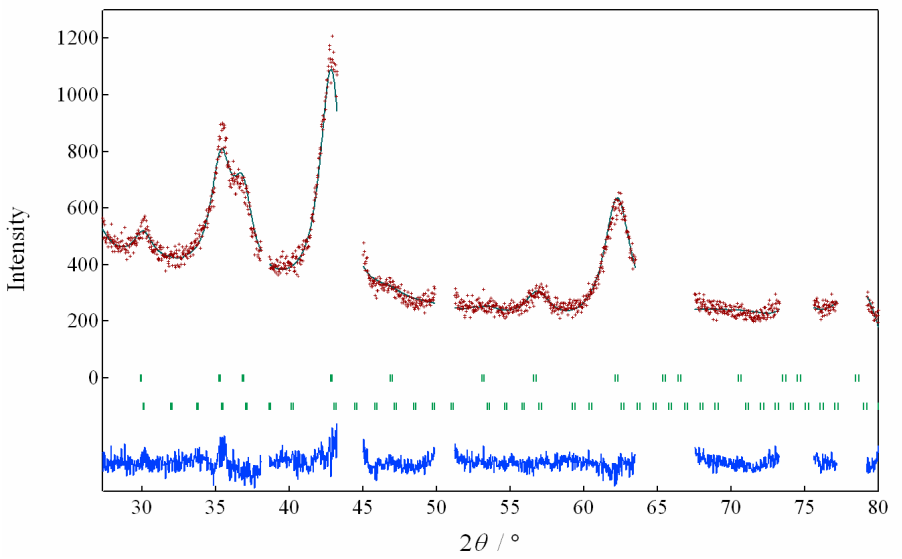

Fig. 5.7 Rietveld refinement pattern of lithiated γ-Fe_2O_3 to a cut-off voltage of 1.0 V. The diffraction angles near the peaks due to current corrector and diffraction holders were

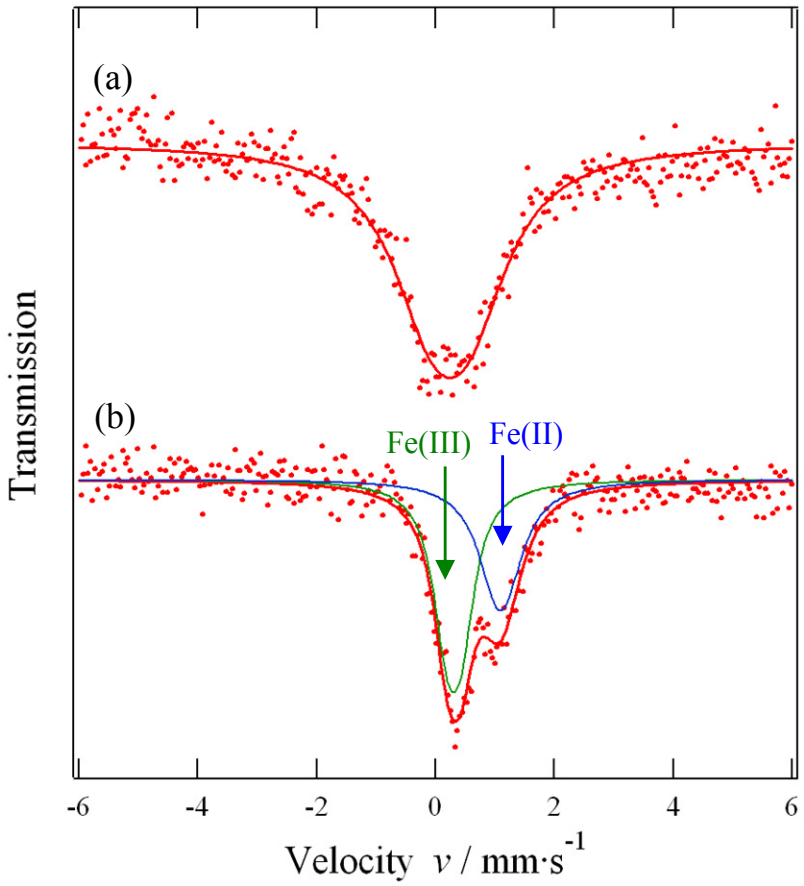

Fig. 5.8 Mössbauer spectra of nano-size γ-Fe_2O_3. (a) Initial state and (b) after discharge process down to 1.0 V *vs.* Li/Li^+.

Table 5.1 Fitting parameters iron oxide of Mössbauer spectra before and after the electrochemical discharge experiments.

	Species	Quotient	*IS*	*QS*
Before discharge	Fe(III)	100	0.225	0.785
After discharge	Fe(II)	43.1	1.094	0.154
	Fe(III)	56.9	0.306	0.241

5-4 Effect for the battery performance

Figure 5.9(a) shows charge-discharge curves of the nano-size γ-Fe_2O_3 after the chemical oxidation with a current density of 0.05 mA/cm^2 (about 0.7 C rate) and cut-off voltages of 1.0 and 4.0 V for the discharge and charge, respectively. Figure 5.9(b) shows the cycling characteristics of γ-Fe_2O_3 before and after the chemical oxidation. The chemical treatment improved the cycling characteristics. However, a large irreversible capacity was still observed; a reaction between lithium and the surface caused an irreversible reaction. The irreversible capacity was about 75.3 mAh/g, which corresponds to the nominal composition of 0.45 Li for γ-Fe_2O_3.

In the present study, the importance of surface conditions and phase transition mechanism of the nano-particles for electrochemical reactions were indicated. As the nano-particles provided large surface area, the control of the surface conditions is very important for the electrochemical characteristics. The main impurity phase formed during the synthesis process was successfully removed by our chemical treatment, and the reversible lithium capacity was improved. However, the FT-IR and TG characterization of the nano-particles indicated that there are still residual protons on the surface, and the surface condition of the nano-particles was found to be an important factor that determines both the capacity and reversibility of electrode characteristics.

In the present study, the reversible spinel/rock-salt phase transition was confirmed for the nano-particles, although a complete phase change was not observed during the first charge-discharge cycle for the present samples. Reversible phase transition with the lithium (de-)intercalation into the γ-Fe_2O_3-type spinel structure may indicate further possibility to improve reversible capacities of the nano-particles.

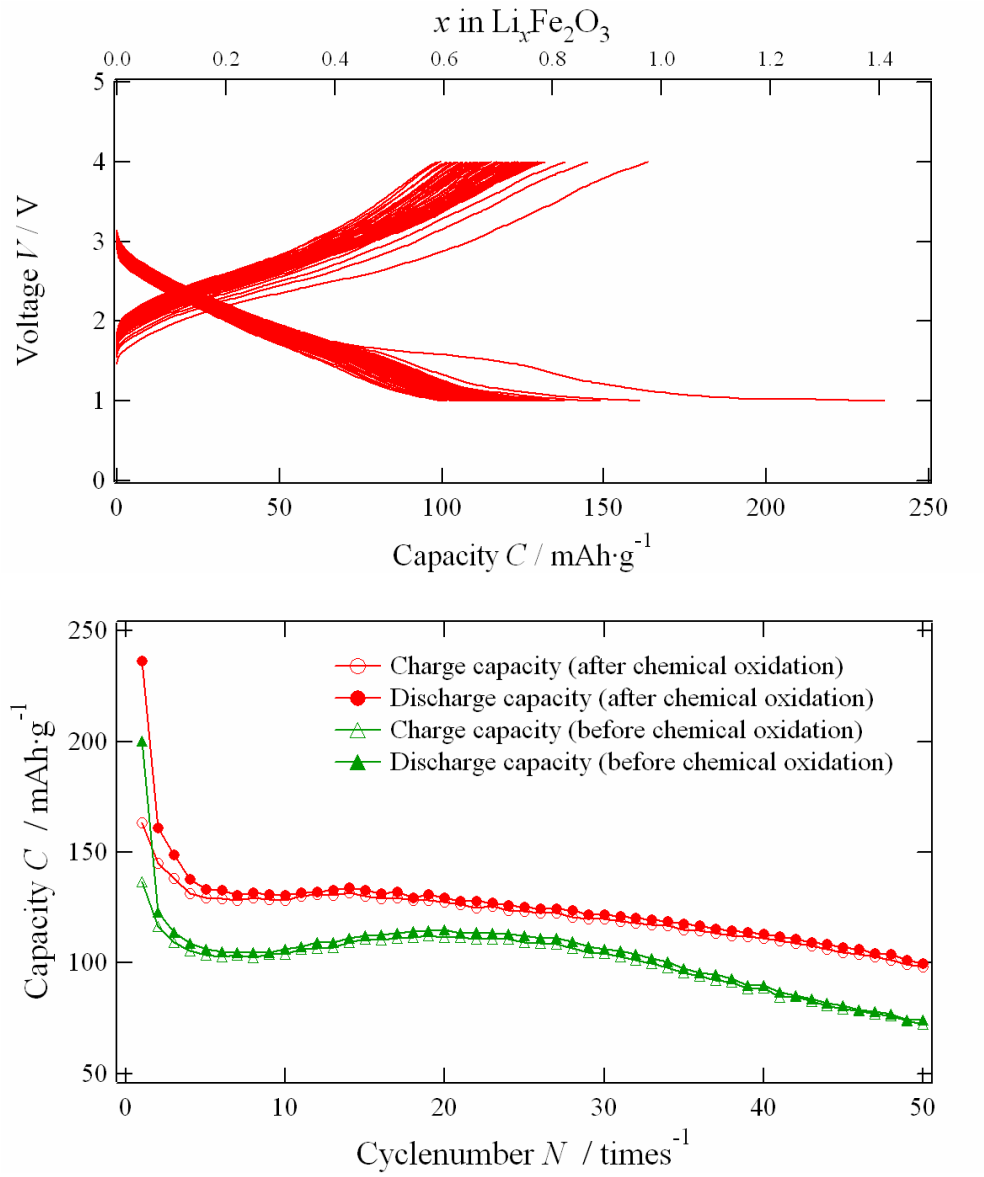

Fig. 5.9 (a) Charge-discharge curves of nano-size γ-Fe_2O_3. Conditions: cut-off voltage: 1.0 V and 4.0 V; current density: 0.05 mA/cm^2. (b) Cycle number dependence of charge/discharge capacities of nano-size γ-Fe_2O_3 before and after chemical oxidation process.

5-5 Conclusion

We investigated the effect of chemical oxidation with NO_2BF_4 for nano-size γ-Fe_2O_3. The chemical oxidation removed the residual impurity phase without any changes in particle size and morphology of the nano-particles. The sample after chemical oxidation showed larger charge-discharge capacity with better cycling characteristics. The increase in the amount of lithium intercalated into the structure (discharge capacity) caused a phase change from the spinel to the rock-salt structure, which was not observed for the samples with no chemical oxidation process. However, the reversible behavior of the spinel/rock-salt phase transition may indicate a possibility of capacity increase in the spinel-type iron oxides. The chemical oxidation process is efficient to improve electrochemical characteristics of nano-particles with high surface area. However, large surface area of the nano-particles affects the electrochemical properties and the control of the surface conditions is an important factor to improve the capacity.

References

1. S. Kanzaki, T. Inada, T. Matsumura, N. Sonoyama, A. Yamada, M. Takano and R. Kanno, *J. Power Sources*, **146**, 323 (2005).
2. T. Hyeon, S. S. Lee, J. Park, Y. Chung and H. B. Na, *J. Am. Chem. Soc.*, **123**, 12798 (2001).
3. A. R. Wizansky, P. E. Rauch and F. J. Disalvo, *Journal of Solid State Chemistry*, **81**, 203 (1989).
4. R. Graeve and G. H. Wahl, *J. Chem. Educ.*, **41**, 279 (1964).
5. T. Inoue, Y. Hisatsugu, R. Ishikawa and M. Suzuki, *Chem. Phys. Lipids*, **127**, 161 (2004).
6. S. Chen and W. Liu, *Mater. Chem. Phys.*, **98**, 183 (2006).
7. N. Vlachos, Y. Skopelitis, M. Psaroudaki, V. Konstantinidou, A. Chatzilazarou and E. Tegou, *Anal. Chim. Acta*, **573+574**, 459 (2006).
8. S. Music, G. P. Santana, G. Smit and V. K. Garg, *J. Alloys Compd.*, **278**, 291 (1998).
9. X. Liu, M. D. Kaminski, Y. Guan, H. Chen, H. Liu and A. J. Rosengart, *J. Magn. Magn. Mater.*, **306**, 248 (2006).
10. B. Bonnet, P. Strobel, M. Pernet, M. Gondrand, Y. Gros, C. Mouget and Y. Chabre, *Materials Science Forum*, **91-93**, 345 (1992).

Chapter 6

Investigation of the reaction process for nano-size γ-Fe_2O_3 with lithium ions

6-1 Introduction

Nano-sized γ-Fe_2O_3 indicated reversible electrochemical reactivity, as shown in chapter 4 and chapter 5. *Ex-situ* XRD measurements indicated reversible spinel/rock-salt phase transformation, which was reported to be an irreversible reaction for the large size particles[1]. This reversible reactivity was typical for the nano-sized particles[2, 3]. While results on Mössbauer spectroscopy indicated that the discharge process proceeded by a reduction of iron together with a reaction mechanism which was not explained by a Fe(III)/Fe(II) redox. However, the mechanism was not clarified.

In this chapter, details of the lithiation process of nano-sized γ-Fe_2O_3 were studied by neutron scattering technique together with the conventional X-ray diffraction measurement. Chemical lithiation was used to perpetrate the lithiated samples for neutron measurements[4, 5] because the additives such as acetylene black and PVdF used for electrochemical measurements affect the background of neutron scattering. Structure changes of the bulk structures were determined by neutron powder diffraction measurement with the Rietveld analysis, the local structures were analyzed by neutron total scattering with pair distribution function. Based on the structural information, electrochemical lithiation mechanism was discussed for nano-sized γ-Fe_2O_3.

6-2 Synthesis and structure

The samples used for neutron scattering were prepared by the same method discussed in chapter 5. Figure 6.1 shows the X-ray diffraction patterns of the nano-sized γ-Fe_2O_3 synthesized.

The broad refractions were obtained because these materials were huge small particles. Structure parameters were refined with the space group $P4_332$ using a model: Fe at the octahedral sites, 4*b* (5/8, 5/8, 5/8), 12*d* (1/8, *y*, -*y*+1/2); Fe at the tetrahedral site, 8*c* (*x*, *x*, *x*); and O at 8*c* (*x*, *x*, *x*) and 24*e* (*x*, *y*, *z*). No impurity phase was observed for the XRD measurement. During the refinements, isotropic atomic displacement parameters, U_{iso}, were fixed. The obtained *R* factors and structural parameters were presented in Table 6.1. For the bulk materials of γ-Fe_2O_3, site occupations of the iron in the 4*b*, 8*c* and 12*d* sites were reported to be 0.35, 1.0 and 0.98, respectively[6]. However, the nano-sized materials in the present study showed the Fe occupation parameters of 0.494, 0.941 and 0.845 for the 4*b*, 8*c* and 12*d* sites, respectively. The occupancy of 4*b* site in the nano-sized γ-Fe_2O_3 was increased, and those of 8*c* site and 12*d* site decreased. More disordered orientation was observed for the nano-sized materials.

X-ray diffraction and neutron diffraction were measured for the lithiated γ-Fe_2O_3 with nano-sized particles. The lithiated sample was synthesized by a chemical lithiation technique using *n*-BuLi in hexane solvents. Several types of cation disorder and vacancy models were used for the refinements, and finally lithiated material was refined as a two-phase mixture with the spinel type structure; a defect spinel phase with the space group of $P4_332$, and a disordered rock-salt phase with the space group of *Fd*-3*m*, for the phase I and the phase II, respectively. The initial coordinates for the phase I with the space group $P4_332$ were as follows: Fe and Li at the octahedral sites, 4*a* (1/8, 1/8, 1/8), 4*b* (5/8, 5/8, 5/8), 12*d* (1/8, *y*, -*y*+1/2); Fe at the tetrahedral site, 8*c* (*x*, *x*, *x*); and O at 8*c* (*x*, *x*, *x*) and 24*e* (*x*, *y*, *z*). The initial coordinate of the phase II with the space group *Fd*-3*m* were as follows: Fe and Li at the octahedral sites, 16*c* (0.0, 0.0, 0.0), 16*d* (0.5, 0.5, 0.5); and O at 32*e* (*x*, *x*, *x*). Refinement results are summarized in Table 6.2. Figure 6.2 illustrates the profile fit and difference patterns of the X-ray and neutron Rietveld analysis analyzed with the two-phase structure model. The refinement results indicated an existence of about 12% of disorder rock-salt phase.

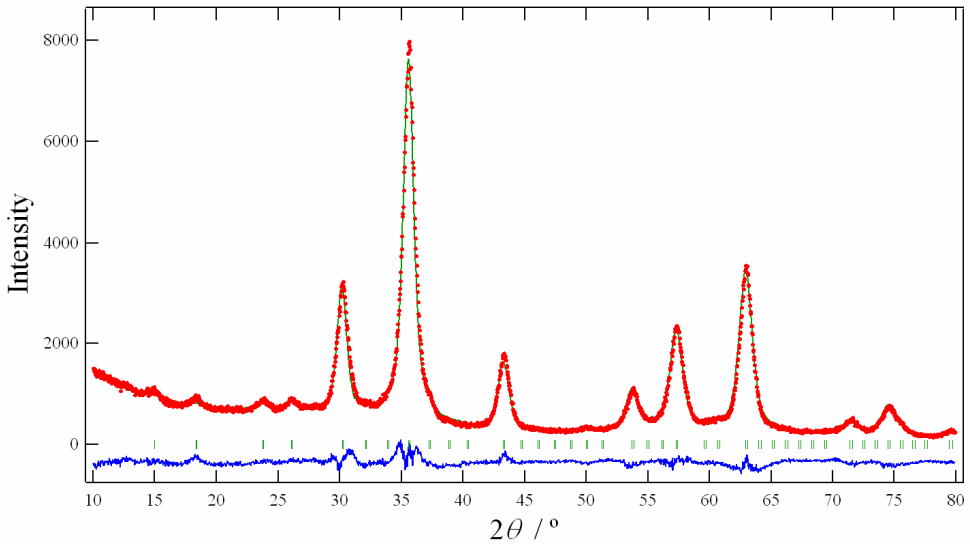

Fig. 6.1 Observed, calculated and difference plots for the nano-sized γ-Fe_2O_3, observed by (a) X-ray powder diffraction. The solid lines are calculated intensities, dots (●) overlying them indicates observed intensities, and solid line at the bottom is the difference between observed and calculated intensities.

Table 6.1 Rietveld refinement result of nano-sized γ-Fe_2O_3, before lithiation process

Atom	site	*g*	*x*	*y*	*z*	U_{iso}
Fe	4*b*	0.494(8)	0.625	0.625	0.625	0.0038
Fe	8*c*	0.941(6)	-0.0075	-0.0075	-0.0075	0.0038
Fe	12*d*	0.845(7)	0.125	0.3652	0.8848	0.0038
O	8*c*	1.0	0.3824	0.3824	0.3824	0.013
O	24*e*	1.0	0.3820	0.8640	0.8704	0.013

Space group: $P4_332$, a = 8.3443(2) Å

R_{wp} (fitted) = 6.94%, R_p (fitted) = 5.28%, R_{wp} (-B knd) = 6.64%, R_p (-B knd) = 5.35 %, D_{Wd} = 0.765

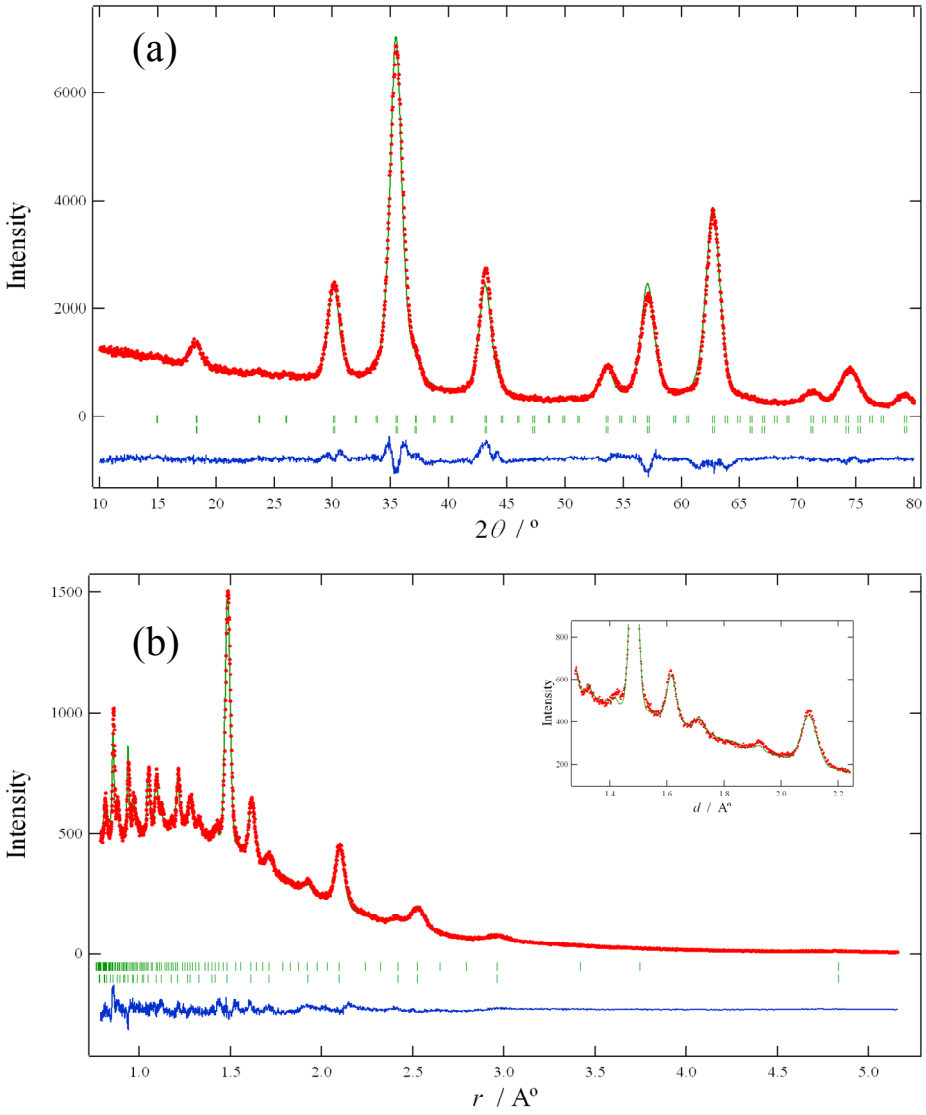

Fig. 6.2 Observed, calculated and difference plots for the litiated nano-sized γ-Fe_2O_3, observed by (a) X-ray powder diffraction and (b) neutron powder diffraction calculated with two phase. The solid lines are calculated intensities, dots (●) overlying them indicates observed intensities, and solid line at the bottom is the difference between observed and calculated intensities.

Table 6.2 Rietveld refinement result of lithiated nano-sized γ-Fe_2O_3 with two phase refinement.

Phase	Atom	site	*g*	*x*	*y*	*z*	U_{iso}
I	Fe	4*a*	0.086(6)	0.125	0.125	0.125	0.0038
	Fe	4*b*	0.683(11)	0.625	0.625	0.625	0.0038
	Fe	8*c*	0.751(3)	-0.0074	-0.0074	-0.0074	0.0038
	Fe	12*d*	0.744(6)	0.125	0.3797	0.8703	0.0038
	Li	12*d*	0.256(6)	0.125	0.3797	0.8703	0.0038
	O	8*c*	1.0	0.3779	0.3779	0.3779	0.013
	O	24*e*	1.0	0.3864	0.8804	0.8696	0.013
II	Fe	16*c*	0.0	0.0	0.0	0.0	0.0038
	Li	16*c*	1	0.0	0.0	0.0	0.0038
	Fe	16*d*	0.911(19)	0.5	0.5	0.5	0.0038
	Li	16*d*	0.089(19)	0.5	0.5	0.5	0.0038
	O	32*e*	1.0	0.2481	0.2481	0.2481	0.013

Space group: Phase I: $P4_332$, a = 8.3731(2) Å、 Phase II: *Fd-3m*, a = 8.3744(4)

Neutron; Phase I:Phase II = 0.884:0.116

*R*wp (fitted) = 3.89%, *R*p (fitted) = 2.96%, *R*wp (-B knd) = 3.72%, *R*p (-B knd) = 2.89 %, *D*Wd = 0.686

X-ray; Phase I:Phase II = 0.879:0.121

*R*wp (fitted) = 6.22%, *R*p (fitted) = 4.79%, *R*wp (-B knd) = 6.67%, *R*p (-B knd) = 5.25 %, *D*Wd = 0.531

Total

*R*wp (fitted) = 4.78%, *R*p (fitted) = 3.54%, *R*wp (-B knd) = 6.17%, *R*p (-B knd) = 4.35 %, *D*Wd = 0.601

After lithiation sample, shoulder-like reflection was observed at 2θ = 38º. Relative intensity of 2θ = 43º was higher than the sample before chemical lithiation. Occupation parameters of the tetrahedral site, 8*c* in phase I decreased from 0.941 to 0.751 and the parameters at octahedral sits, 4*a* and 4*b* increased form 0.0 to 0.806 and from 0.494 to 0.683, respectively, and the parameters at octahedral sits, 12*d* decreased from 0.845 to 0.744 with the Li disorder. Changes of the occupation parameters with the lithiation indicate a diffusion of iron from the tetrahedral site to the octahedral sites, which corresponding to a partial transformation from the defect spinel phase to the disordered rock-salt phase. Changes of X-ray diffraction patterns may due to this phase transformation. This change of site occupancy investigates that phase I is early in the state of the spinel/rock-salt phase transformation. In contrast, spinel/rock-salt phase transformation was completely progressed at phase II. Lattice parameter of phase II is closed to that of phase I. γ-Fe_2O_3, indicate low lithium ion conductivity because transition metal ions are located at tetrahedral site. Phase II may generated surface of the particles, because of this structural fault.

As in the proportion of phase I : phase II is 0.88 : 0.12, formula ratio of nanoparticle calculated from the Rietveld refinement is Li/Fe = 0.21 ($0.42Li/Fe_2O_3$, Li/Fe = 0.17 for phase I and Li/Fe = 1.20 for phase II). While the ICP measurement indicates Li/Fe = 0.31 ($0.62Li/Fe_2O_3$,). Difference in the compositions between the structure and chemical analysis indicates a possibility of another reaction except for the lithium insertion into the particles, such as adsorption reaction or reaction with residual impurity phases.

6-3 Investigation for local structure with PDF

Pair distribution function, PDF of nano-sized γ-Fe_2O_3 before and after lithiation was calculated by neutron total scattering measurements to investigate the local structure of particle surface. In the PDF calculated from neutron scattering, sign of the peaks are dependent on the scattering length of atoms. Table 6.3 summarizes the scattering length and sign of correlations for the atoms containing in the lithiated γ-Fe_2O_3, including the impurity phase[7]. Figure 6.3 shows the PDF of γ-Fe_2O_3 before and after chemical lithiation. Table 6.4 summarizes the adscription of peaks for the PDF. After the chemical lithiation, relative intensities ratio of 2 Å, 3.5 Å compare to 3 Å were decreased. New negative peaks were observed around 2.36 Å and 3.9 Å. Positive intensity at 2 Å indicates the correlation between the iron atom and oxygen atom. Decrease in this peak intensity may be due to the Li-O correlation by the lithium atoms located at the octahedral sites. Positive intensity at 3.5 Å indicates the correlation between the iron atoms located at octahedral sites and tetrahedral sites. Decrease in these peak intensity may be due to two reasons; increase in the correlation between the iron atom located at tetrahedral site and lithium atom located at the octahedral sites, and decrease in the site occupancy of iron atoms located at tetrahedral sites. These results are in good agreement with the Rietveld refinement results, which indicated the lithium located at the octahedral site and the decrease of iron at tetrahedral site.

Table 6.3 Scattering length for neutron and sign of correlations between the twp atoms

Atoms	Scatterin lemgth	Atoms				
	b_c / fm	H	Li	C	O	Fe
H	-3.74	+	+	−	−	−
Li	-1.9	+	+	−	−	−
C	6.65	−	−	+	+	+
O	5.80	−	−	+	+	+
Fe	9.45	−	−	+	+	+

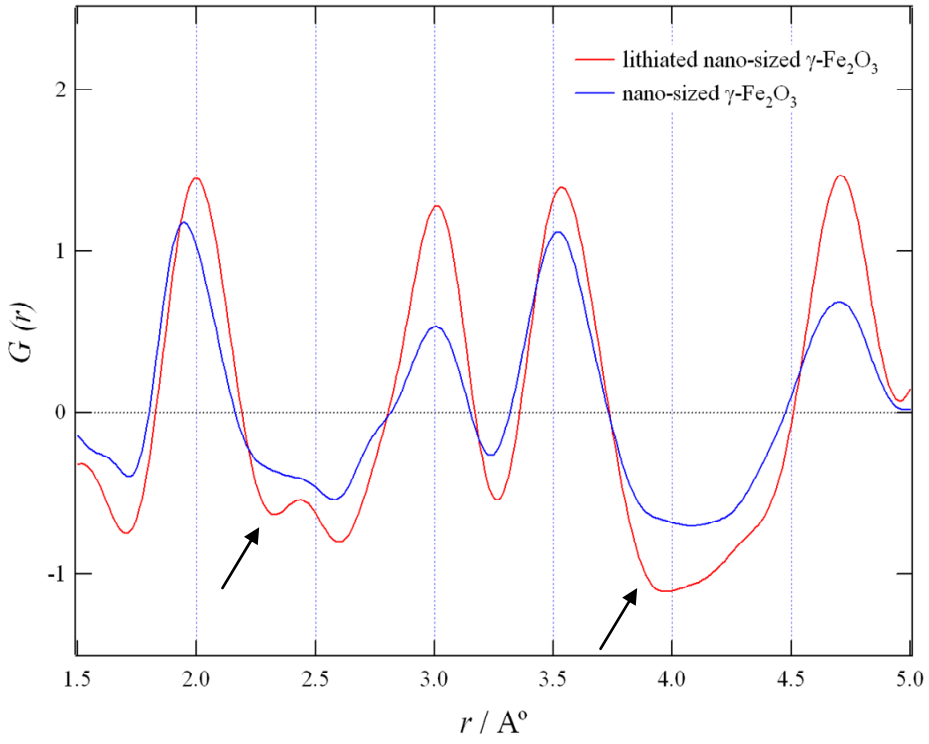

Fig. 6.3 Pair distribution functions of nano-sized γ-Fe_2O_3 before and after lithiation process calculated from neutron total scattering measurement. Arrows indicates new peaks observed after the lithiation process.

Table 6.4 Atomic relation for neutron total scattering of lithiated nano-sized γ-Fe_2O_3

r /Å	nano-sized γ-Fe_2O_3	lithiated nano-sized γ-Fe_2O_3
2.0	Fe-O	Fe-O
2.3	-	O(s)-Li(ad)
2.6	Fe(s)-H	Fe(s)-H
3.0	Fe(o)-Fe(o), O-O	Fe(o)-Fe(o), O-O
3.5	Fe(t)-Fe(o), Fe-O: 2nd	Fe(t)-Fe(o), Fe-O: 2nd, Fe(t)-Li(o)
3.9	-	O-Li(ad): 2nd, Fe-Li(ad)
4.7	Fe-O: 3rd	Fe-O: 3rd

Labels: (s), surface; (ad): adsorption, (o): octahedral site, *n*th: *n*th neighboring correlation

Negative peak at 2.36 Å obtained after chemical lithiation may be attributed to the correlation between the lithium atom and oxygen atom. However, the distance of this correlation is longer than the conventional ionic bonding between oxygen and lithium (*ca.* 2.0 Å, such as LiOH)[8] or correlation between the lithium atoms and oxygen atoms which located at intercrystalline sites (*ca.* 2.0 – 2.1 Å). There are two possibilities for this long distance correlation. One is the correlation of the longer bonding with the physical adsorption or coordination linkage, on the particle surface. Another is the distortion inner particle. It cannot be determined that this negative peak was originated by which type of lithium. Negative peaks at 3.9 Å may indicate the correlation of the iron atom and adsorbed lithium or lithium at distorted site. These results indicate an existence of lithium loosely bonded in the lithiated samples, probably those lithium adsorbed on the particle surface. Assuming that residual impurity phase did not provide any side reaction, 0.1Li per iron ($0.2Li/Fe_2O_3$) were adsorbed (or reacted) on the particle surface.

6-4 Investigation for the reaction process of nano-sized γ-Fe_2O_3 with lithium

X-ray and neutron powder diffraction measurements indicate that the lithiation process was proceeded with a two-phase reaction. The PDF, calculated from the neutron total scattering measurement, indicated the existence of surface lithium. These results indicate the existence of three types of lithium, contained at defect spinel phase (phase I), contained at disordered rock-salt phase (phase II), and adsorbed at particle surface.

Figure 6.4 shows the XRD patterns of nano-sized γ-Fe_2O_3 with the Li/Fe ratio, Li/Fe = 0.31, those of the lithiated γ-Fe_2O_3 by chemically and electrochemically. The lithiated samples showed peak shifts with a small shoulder-like peak around 2θ = 37º and the increase of peak intensity of 2θ = 43º. No significant change was observed for the chemically and electrochemically lithiated samples. Both processes proceeded in a similar manner.

Lattice parameters of chemically lithiated sample (phase I) and electrochemically lithiated samples (calculated as a cubic type cell) are 8.3729(2) Å and 8.3692(7) Å, respectively. Chemical lithiated sample indicates a slightly large value. This might be depends on the lithiation process for these two methods: cell voltage at the 0.31Li is indicate about 1.5 V (Fig. 6.5), while chemical potential of *n*-BuLi *vs.* Li/Li^+ is about 1.0 V.

Figure 6.6 shows the *ex-situ* XRD measurement of first discharge process down to 1.0 V vs. Li/Li^+ and after charged from 1.0 to 4.0 V Li/Li^+. Lattice parameters of defect spinel phase (phase I mentioned in above sections) were also shown in Fig. 6.6. Lattice parameters of defect spinel phase changed linearly with the lithium content. The X-ray powder diffraction, neutron powder diffraction and neutron total scattering measurements indicate that there are three types of lithium, (i) lithium at defect spinel phase (phase I), (ii) lithium, at disordered rock-salt phase (phase II), and (iii) lithium adsorbed at particle surface, at the middle of the discharge process around 1.5 V. Lithiation insertion, adsorption and phase transformation reactions may be proceeded simultaneously to the 1.2 V.

Discharge reaction below the 1.2V, profile of lattice parameters for defect spinel phase was saturated and disorder rock-salt phase was clearly increased. In this range, too much lithium was inserted into the particles and phase transformation was rapidly progressed.

After discharged process down to 1 V vs. Li/Li^+ and charged up to 4 V vs. Li/Li^+. After the charge process, the amount of the disordered rock-salt phase was decreased and back to the spinel phase again. Kato *et al.* reported similar reaction for the nano-sized Fe_3O_4 with spinel type structure[9]. For Fe_3O_4, crystalline phase was changed to amorphous phase during the discharge process. At the next charge process, remaining Fe_3O_4 phase act as a core, and the amorphous phase transformed to the Fe_3O_4 spinel phase. For the nano-sized γ-Fe_2O_3, defect spinel phase, phase I, might act as a core, and the disordered rock-salt phase transformed reversibly to the defect spinel structure during the charge process. After the discharge process, lattice parameter of phase I was

decreased from 8.387(5) Å to 8.368(3) Å. Lithium was extracted from phase I. In the charge process, lithium extraction from phase I and phase transformation from phase II to phase I proceeded simultaneously.

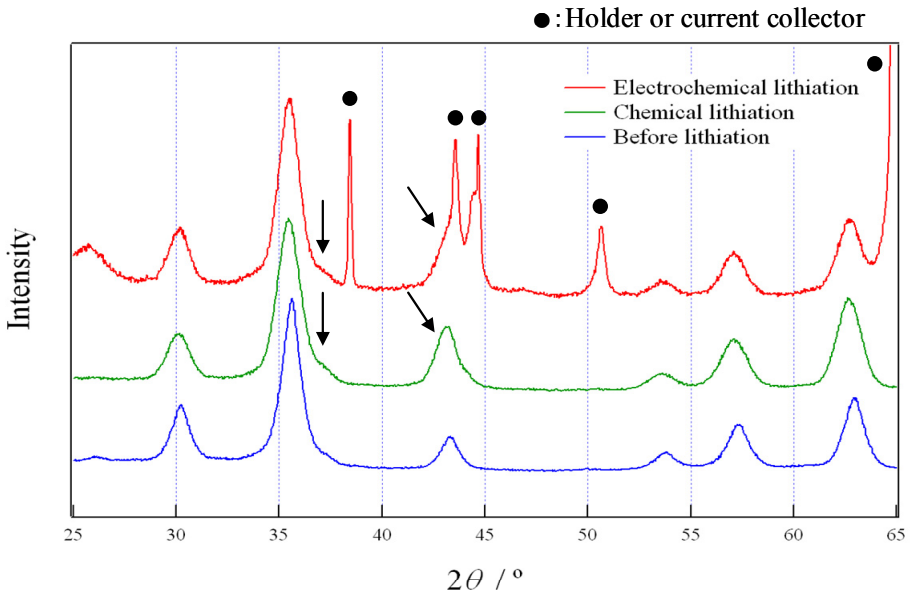

Fig. 6.4 Comparison of the XRD patterns for nano-sized γ-Fe_2O_3, before lithiation (blue line), after chemical lithiation (green line) and after electrochemical lithiation process (red line). Arrows indicate the reflections which changed.

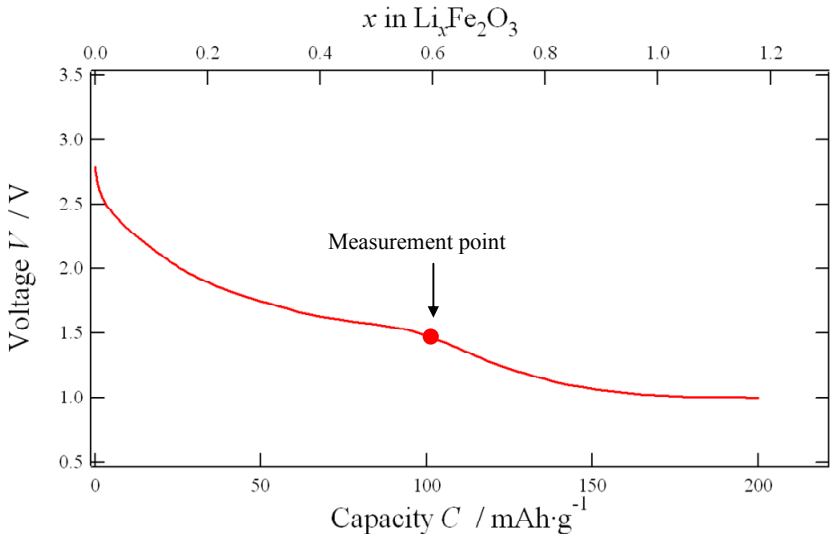

Fig. 6.5 First discharge curve of nano-sized γ-Fe_2O_3. Circle indicates the composition of the sample appeared for the chemical lithiation sample.

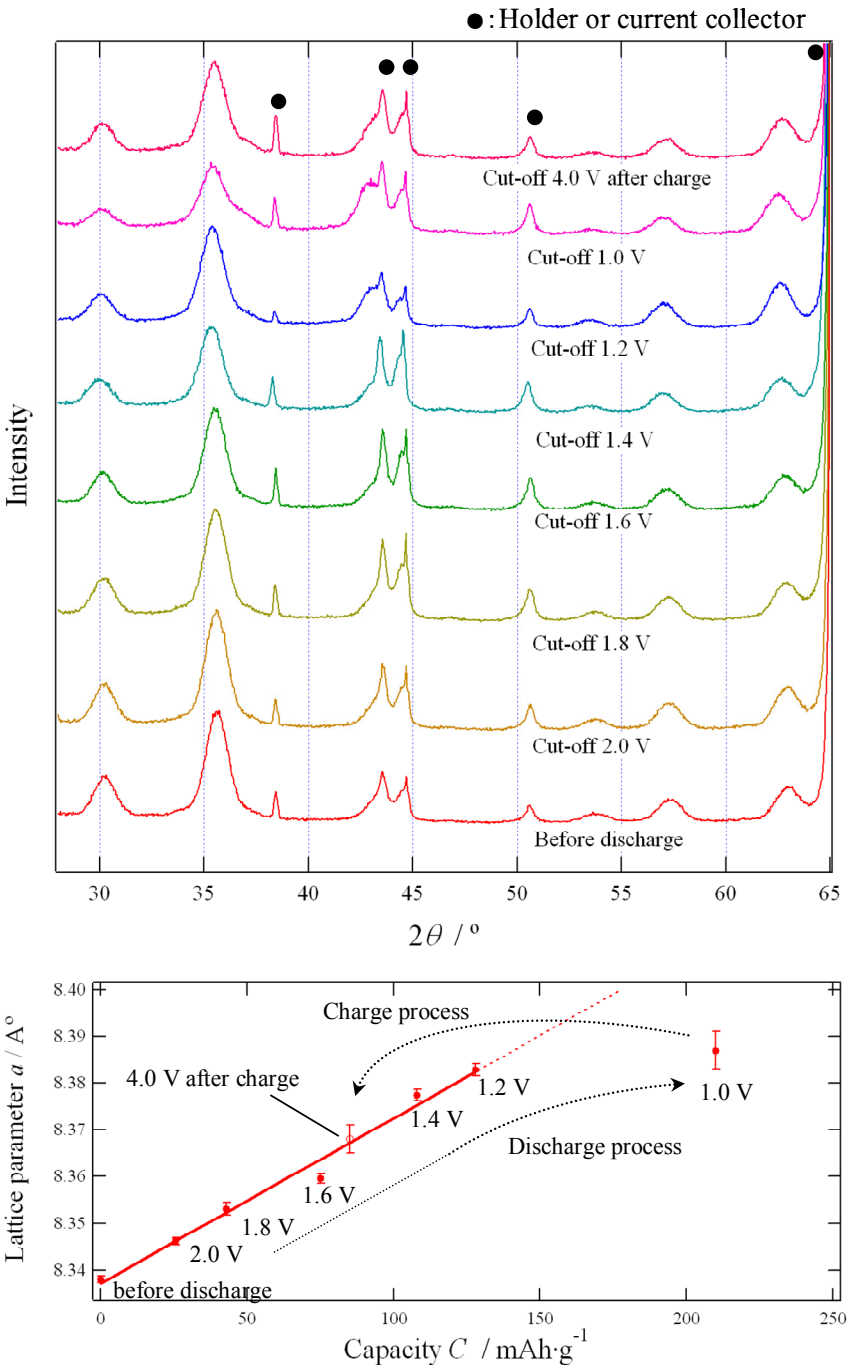

Fig. 6.6 (a) e*x-situ* X-ray diffraction patterns of nano-sized γ-Fe_2O_3 measured during the first discharge process and (b) variation of the cubic lattice parameter for the phase I during the first discharge process.

6-6 Conclusion

Reaction mechanism of nano-sized γ-Fe_2O_3 with lithium was investigated. Rietveld analysis of X-ray powder diffraction and neutron powder diffraction measurements indicate lithium rich disorder rock-salt phase was formed, and it is ascertained that this reaction was undergone two-phase reaction with defect spinel phase and disorder rock-salt phase. Pair distribution functions calculated from neutron total scattering measurement result indicate lithium ions are adsorbed on the particle surface. Biphasic reaction and adsorption reaction are typical of the ultra fine nanoparticle, and reversible reaction was provided from these reactivates

Reference

1. M. Pernet, P. Strobel, B. Bonnet, P. Bordet and Y. Chabre, *Solid State Ionics*, **66**, 259 (1993).
2. S. Komaba, K. Suzuki and N. Kumagai, *Electrochemistry (Tokyo, Japan)*, **70**, 506 (2002).
3. S. Kanzaki, T. Inada, T. Matsumura, N. Sonoyama, A. Yamada, M. Takano and R. Kanno, *J. Power Sources*, **146**, 323 (2005).
4. D. W. Murphy and P. A. Christian, *Science (Washington, DC, United States)*, **205**, 654 (1979).
5. M. Ohashi, S. Yamanaka, M. Sumihara and M. Hattori, *J. Inclusion Phenom*., **2**, 289 (1984)
6. H.-S. Shin, *Yoop Hakhoechi*, **35**, 1113 (1998).
7. V. F. Sears, *Neutron News*, **3**, 3 (1992)
8. S. L. Mair, *Acta Crystallogr., Sect. A: Found. Crystallogr.*, **A34**, 542 (1978).
9. T Kato, K. Nakazawa, K. Fujimoto, S. Ito, *Proceedings of The 47th Battery Symposium in Japan*, (Nov., 20-22, Tokyo, 2006) No. 3F-20

Chapter 7

Composite electrode of iron oxide nano-particles in CMK-3 mesoporous carbon matrix for lithium battery

7-1 Introduction

Mesoporous carbons are previously used as an anode materials for lithium secondary battery[1-3]. In this chapter, composite electrode of iron oxide with nano-metric structure and mesoporous carbon is investigated. Schematic drawing of the composite electrode of iron oxide on the mesoporous carbon structure is shown in Fig. 7.1. The electrolysis was used for the synthesis of composite system. During the electrolysis, irons are deposited on the surface of the mesopore of the mesoporous carbon, and oxidized in the mesopore.

The advantageous of the systems are as follows: (i) large surface area improves close contact between electrode and electrolyte, which allows high electrochemical reaction at the electrode/electrolyte interface and high current densities as a result, (ii) small particle size of simple oxides caused different reaction mechanism from those of bulk materials, for example, reversible spinel/rock-salt phase transition was observed during the charge-discharge reactions for γ-Fe_2O_3, which provided high reversible capacities, (iii) large surface area might provide surface reactions similar to a reaction mechanism of super-capacitor, which may provide high capacity together with the intercalation reaction mechanism.

In this chapter, the new composite electrode of mesoporous carbon and iron oxide was investigated. The composite system showed high lithium storage capacity with high rate capability. The composite electrode was synthesized using electroplating in an aqueous solution to insert iron into the mesopore of the carbon matrix. The synthesis, characterization, and charge-discharge property were studied and its reaction mechanism will be discussed.

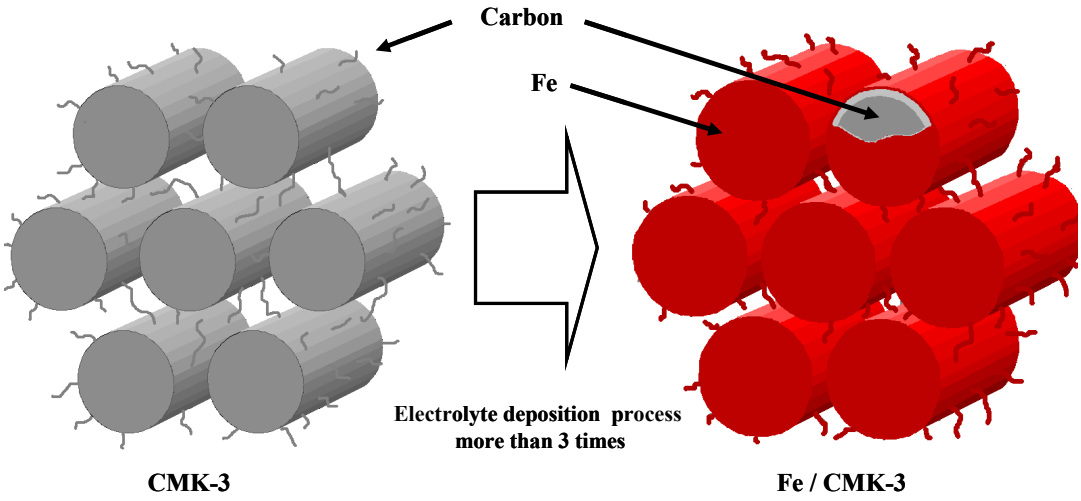

Fig. 7.1 Schematic drawing of the composite electrode of iron oxide on the mesoporous carbon structure.

7-2 Characterizations

Figure 7.2 shows the N_2 adsorption isotherms and pore distribution of mesoporous carbon (CMK-3) and the samples prepared by electrolysis process for 1 time, 3 times, and 5 times. Figure 7.3 shows the X-ray diffraction patterns of the mesoporous carbon (CMK-3) and the sample prepared by the electrolysis for 3 times. The N_2 adsorption isotherm curves indicated that the surface area decreased with the electrolysis process, indicating that the iron was cast on the carbon surface. The changes in the slope due to mesopore ($P / P_0 < 0.5$) became small with the electrolysis process, while no significant changes were observed in the curves at $P / P_0 < 0.1$. The pore distribution function shown in Fig. 7.2(b) indicated that the pore with a diameter of around 3 ~ 4 nm for the mesoporous carbon disappeared for the electrolysis samples. These results indicate that the pore in the mesoporous carbon decreased to around 1nm by the electrolysis process. Low-angle X-ray diffraction pattern of the electrolysis sample indicated that a peak due to periodic distribution of mesopore became small, consistent with a decrease in the mesopore in the structure. Table 7.1 summarizes BET surface area, pore volume, $d(100)$, pore size and wall thickness of mesoporous carbon (CMK-3), and the mesoporous carbon/iron oxide composites. Mössbauerspectra of mesoporous carbon/iron oxide composite after electrolysis process indicated the values of isomer shift, $IS = 0.27$ mm/s, and quadrupole splitting, $QS = 0.95$ mm/s, consistent with the Fe^{3+} state. The iron plated on the CMK-3 was oxidized in air and became Fe^{3+} state. The spectra indicated disappearance of internal magnetic field, suggesting super-paramagnetism due to nano particle effect. The X-ray diffraction pattern at high angle region indicated amorphous character. The iron content in the final product was determined by chemical analysis using ICP, for example 3 times electroplating process provided an iron content of about 30 wt% of total sample weight. The composite materials of mesoporous carbon and iron oxide were successfully synthesized in the present study. The structure of the mesoporous carbon / iron oxide composite electrode is shown in Fig. 7.1. The iron oxides were deposited on the mesopore of the carbon matrix while the composite

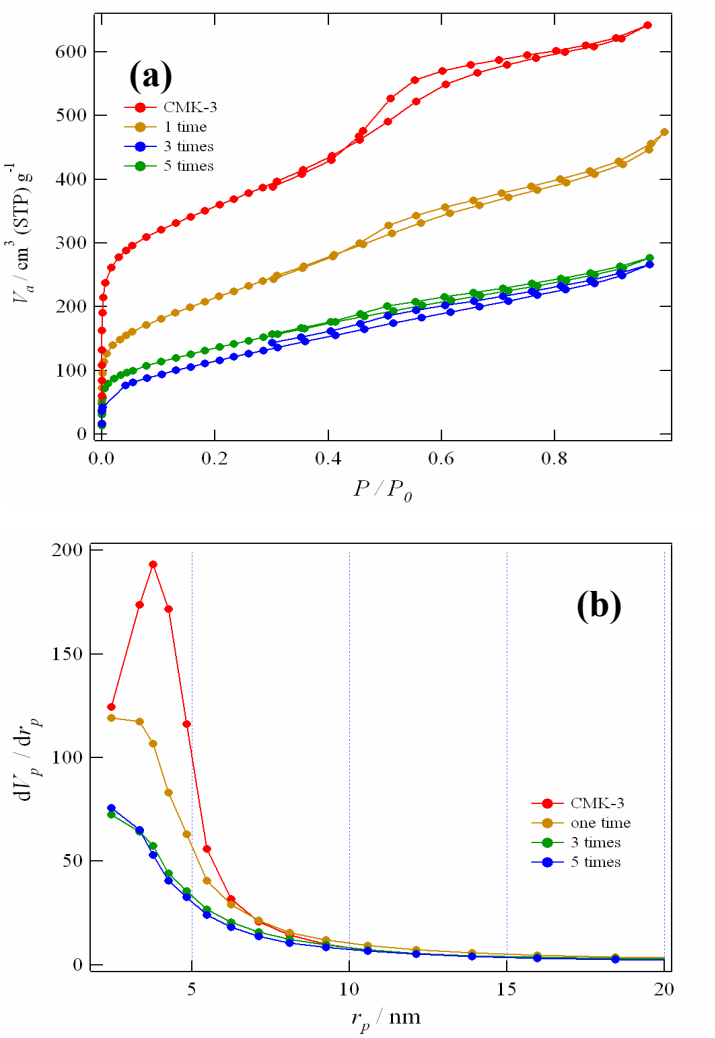

Fig. 7.2 (a) N_2 adsorption isotherms and pore distribution (b) of mesoporous carbon(CMK-3) and the samples prepared by electrolysis process : CMK-3, electrolysis of 1 time, 3 times, and 5 times.

Table 7.1 BET surface area, pore volume, *d*(100), pore size and wall thickness of mesoporous carbon and iron oxide composite.

Sample	BET surface area	Pore volume	*d*(100)	Pore size	Wall thikness
	s / m^2 g^{-1}	v / m^3 g^{-1}	l / nm	l / nm	l / nm
CMK-3	1077	0.99	9.0	3.7	6.7
Composite (1 time)	727	0.73	-	3.0	-
Composite (3 times)	406	0.41	9.0	2.4	4.3
Composite (5 times)	452	0.43	-	2.0	-

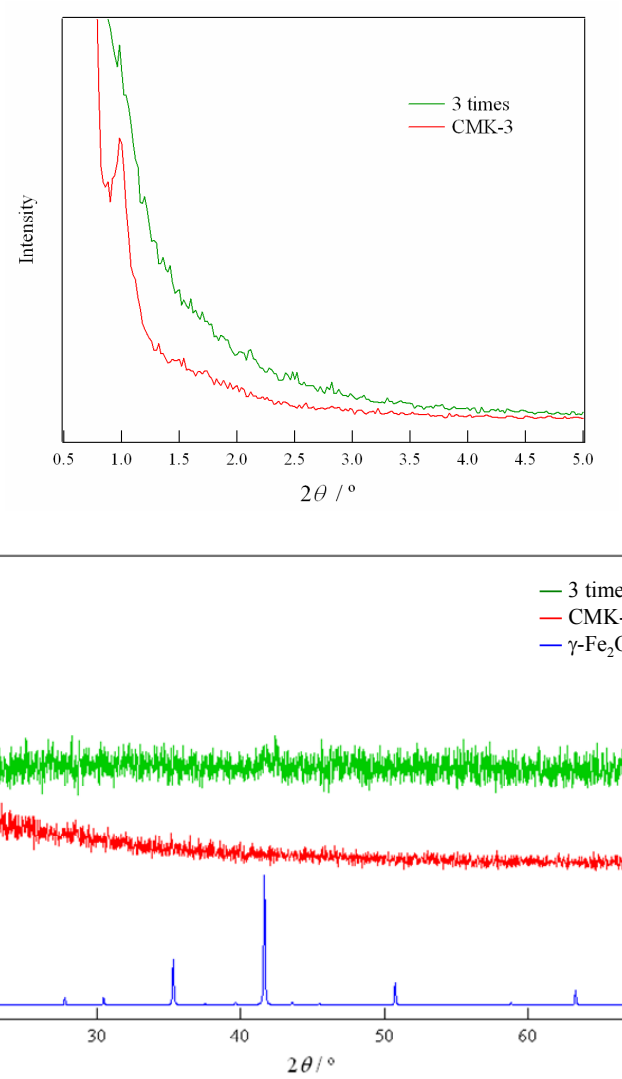

Fig. 7.3 X-ray diffraction patterns (top: low angle, bottom: $2\theta = 20° - 70°$) of the mesoporous carbon(CMK-3) and the samples prepared by electrolysis process for 3 times.

structure still has pores of around 1 nm. The iron after deposited by electroplating changed to an amorphous state of iron oxides. These samples were then heated at 250°C in O_2. The X-ray diffraction patterns of the heat-treated samples indicated several diffraction peaks which are indicative of γ-Fe_2O_3. However, due to weak peak intensities, the phase was not determined. Figure 7.4 shows the SEM images and EDX analysis of the mesoporous carbon (CMK-3) and the mesoporous carbon/iron oxide composite after three times electrolysis. The surface of the carbon matrix was covered by small particles. The EDX images indicated homogeneous distribution of iron on the surface. The SEM observation of the samples after treated at 250°C in O_2 indicated particles with diameter of 2 ~ 3 nm with a length of 10 nm on the surface of carbon matrix. No segregation of the nano-particles was observed by the heat-treatment process.

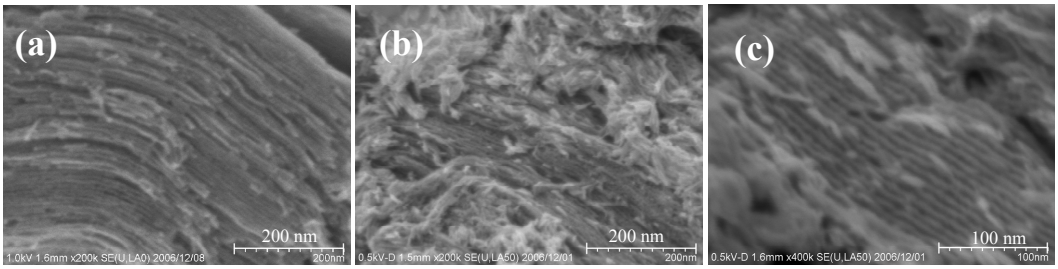

Sample	Low magnetization		High magnetization	
	SEM	EDX	SEM	EDX
CMK-3				
CMK-3 / iron oxide composite				

Fig. 7.4 SEM(top) and SEM-EDX(bottom) images of mesoporous carbon(CMK-3) and CMK-3 / iron oxide composite. Top: (a) is the CMK-3 before electrolysis process, (b) is the composite sample before heat treatment, (c) is the composite sample after heat treatment. Iron distribution was mapped for the EDX image.

7-3 Electrochemical behavior with lithium

Figure 7.5 shows the cyclic voltammogram (CV) of the mesoporous carbon/iron oxide composite electrode. Broad oxidation peak around 2.3 V and a reduction peak around 1.5 V were observed, which are consistent with the redox couple of Fe(III)/Fe(II). The CV behavior is similar to those reported previously for γ-Fe_2O_3 with nano particle-size, but is completely different from those of CMK-3. These results indicate that the electrochemical characteristics of the sample synthesized in the present study are due to iron oxides. Figure 7.6 shows the charge-discharge curves of the composite electrode with a current density of 0.5 mA/cm^2 and cut off voltages of 1.0 and 4.0 V. The mesoporous carbon/iron oxide composite electrode showed much higher capacity than γ-Fe_2O_3 nano-particles of 230 mAh/g[4]. The capacity was calculated both for the mesoporous carbon/iron oxide composite sample and iron oxide, Fe_2O_3. As the CV experiments indicated that only the iron oxide participates in the electrochemical reactions, the capacity value based on Fe_2O_3 might be suitable. It is surprising that the first discharge capacity exceeded 1100 mAh/g, which is extremely higher than the theoretical values of 340 and 170 mAh/g for the electrode reactions (1) and (2), respectively.

$$Fe_2O_3 + 2Li \rightarrow Li_2Fe_2O_3 \qquad (1)$$

$$Fe_2O_3 + Li \rightarrow LiFe_2O_3 \qquad (2)$$

The capacity obtained is almost comparable to the theoretical value of 1020 mAh/g for the reaction as follows.

$$Fe_2O_3 + 6Li \rightarrow 3Li_2O + 2Fe \qquad (3)$$

Recently, Ito *et al.* indicated large capacity of iron oxide for higher temperature operation; they also indicated a capacity which exceeds 1000 mAh/g for iron oxides[5]. They proposed the reaction mechanism that the iron reduced to metallic state. However, the cell voltages exceed 1.0 V, this might not be provided by a redox couple of Fe(0)/Fe(II). The charge-discharge capacities obtained for the mesoporous carbon/iron oxide composite cathode indicated huge reversible charge-discharge

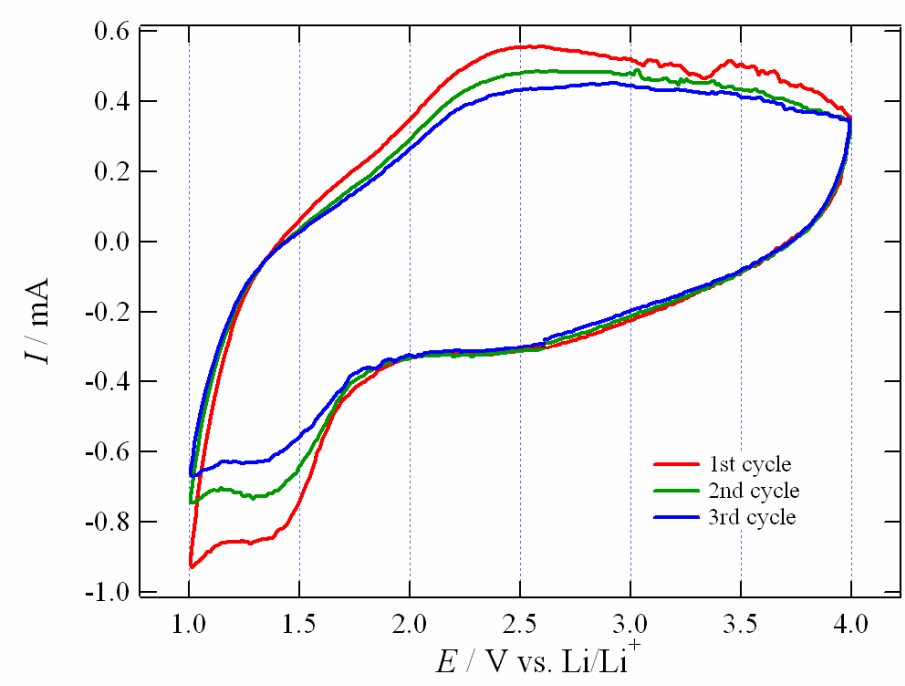

Fig. 7.5 Cyclic voltamogram of meso-porous carbon/iron oxide composite. Scan rate: 0.1 mmV/sec.

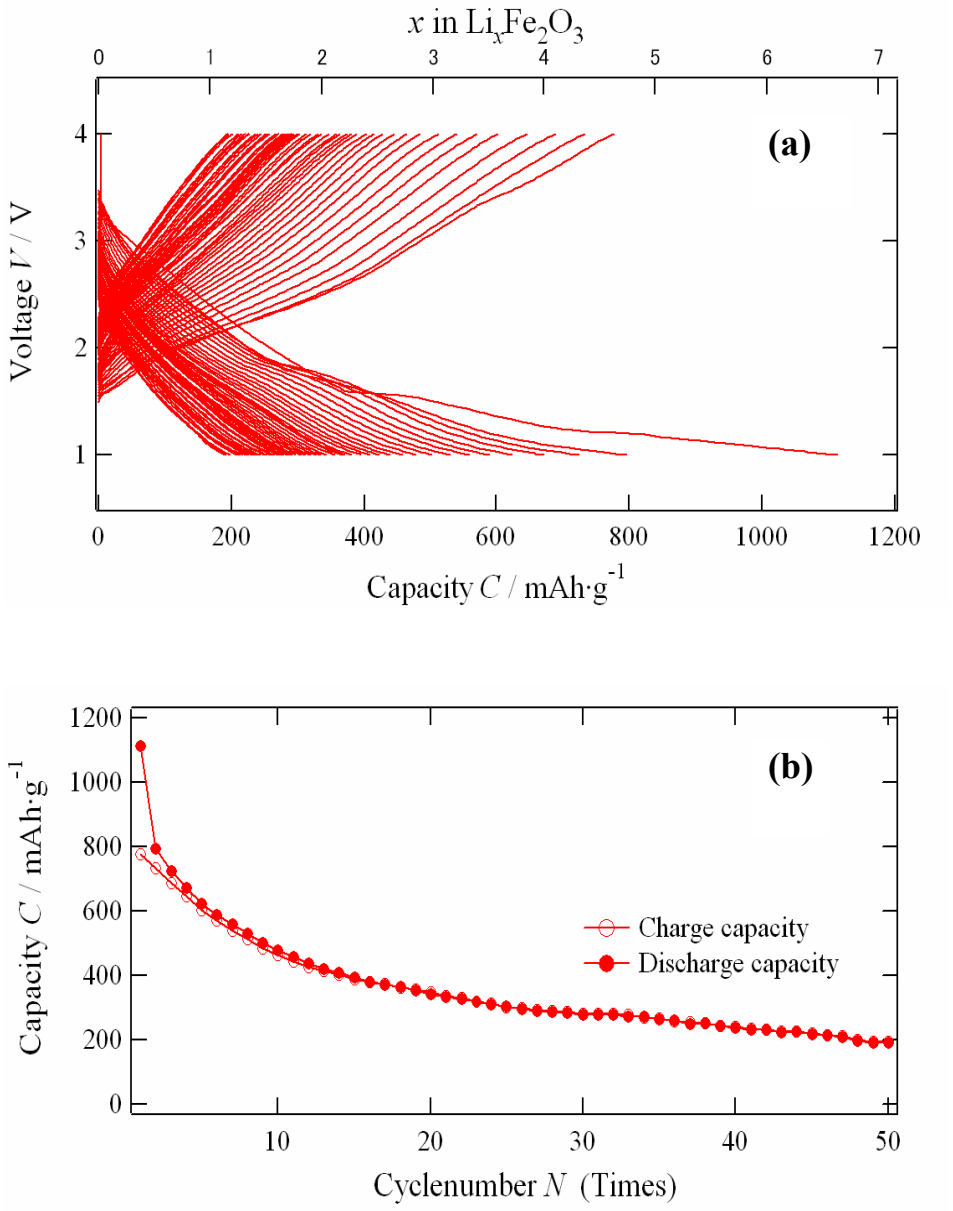

Fig. 7.6 (a) Charge-discharge curves for meso-porous carbon/iron oxide composite. Conditions: cut-off voltage: 1.0 V and 4.0 V; current density: 0.5 mA/cm^2. (b) Cyclenumber dependence of charge/discharge capacities of mesoporous carbon / iron oxide composite.

capacities. The Mössbauer spectra of the discharged sample indicated a mixed-valent state of Fe(II)/Fe(III). The refined parameters are summarized in Table 7.2. Assuming that the redox couple of Fe(II)/Fe(III) participates in all the charge-discharge reaction, the capacity calculated from the Mössbauer data was 84 mA h/g, which is much smaller than those observed for our experiments. The discrepancy between the charge-discharge capacity and valence state obtained by the Mössbauer spectroscopy was previously indicated for $LiFeO_2$ with the $LiMnO_2$-type and the holandite structure [6, 7], and layered lithium manganese iron oxide[8, 9]. The valence change in oxygen was proposed for these systems. However, further studies on the charge-discharge mechanism are necessary to understand the huge capacity obtained for the iron oxide system.

Table 7.2 Fitting parameters mesoporous carbon/iron oxide of Mössbauer spectra of composite before and after the electrochemical discharge experiments.

	Species	Quotient	*IS*	*QS*
Before discharge	Fe(III)	100	0.271	0.955
After discharge	Fe(II)	25.7	0.741	1.770
	Fe(II)	74.3	0.326	0.671

Charge-discharge characteristics were also observed for the mesoporous carbon / iron oxide composite cathode treated at 330°C in O_2 conditions. The charge-discharge capacity of 300 mAh/g was observed for the first cycle, which is lower than the sample treated at 250°C. The XRD and N_2 adsorption experiments of the sample treated at 330°C indicated the same parameters as those of 250°C. As the TG curves of the composite electrode indicates weight loss above 350°C, corresponding to the decomposition of carbon matrix, the heat treatment at 330°C caused less carbon content in the samples and consequently low charge-discharge characteristics. These results indicate that the carbon matrix plays an important role for its quite high charge-discharge characteristics.

Charge-discharge characteristics were measured as a function of current range of 0.05 - 0.5 mA/cm^2, corresponding to a C rate of 0.07 to 0.7. (Fig. 7.7) No significant degradation in charge-discharge capacities was observed between the current range between 0.05 and 0.5 mAh/g, which indicates that the composite electrode has very high power characteristics of lithium battery reaction.

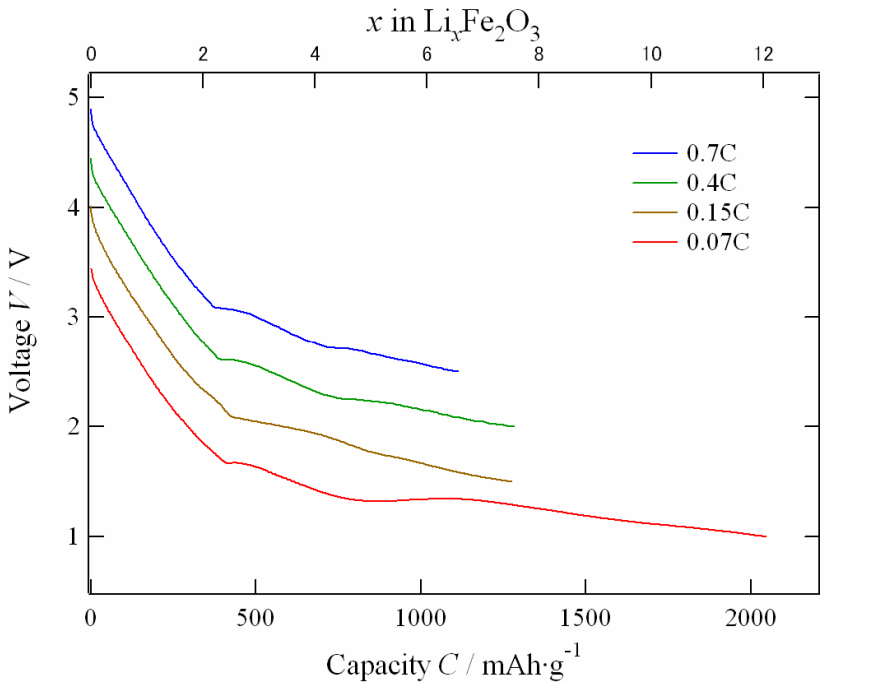

Fig. 7.7 First discharge curves with various C rate. For clarify, the data for voltage in 0.15C, 0.4C and 0.7C have been offset by 0.5, 1.0 and 1.5, respectively.

There are several criteria for the lithium battery reactions; (i) bulk intercalation reaction, (ii) reversible oxidation-reduction reaction up to metal (0 valent state), (iii) adsorption at the surface. Nano-size effect of the electrode reaction is indicated for these criteria. For the bulk intercalation reaction, nano-size effect was observed for γ-Fe_2O_3 where the reversible spinel/rock-salt phase transition that is irreversible process for bulk material was observed or nano particle[4]. Reversible process with an electrode reaction indicated in the equation [6] was previously reported for simple oxide nano-particles, such as CoO and FeO [10]. The reduction to metal caused high capacity although the potential is low and is suitable for anodes. The importance of the surface adsorption of lithium is widely recognized for super-capacitor. We also indicated the possibility of this type of reaction for α-Fe_2O_3-SnO_2 composite cathode materials[11]. The mesoporous carbon / iron oxide composite electrode showed extremely high charge-discharge capacity with high rate capability. The composite electrode showed cell voltages of the 1 V – 4 V, which is higher than those expected by the reaction of Fe(0)/Fe(II) couple. The role of the nano-particle surface might be important for the charge-discharge reactions. On the other hand, composite structure of the electrode provided a close contact between the nano-particles of iron oxide and the carbon matrix with high electronic conduction. This causes high utilization ratio of the iron oxide electrode and high rate charge-discharge reactions. The nano-particle iron oxide, γ-Fe_2O_3, showed only a charge-discharge capacity of 230 mAh/g with a current density of 0.1 mA/cm, which is much lower than the composite electrode.

7-4 Conclusion

Composite electrode of mesoporous carbon (CMK-3) and nano-particles of iron oxide was synthesized, with an electrolysis method. The mesopore of the carbon structure was almost filled up by iron oxide nano-particles, constructing a close contact between high electric conducting carbon matrix with cathode materials. The composite electrode showed extremely high charge-discharge capacity with high current rate capability, and is a promising candidate for future lithium battery cathode material.

Reference

1. B. Li, K. Li, C. Lu, D. Wu, L. Ling, C. Xu and R. a. Wang, *Shiyou Daxue Xuebao, Ziran Kexueban*, **25**, 81 (2001).
2. P. Li, C.-y. Wang, H. Jiang and J.-m. Zheng, *Tansu Jishu*, 5 (2001).
3. H. Zhou, S. Zhu, M. Hibino, I. Honma and M. Ichihara, *Adv. Mater. (Weinheim, Fed. Repub. Ger.)*, **15**, 2107 (2003).
4. S. Kanzaki, T. Inada, T. Matsumura, N. Sonoyama, A. Yamada, M. Takano and R. Kanno, *J. Power Sources*, **146**, 323 (2005).
5. S. Ito, N. Umehara, H. Takata and T. Fujii, *Solid State Ionics*, **172**, 403 (2004).
6. T. Matsumura, R. Kanno, Y. Inaba, Y. Kawamoto and M. Takano, *J. Electrochem. Soc.*, **149**, A1509 (2002).
7. T. Shirane, R. Kanno, Y. Kawamoto, Y. Takeda, M. Takano, T. Kamiyama and F. Izumi, *Solid State Ionics*, **79**, 227 (1995).
8. M. Tabuchi, A. Nakashima, K. Ado, H. Kageyama and K. Tatsumi, *Chem. Mater.*, **17**, 4668 (2005).
9. M. Tabuchi, A. Nakashima, K. Ado, H. Sakaebe, H. Kobayashi, H. Kageyama, K. Tatsumi, Y. Kobayashi, S. Seki and A. Yamanaka, *J. Power Sources*, **146**, 287 (2005).
10. P. Polzot, S. Laruelle, S. Grugeon, L. Dupont and J. M. Tarascon, *Nature (London)*, **407**, 496 (2000).
11. T. Matsumura, N. Sonoyama, R. Kanno and M. Takano, *Solid State Ionics*, **158**, 253 (2003).

Chapter 8

Summary

Iron oxides are most ideal materials for next generation lithium secondary battery cathode materials, because of its low cost and non toxicity. Iron oxides with nano-sized morphology indicate reversible electrochemical reactivity with lithium with the suppression of irreversible phase transformation. Large surface area of nanoparticles may provide high reactivity. In the present study, iron oxide ultra fine nanoparticles were investigated from a viewpoint of the reversible Li-storage properties for those materials. γ-Fe_2O_3 was chosen for this research because of its high reactivity and high sorbability. As a result, crystalline nano-sized γ-Fe_2O_3 was synthesized and purified by heat treatment in oxygen atmosphere (chapter 3). The nanoparticles indicate reversible electrochemical reactivity which was not observed large particles synthesized by conventional ceramic sintering method (chapter 4). The sample treated by chemical oxidation provided the larger capacity and better cycling characteristics (chapter 5). X-ray diffraction, neutron diffraction, and neutron total scattering measurements indicated the reaction proceeded by two-types kinds of processes, intercalation process and adsorption process (chapter 6).

New lithium secondary battery cathode system, iron oxide ultra fine nanoparticle/mesoporous carbon composite system was also investigated. Because of its high electron conductivity, huge surface area and nanometric morphology, mesoporous carbons are expected as a supporter of nano-sized iron oxide, which is an as active center of cathode. Composite system was prepared by the electrochemical plating method. As a result, the composite electrode showed extremely high charge-discharge capacity with high current rate capability, and is a promising candidate for future lithium battery cathode material (Chapter 7).

The results of each chapters are summarized as follows.

In chapter 3, synthesis method, synthesis condition and purification process of nano-sized

γ-Fe_2O_3 were investigated. Careful identification of the optimum heat treatment condition was essential to isolate nano-sized γ-Fe_2O_3 with low impurity phase. Results are summarized follows.

(i) Nano-sized γ-Fe_2O_3 was synthesized by the mild oxidation of iron-micelle.

(ii) Coarse product contains about 40 wt% organic impurity phase.

(iii) Impurity phase was successfully removed by the heat treatment in oxygen atmosphere without phase change or particle size growth.

Identification of impurity phase was tried with XRD, FT-IR, ^{1}H NMR and ^{13}C NMR measurements. The impurity phase might be oleic acid related compound, but its formula was too complicated to be determined. By the purification with the conditions of 150°C for 20h in oxygen atmosphere, impurity phase was successfully removed without any phase change nor particle size growth.

In chapter 4, electrochemical properties of nano-sized γ-Fe_2O_3 were examined. Particle size effect, cell performance and reaction process were investigated. Results are summarized follows.

(i) Irreversible spinel/rock-salt phase transformation was suppressed by the down sizing effect.

(ii) Electrochemical reaction of nano-sized γ-Fe_2O_3 with lithium was undergone by reduction of iron with other side reactions.

(iii) Electrochemical reactivity of nano-sized γ-Fe_2O_3 with lithium was reversibly, but cycle characteristic was not efficient for a practical use.

Spinel/rock-salt phase transformation, which was reported to the conventional large size particle, was suppressed for the samples particle size of less than 20 nm. Suppression of this phase transformation provided the reversible reactivity, and these particles are suitable for lithium secondary battery cathode materials. The discharge capacity, however, was not consistent with the calculated capacity, estimated by Fe(III)/Fe(II) ratio determined by the Mössbauer spectroscopy. Electrochemical reactions of nano-sized γ-Fe_2O_3 with lithium might proceeded by reduction of iron

with other side reactions, such as lithium adsorption on the particle surface.

In chapter 5, effect of chemical oxidation was investigated. Chemical oxidation process was performed with NO_2BF_4 / acetonitrile solution in argon atmosphere. Influence of the chemical oxidation for the structure, morphology and electrochemical properties are examined. Results are summarized follows.

(i) Particle structure, morphology and size were not affected by the chemical oxidation process.

(i) Chemical oxidation was efficient to remove the impurity phase on the surface of nano-size γ-Fe_2O_3 particles.

(ii) Charge and discharge capacities and cycling characteristics are improved by the treatment of chemical oxidation.

XRD measurement and SEM observation indicated that the chemical oxidation made no changes in the structure, morphology and particle size. TG and FT-IR measurements indicated that 3 wt% of impurity phase was removed by the chemical oxidation, while the process was not efficient to remove protons which were adsorbed or chemically bonded on the surface. The sample after chemical oxidation showed larger charge-discharge capacity with better cycling characteristics. The increase in the amount of lithium intercalated into the structure caused the spinel/rock-salt phase transformation. However, this phase transformation was reversible and this indicates further possibility to improve reversible capacities of the nano-particles.

In chapter 6, details of the reaction process for nano-sized γ-Fe_2O_3 with lithium was investigated by the neutron diffraction and neutron scattering techniques. Samples for the neutron diffraction and neutron scattering are prepared by chemical lithiation with *n*-BuLi in hexane solution. XRD measurement indicated that the structure of chemically lithiated γ-Fe_2O_3 and electrochemically lithiated γ-Fe_2O_3 were almost the same. Results are summarized follows.

(i) Intercalation proceeded by the two-phase reaction.

(ii) Reaction of nano-sized γ-Fe_2O_3 with lithium proceeded by the intercalation and the adsorption reactions, simultaneously.

Two-types of phases, defect spinel and disordered rock-salt phase, were indicated by the neutron diffraction measurement. The intercalation proceeded with a biphasic reaction. Pair distribution functions calculated from the neutron total scattering measurement indicated the correlation of Li-O with a distance of 2.36 Å. This distance is longer than the distance of ionic bonding, such as LiOH (*ca.* 2.0 Å), or distance of tetrahedral site/octahedral site in the crystal structure (*ca.* 1.8 Å - 2.0 Å). This long distance may indicate that lithium coordinates to the oxygen on the particle surface, by the reaction mechanism of lithium adsorption. Lithiation of nano-sized γ-Fe_2O_3 proceeded by reactions of intercalation and adsorption.

In chapter 7, new type of cathode, iron oxide nanoparticle/mesoporous carbon binary system was investigated. Iron oxide/mesoporous carbon binary system was prepared by the electrolytic plating process. CMK-3 was used as a supporting matrix of the electrolysis. Structures and electrochemical properties are investigated with the BET, XRD, SEM and EDX, Mössbauer spectroscopy, cyclic voltammetry and charge-discharge measurements. Results are summarized follows.

(i) The meso-pore of the carbon structure was almost filled up by iron oxide nano-particles.

(ii) The composite electrode showed extremely high charge-discharge capacity with high current rate capability.

BET results of mesoporous carbons after electrolytic process indicated a decrease of specific surface area and also decrease in the pore diameter. The iron particles have a diameter of 2 – 3 nm with a length of 10 nm on the surface of carbon matrix, and the EDX measurement indicated a homogeneous distribution of iron on the surface. The binary composite should extremely high charge-discharge capacity of about 1200 mAh/g with a current density of 0.5 mA/cm^2, and the capacity vale is much higher capacity than those of γ-Fe_2O_3 nano-particles (230 mAh/g). Close

contact between the iron oxide and mesoporous carbon constructed by the electrolytic process provided the high performance.

In the present study, electrochemical properties of the ultra fine nanoparticles of iron oxide and a new binary system ‘iron oxide/mesoporous carbon’ were investigated, and possibilities for the cathode materials were indicated. The iron based materials are promising candidate for battery materials for its low cost and low environmental impacts, together its high electrochemical properties of large capacity and high current rate.

Acknowledgment

The author would like to express his application to Professor R. Kanno of Tokyo institute of technology for his continuous guidance and valuable discussion on this thesis, and wish to thank Associated Professor A. Yamada of Tokyo Institute of Technology for his encouragement. The author is greatly indebted Associated Professor N. Sonoyama of Nagoya Institute of Technology for his encouragement.

The author greatly wishes to thank Research Assistant M Yonemura of Ibaraki University for neutron diffraction, neutron total scattering measurement and for his encouragement at KENS and IPNS, and Professor K. Doumen foe SEM – EDX measurement.

The author especially wish to thank Dr. R. Kiyanagi and Dr. J. Fieramosca of IPNS for neutron powder diffraction measurement, and Research Assistant K. Ito of Kyoto University for neutron total scattering measurement and Associated Professor K. Kitamoto for Mossbauer measurement, Research Assistant T. Sanji and Dr. Inada for analysis by NMR and TG-MS measurement, and Y. Sumiya for TEM measurement, and Dr. Y. Kumashiro for FT-IR measurement, and T. Toya for ICP measurement and for M. Ishikawa for elemental analysis.

The author thanks all members of Kanno – Yamada Lab., especially T. Otani and Dr. C. Pitteloud.

Finally, the author would like to express his sincere gratitude to his parents Mr. Yasushi Kanzaki and Mrs. Natsuko Kanzaki, for their support, understanding, and encouragement.

December 2006

Sho Kanzaki